eman ta zabal zazu

Universidad del País Vasco
Euskal Herriko Unibertsitatea

Spin transport in magnetic insulator/heavy metal heterostructures

Juan Manuel Gómez Pérez

PhD thesis

Thesis Supervisors:

Prof. Fèlix Casanova and **Prof. Luis E. Hueso**

2020


CIC
nanoGUNE
nanoscience cooperative research center

Resumen

Los dispositivos electrónicos han invadido nuestra vida cotidiana hasta tal punto que determinadas acciones cotidianas sería imposible pensarlas sin la presencia de esta tecnología. Además, cuantos más dispostivos mayor es la necesidad de que sean más rápidos, más eficientes, es decir, con mayores capacidades. Todo esto ha sido posible gracias al increible desarollo de la electrónica en las últimas decadas, la cual explota la carga de los electrones para el transporte y el almacenamiento de información. La tendencia actual es miniaturizar los chips para intentar almacenar el máximo de información en el menor espacio posible, además de incrementar la densidad de transistores en el mismo espacio. Sin embargo, la miniaturización conlleva diversos problemas tecnológicos como caras técnicas de fabricación, o la aparición de efectos cuáticos y problemas de disipación de energía debido al diminuto tamaño de los transistores , que conlleva al mal funcionamiento o deterioro de los componentes electrónicos e incluso a la pérdida de información. Otro problema de la tecnología actual es el consumo de energía. En los útlimos años el consumo de energía se ha multiplicado y la tendencia es que siga aumentando. Por ejemplo, en la próxima decada se prevé que sólo el consumo de almacenamiento de información sea el 20% del consumo energético mundial.

Por tanto, surge la necesidad de una nueva *electrónica* de la que se espera que pueda proporcionar nuevas soluciones basadas en nuevos materiales, nuevas propiedades físicas y nuevas arquitecturas. Es en este punto dónde la *espintrónica* aparece como una solución alentadora a los problemas de la electrónica actual. Y todo ello a partir de aprovechar todos los grados de libertad del electrón: la electrónica convencional está basada basicamente en la carga del electrón, mientras que la espintrónica se basa tanto de la carga del electrón como otra propiedad intrínseca conocida como espín. El espín es el momento angular intrínseco asociado a los electrones que conlleva un momento magnético asociado.Es una propiedad cuántica, por lo que el momento angular puede tomar dos valores cuantizados: $\hbar/2$ y $-\hbar/2$, con $\hbar$ la contante de Planck reducida. Estos dos valores son más comunmente conocidos como espín arriba y espín abajo (del inglés *spin up* and *spin down*). Por tanto, la espintrónica busca aprovechar este grado de libertad para generar, transportar, manipular y detectar la información en forma

espín, con el objetivo de mejorar la electrónica de hoy en día.

El punto de partida de la espintrónica es 1989 cuando de manera simultánea e independiente el grupo de P. Grünberg y el grupo de A. Fert descubrieron el fenómeno físico conocido como magnetoresistancia gigante (GMR, por sus siglas en inglés *giant magnetoresistance*). Este descubrimiento supuso un gran impacto en el desarrollo de una nueva tecnología para la industria de las memorias magnéticas y, por ello, P. Grünberg y A. Fert fueron distinguidos con el premio Nobel de Física en 2007. La importancia de la GMR se demostró en su rápida incorporación al mercado de las memorias magnéticas tan sólo 9 años depués de su descubrimiento. Ésta se incorporó en las cabeza lectoras de los discos duros de la época ya que el efecto era sensible a campo magnéticos tan pequeños cómo los creados por los *bits* (unidad de medida de información) que definen todo el almacenamiento que conocemos actualmente. Por tanto, en los discos duros de la época los *bits* eran "grabados" con campos magnéticos y "leídos" eléctricamente por GMR. Su implantación en el mercado fue tan rápida debido a que permitió incrementar la densidad de grabación magnética en las memorias. A partir de este descubrimiento, buena parte de la comunidad científica se concentró en aprovechar el espín del electrón como catapulta para la siguiente generación tecnológica.

Más tarde, en 2004, las cabezas lectoras fueron sustituidas por las conocidas como magnetorresistencias de efecto tunel (TMR, por sus siglas en inglés), que permitian que cambios en la resistencia mucho mayores que la GMR. Y su mayor impacto fue que dió paso a las memorias magnéticas de acceso aleatorio (MRAMs por sus siglas en inglés, *magnetic random access memories*), las cuáles son memorias no volátiles. En las MRAMs, tanto la escritura como la lectura de los *bits* se podía realizar eléctricamente. A partir de aquí se ha seguido la tendencia de seguir miniaturizando las MRAMs, lo cual provoca que aparezcan problemas de estabilidad de la información debido a la increiblemente alta densidad de *bits*, ya que el campo magnético necesario para escribir un *bit* puede modificar la información del adyacente. Por tanto, se están investigando posibles técnicas alternativas para el proceso de escritura.

Como se puede ver, hay un gran esfuerzo por estudiar nuevos efectos y materiales para poder implementarlos en nuevos dispositivos tecnológicos para la creación, el transporte, el almacenamiento y detección de la información de espín de manera eficiente y sin las limitaciones del calentamiento por efecto Joule o de las longitudes de relajación de espín. Es en este punto donde aparece la espintrónica basada en aislantes eléctricos para el transporte y el almacenamiento de la información de espín. Y para ello es necesario crear y detectar la información de espín, para lo cual hay distintas técnicas, como por ejemplo la basada en el uso de materiales con acoplamiento espín-órbita grande en contacto con materiales magnéticos aislantes. En la intercara entre estos materiales ocurren

numerosos fenómenos físicos que necesitan ser estudiados. En concreto, en esta tesis nos vamos a centrar en dos de ellos: (i) el estudio de la evolución de la imanación de superficie de distintos materiales magnéticos aislantes usando una técnica conocida como magnetorresistencia Hall de espín (SMR por su siglas en inglés, *spin Hall magnetoresistance*); (ii) transporte de información de espín a través de aislantes magnéticos (MI, por sus siglas en inglés *magnetic insulator*), y esta información es transmitida por el material magnético gracias a la generación de ondas de espín que transportan la información de espín.

En la primera parte de la tesis estudiamos cuatro materiales magnéticos aislantes distintos: (i) ferrimagnético, (ii) antiferromagnético sintético, (iii) paramagnético y (iv) ferromagnético. Para ello, necesitamos depositar un metal no magnético (NM, por su siglas en inglés) con fuerte acomplamiento espín-órbita (SOC, *spin-orbit coupling*), como por ejemplo platino (Pt). Cuando se aplica corriente por los NM con fuerte SOC los espines con distinta orientación son deflectados en direcciones opuestas por el efecto Hall de espín. Si el Pt está en contacto con el material aislante, los espines con cierta orientación se acumulan en la intercara entre los materiales que interaccionan con los momentos magnéticos del aislante magnético. Dependiendo de la orientación relativa entre la imanación del aislante magnético y la polarización de espín de la acumulación, los espínes serán reflejados de nuevo al Pt o sean absorbidos por el material magnético. Por tanto, gracias a la SMR podemos estudiar la evolución de imanación de superficie del aislante magnético. Pero no sólo eso, la SMR también se puede definir la calidad de la intercara a través de otro parámetro importante, la conductancia de mezcla de espín (en inglés *spin-mixing conductance*), la cual gobierna el transporte de espín a través de la intercara NM/MI. La *spin-mixing conductance* $G_{\uparrow\downarrow=G_r+iG_i}$ tiene dos componentes distintas que definen el torque ejercido a la imanación al interactuar con los espines: (i) G_r corresponde al torque de antiamortiguamiento (*anti-damping-like torque*) que es torque que ejercen los espines a la imanación y controlan su direction. (ii) G_i corresponde al torque de campo (*field-like torque*) que transfiere un momento angular a la imanación igual a un campo efectivo paralelo a la acumulación de espines en la intercara. Además, otra conductancia juega un papel relevante en el transporte de espín en la intercara: *spin-sink conductance* (G_s), que es debida al *spin-flip scattering* y juega un papel muy importante en la excitación de ondas de espín o magnones. Para estudiar las conductancias en la intercara entre el NM/HM hacemos medidas de resistividad en función del campo magnético aplicado en los tres ejes principales (x,y,z), además de medidas con el ángulo. De estás medidas se pueden extraer las amplitudes de SMR conocidas como $\Delta\rho_1/\rho$ y $\Delta\rho_2/\rho$. Con las amplitudes de SMR y la teoría microscópica de SMR se puede estudiar las tres conductancias mencionadas en función de la temperatura y del campo magnético aplicado.

En el **Capítulo 3** investigamos un aislante ferrimagnético que es ampliamente usado debido a su baja campo coercitivo, baja constante de amortiguamiento y prácticamente nula anisotropía, este material es $Y_3Fe_5O_{12}$, conocido como YIG (del inglés, *yttrium iron garnet*). En los experimentos de SMR se suele utilizar el Pt como material con fuerte SOC, sin embargo, el Pt en contacto con un material magnético puede volverse magnético al menos las primeras capas, conocido como efecto de proximidad magnética. Es por ello que al principio hubo bastante controversias en la literatura sobre si era SMR o simplemente era efecto Hall anómalo (AHE, por las siglas en inglés de *anomalous Hall effect*) que aparece en metales magnéticos, dando lugar a un comportamiento no lineal en la resistividad transversal cuando el campo está aplicado perpendicular a la muestra. Sin embargo, la teoría de SMR también predice esté término que, para el caso de SMR, varía con el cuadrado del ángulo Hall de espín (θ_{SH}) en vez de ser lineal como en el caso de AHE. En este capítulo, para diferenciar entre SMR y AHE, realizamos primero el experimento en Pt/YIG y posteriormente reemplazamos el Pt por oro (Au) que también es un material con SOC, pero sin la posibilidad de que se vuelva magnético en contacto con el YIG. En ambos casos fuimos capaces de detectar el término no lineal en la resistividad transversal. Por tanto, la física detrás de ambos experimentos es la misma y puede ser completamente entendida por SMR, a través de la presencia del torque de campo (*field-like torque*), sin necesidad de la presencia del efecto de proximidad magnética.

El **Capítulo 4** presenta una bi-capa ultrafina (13 nm en total) de dos aislantes magnéticos que están acoplados antiferromagnéticamente. La bi-capa está formada por YIG en la capa superior, mientras que la inferior es $Gd_3Fe_5O_{12}$, (GdIG, por su siglas en inglés *gadolinium iron garnet*) el cuál también es un aislante ferrimagnético. Cuando se aplican campo magnéticos pequeños, la imanación del YIG es opuesta al campo aplicado y ésta rota a medida que el campo aumenta intentando alinearse finalmente con el campo externo. Somos capaces de ver la evolución del imanación de la bi-capa a través de medidas de SMR, que sólo es sensible a la imanación de superficie. Confirmamos este comportamiento con medidas de dicroismo circular magnético de rayos X en sincrotrón. Demostramos que la bi-capa se comporta como un antiferromagnético sintético basado en materiales aislantes magnéticos. Finalmente, también observamos un efecto de memoria en la dirección perpendicular al plano, el cual puede ser leido por medidas longitudinales de SMR en el Pt.

En el **Capítulo 5**, el siguiente paso fue estudiar un aislante magnético distinto que no presentara imanación espontánea en ausencia de campo magnético aplicado. Por ello, elegimos $Gd_3Ga_5O_{12}$ (GGG, por su siglas en inglés gadolinium gallium garnet) que es un material paramagnético puro con una temperatura de Curie-Weiss de -2 K. En principio, las medidas de SMR sólo se pueden hacer

cuando la imanación está saturada y en un material paramagnético es necesario campos magnéticos excesivamente grandes. Sin embargo, en nuestro caso, a baja temperatura (2 K) y altos campos magnéticos ($>$ 3.5 T) podemos saturar el GGG, observando claras señales de SMR debido a la inducción de imanación en el GGG. También observamos el término no lineal en la resistividad transversal que predice la teoría de SMR cuando el campo magnético es aplicado fuera del plano de la muestra. Por otra parte, aplicamos un módelo microscópico para SMR (desarrollada por nuestro colaboradores X.-P. Zhang, Dr. Vitaly N. Golovach y Prof. Dr. F. Sebastian Bergeret), que incluye el acoplamiento de canje entre los espínes de conducción del Pt y los espínes localizados del GGG. Gracias a esta teoría podemos estudiar la evolución de los distintos términos de la *spin-mixing conductance* con el campo magnético aplicado, dónde encontramos que G_i es igual de importante que G_r en la intercara entre el Pt y el GGG.

En los experimentos de SMR realizados que podemos encontrar en la literatura, la gran mayoría son en YIG o otros aislantes ferrimagnéticos, pero nunca un aislante realmente ferromagnético. Y esto se debe a que los aislantes ferromagnéticos son escasos y con una temperatura de Curie bastante baja, por lo general por debajo de los 100 K. En el **Capítulo 6**, presentamos medidas de SMR en Pt/EuS, dónde el EuS es un aislante ferromagnético por debajo de 25 K. Realizamos medidas de SMR longitudinal donde observamos claramente señal de SMR en la intercara entre el Pt y el EuS por debajo de $\sim$25 K, desapareciendo la señal de SMR por encima de dicha temperatura. También podemos observar el término no lineal de la resistividad transversal al aplicar el campo magnético fuera del plano, y en este caso particular, la amplitud de la señal es mayor que la medida de resistividad longitudinal, en contraposición con otros aislantes magnéticos. Es por ello que las contribuciones de los distintos términos de la *spin-mixing conductance* podrían ser distintos. Para ello empleamos de nuevo la teoría microscópica de SMR para estudiar la dependencia con la temperatura de los distintos términos. De estos resultados encontramos que, por primera vez, en la intercara entre un NM/MI la contribución de torque de campo (G_i) es mayor la contribución tipo amortiguamiento (G_r), hasta 4 veces más grande a la temperatura más baja estudiada.

Por último, en los dos último capítulos de la tesis vamos un poco más allá y nos centramos en el transporte de la información a través de los MI. Para ello utilizamos una geometría no local, utilizando como generador y detector de los magnones un NM. Hay distintas técnicas para la generación de magnones en un MI, pero aquí sólo nos centramos en la generación eléctrica y térmica. La primera, de manera parecida a la medidas de SMR, se aplica un corriente a través del NM generando una acumulación de espines en la interacara NM/MI. Cuando los espines son paralelos (antiparalelos) a la imanación del MI se aniquilan (generan)

magnones debido a la interacción de canje entre los espines en NM y los momentos magnéticos del MI. Esto crea un desequilibrio de la población de magnones en la intercara dando lugar a una difusión de los magnones siendo detectados hasta varias micras de distancia en el segundo NM por el proceso recíproco a la excitación. Sin embargo, los magnones también pueden ser inducidos térmicamente. Cuando en un MI se aplica un gradiente térmico, se excitan magnones debido al efecto Seebeck de espín. Estos magnones también pueden difundir a través del MI siendo detectados en el segundo NM. El transporte de magnones a través de MI está supeditada a la longitud de difusión de magnónica (λ_m). Sin embargo, algunos de los primeros resultados de la literatura son aún contradictorios. En particular, para YIG, los valores de λ_m tienen una amplia dispersión de unos grupos de investigación a otros (entre 1 y 50 μm, pero el origen de esta diferencia todavía no se ha conseguido identificar. En el **Capítulo 7** estudiamos λ_m en un YIG de 2 μm de espesor en función de la temperatura y de la intensidad del campo magnético aplicado. Encontramos que hay una diferencia clara tanto con la temperatura como con el campo magnético dependiendo de si los magnones son excitados eléctrica o térmicamente.

Finalmente, en el **Capítulo 8** investigamos el transporte de espín a través de un material sin orden magnético de largo alcance dónde se había reportado que la información de espín podía ser transportada a distancias mucho más largas que, por ejemplo, en YIG. Para este estudio, utilizamos YIG amorfo (a-YIG) que es un material paramagnético. En nuestros resultados no detectamos ninguna señal de espín y la única señal que somo capaces de detectar aparece a temperaturas altas cuando la resitividad del a-YIG decae fuertemente con la temperatura. Por tanto, nuestros resultados sólo pueden ser atribuidos a una corriente de fuga entre el inyector y el detector debido a que a-YIG a alta temperatura comienza a conducir la corriente eléctrica.

Abstract

Everyday devices used in our lives such smartphones or computers have been possible thanks to the developing of a technology based on the electrical charge. Electronics exploits the charge degree of freedom of the electron for transporting and storing information. There is a trend for the last 50 years to make all the gadgets smaller and smaller by increasing the density of the transistors in the same area (known as Moore's law). This leads to several technological problems, such as expensive fabrication techniques but, more importantly, the current transistor size is absolutely tiny, rising problems that appear at very small dimensions, such as quantum effects and energy dissipation. Therefore, there is a necessity of new technology to replace current CMOS technology with new physics, unconventional materials and structures to overcome such problems. At this point, spintronics emerges as a promising field to exploit not only the charge but also the other degree of freedom of electron, the spin. This new research field aims at exploiting the generation, manipulation and detection of spin information, in order to improve the current technology by taking the advantage of the spins.

In 1989, two different groups observed simultaneously, but independently, a new and revolutionary effect: the Giant Magnetoresistance (GMR) effect. The first observation of the GMR was in a stack of ferromagnetic layers with non-magnetic metallic interlayers in between where the resistance experimented a *giant* change when an external magnetic field was applied. GMR was rapidly transferred into the magnetic hard drives market, which encouraged the scientific community to focus on exploiting the spin as the launch pad for the next technology generation. Nowadays, there is a great effort for studying new effects and materials to be implemented in the devices; for the creation, transport, storage and detection of spin information in an efficient way without the limitations of spin relaxation and Joule heating. It is at this point where the insulator-based spintronics appears. Insulator-based spintronics uses electrical insulators for transport and storing the spin information. The important issue is how to create and detect this spin information. There are different ways to do so. The one used in the thesis is by using heavy metals (HM) in contact with a magnetic insulator (MI), which leads to many different phenomena at the interface and need to be studied and under-

stood. In this thesis, we introduce different spin-dependent phenomena in MI/HM interfaces and how they affect to the creation and transport of the spin information. The thesis is divided in two different parts: (i) spin Hall magnetoresistance (SMR) in magnetic insulators, (ii) Magnon spin transport in magnetic insulators. In the first part (**Chapters 3**, **4**, **5** and **6**), we mainly focus on the interface between the heavy metal and the magnetic insulator, studying the evolution of the surface magnetization by SMR. As well as that, we can study by SMR the quality of the interface given by the *spin-mixing* conductance. Spin-dependent scattering of conducting electrons at heavy metal (HM)/magnetic insulator (MI) interface can be described in terms of three parameter: the so called spin-sink conductance G_S and the real and imaginary part of the spin-mixing conductance, $G_{\uparrow\downarrow} = G_r + iG_i$. Each parameter is relevant of different experimental situation. For example, G_s originates from spin-flip processes and therefore is a vital parameter in magnonic application, whereas G_r is a spin transfer torque to the magnetization of the MI, and, plays a fundamental role in spin-pumping experiments. On the other hand, G_i is a measured of the interfacial exchange field which induces a field-like torque in the conduction electrons of the HM. In the second part of the thesis (**Chapters 7** and **8**), we focus on the transport of the spin information along the magnetic insulator by spin waves or magnons. We are able to excite, transport and detect the spin information non-locally, quantifying the transport properties.

Part I. *Spin Hall magnetoresitance in magnetic insulators*

- **Chapter 3**. Magnetoresistance signals in platinum in contact with magnetic insulators are common observations that could be explained by either magnetic proximity effect or SMR. In this chapter, longitudinal and transverse magnetoresistances are measured in a pure gold thin film on the ferrimagnetic insulator *yttrium iron garnet* (YIG). We show that both the longitudinal and transverse magnetoresistances have quantitatively consistent scaling in YIG/Au and in a YIG/Pt reference system when applying the SMR framework.

- **Chapter 4**. We investigate a ultra-thin YIG / gadolinium iron garnet (GdIG) insulating bilayer on gadolinium gallium garnet (GGG). From SMR and X-ray magnetic circular dichroism measurements, we show that the YIG and the GdIG layers magnetically couple antiparallel even in moderate in-plane magnetic fields. The results demonstrate an all-insulating equivalent of a synthetic antiferromagnet in a garnet-based thin film heterostructure and could open new venues for insulators in magnetic devices.

- **Chapter 5**. We study the SMR of Pt thin film on top GGG, which is a textbook paramagnetic insulator. The observed magnetoresistance is well

explained by microscopic theory of SMR that takes into account the paramagnetic behavior of the localized spins in GGG and includes the exchange coupling between the conduction electron-spins in Pt and the localized spins in GGG. Our result establishes the spin transport based on the spin-mixing conductance at metal/paramagnetic insulator interfaces. From the analysis of the spin conductances we found that G_i contribution is as important as the G_r contribution.

- **Chapter 6**. The spin conductance terms are broadly studied in ferrimagnetic insulators, where usually the contribution of the G_r is much larger than that of G_i, which leads to only few reports about the field-like torque at HM/MI interface. In this chapter, we investigated for the first time the interface between a HM and ferromagnetic insulator (FMI). The FMI is EuS showing a ferromagnetic behavior below 30 K. We have demonstrated that in a HM/FMI the contribution of field-like torque is up to four times larger than the one of G_r at low temperatures in Pt/EuS.

Part II. *Magnon spin transport in magnetic insulators*

- **Chapter 7**. Magnon currents can be excited both electrically and thermally, even in MIs, by applying charge currents in an adjacent metal layer. Earlier reports in thin YIG films suggested that the diffusion length of magnons is independent on the excitation method, but different values were obtained in thicker films. In this chapter, we study the magnon diffusion length for electrically and thermally excited magnons in a 2-μm-thick YIG film as a function of temperature and magnetic field. Our results evidence that the diffusion length depends on the generation mechanism. Moreover, we show that the damping of the thermally driven magnons with magnetic field is weaker than for those excited electrically. Finally, we demonstrate that the magnon diffusion length for thermally excited magnons is independent of the YIG thickness and material growth conditions, confirming that this quantity is an intrinsic parameter of YIG.

- **Chapter 8**. Long-distance transport of spin information in insulators without magnetic long-range-order has been recently reported. In this chapter, we perform a complete characterization of amorphous YIG (a-YIG) films grown on top of SiO_2. In this chapter, we confirm a clear amorphous structure and paramagnetic behavior of our a-YIG films, with semiconducting behavior resistivity that strongly decays with increasing temperature. The non-local transport measurements show a signal which is not compatible with spin transport and can be attributed to the drop of the a-YIG resistivity caused by Joule heating. Our results emphasize that exploring spin

transport in amorphous materials requires careful procedures in order to exclude the charge contribution from the spin transport signals.

Contents

Chapter 1

Introduction

1.1 Introduction to spintronics

In the last decades, everyday devices used in our lives, such smartphones or computers, have been possible thanks to the development of a technology based on the electrical charge: electronics. Electronics exploits the charge degree of freedom for transporting and storing information. In this technology, there is a main actor, silicon (Si). Si is a material with well-established manufacturing and proper properties that make it very convenient for semiconductor-based electronics, with the Complementary Metal-Oxide-Semiconductor (CMOS) technology as the best example [1], where Si is used as the main material for the transistors. A transistor is an electronic component used to amplify or switch electronic signals, being the basic element in conventional electronics.

Due to market's demands, there is a trend to make electronic the gadgets smaller and smaller, increasing the density of the transistors in the same area. This leads to several technological problems, such as expensive fabrication techniques, and ti fundamental problems that appear at very small dimensions (the current transistor size is at $\sim 5-10$ nm), such as quantum effects and energy dissipation, hindering the trend of Moore's law [2] as was predicted [3]. There is thus the necessity of a post-CMOS technology with new Physics, unconventional materials and structures to overcome such problems. At this point, spintronics emerges as a promising field to exploit not only the charge but also the other degree of freedom of electron, the spin.

The spin is the intrinsic angular momentum associated to the electron. It is a quantum property and has an associated magnetic moment. In particular, the magnetic moment of an electron can take two values: $\hbar/2$ and $-\hbar/2$, also known as *spin up* and *spin down*, respectively, where $\hbar$ is the reduced Planck constant. This

new research field aims at exploiting the control of the spin degree of freedom in electronic currents to transmit and manipulate information, which could be used to improve the current technology by taking the advantage of the spins. The birth year of spintronics is 1989, where two different groups observed simultaneously, but independently, a new and revolutionary effect: the giant magnetoresistance (GMR) effect, discovered by the groups of P. Grünberg [4] and A. Fert [5]. Both were distinguished with the Nobel prize in Physics in 2007 because of the importance and the impact of such a discovery for developing a new technology [6]. The first observation of the GMR was in a stack of ferromagnetic (FM) metallic layers with non-magnetic metallic (NM) interlayers in between where the resistance experimented a *giant* change when an external magnetic field was applied, see Fig. 1.1.

The working principle of the GMR is that, when a charge current is applied into a FM, this current will be spin-polarized because of the magnetic moments in the FM. Therefore, the spin-polarized current will carry more spin up than down, or vice versa. When the magnetic field is applied, the relative magnetization of the FMs changed from parallel to antiparallel configuration, which leads to a different resistance depending on the configuration. When the current is applied through the stack, the spins up and down will scatter differently depending on the relative magnetization configuration of the FM. This means that for the antiparallel configuration both spins suffer scattering having a high resistance state [top Fig. 1.1(a)], whereas for the parallel configuration only the minority spins are scattered which gives a low resistance state [bottom Fig. 1.1(a)]. This discovery became a huge advancement in the magnetic memory industry, because GMR was sensitive enough to detect magnetic fields as small as the ones created by the magnetic bits in hard drives. GMR was one of the discoveries that was transferred incredibly fast into the market through the hard-drive read heads, because it allowed to increase the density of magnetic recording.

The GMR discovery encouraged the scientific community to focus on exploiting the spin as the launch pad for the next technology generation. Another relevant spin-based effect was discovered before the GMR, but it took some time to take off due to reproducibility problems in the fabrication method: the tunneling magnetoresistance (TMR) [7]. The configuration of this effect is the same used for GMR, but with a thin electrical insulator as an interlayer between the FMs instead of a NM metal. This stack is usually known as a magnetic tunnel junction (MTJ) [8, 9]. The insulating layer is so thin (typically around 1 nm) that the conduction electrons can tunnel through the barrier, and the tunneling current depends on the relative orientation of the magnetization of the two FM layers, which can be tuned with an applied magnetic field. From an applied point of view, the TMR had a huge impact, since it is the building block of the

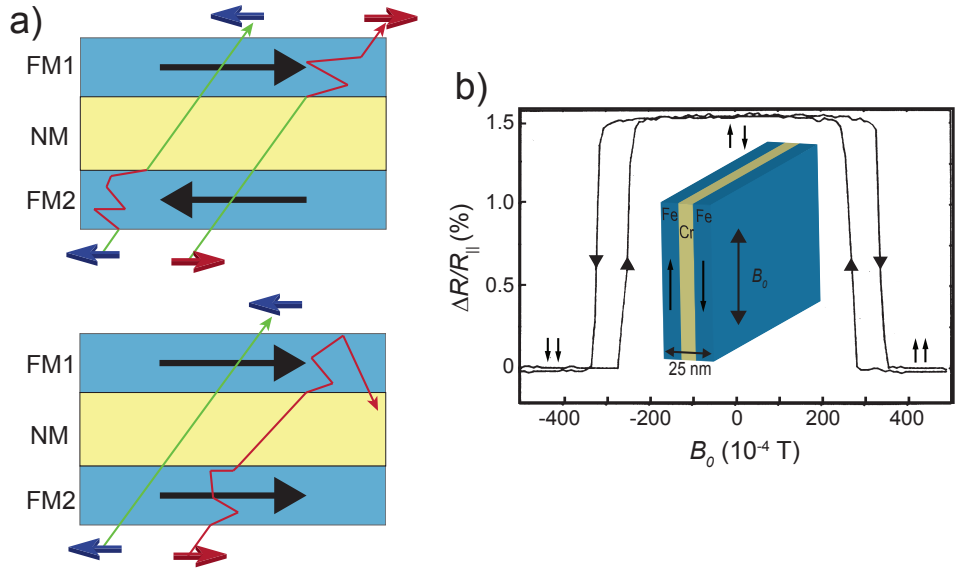

Figure 1.1: **Giant magnetoresistance.** (a) Working principle of GMR reported by P. Grüngberg [4] and A. Fert [5] at the same time in 1989. Top sketch shows how both spin types suffer scattering in one of the two ferromagnetic layers (F1 top, F2 bottom), leading to a high resistance state. However, bottom sketch shows how only one of the spin types suffers scattering in both ferromagnetic layers, leading to a low resistance state. (b) Magnetoresistance *vs.* magnetic field applied in plane, along the easy axis. Inset: Sketch of the 25-nm-thick Fe/Cr/Fe stack and orientation of the magnetic field. At $B_0 = 0$ T, the exchange coupling of the Fe layers across the Cr is antiferromagnetic. Figure adapted from Ref. [4].

non-volatile magnetic random access memories (MRAM). In this type of memory, the relative orientation between the two FM (parallel or antiparallel) defines the magnetic state, know as digital bits (bit "0" for parallel configuration which is a low resistance state, and bit "1" for antiparallel configuration, which is a high resistance state), and it can be read electrically with the TMR effect.

In MRAMs, besides reading the magnetic state, we also must be capable to write it. There are different ways for this. First of all, the building block is based on MTJ: one of the FM is a "fixed" layer where the magnetization is pinned and the polarization cannot be changed unless a huge magnetic field is applied. The other FM is the so-called "free" layer and can be switched by different methods. In the first generation of MRAMs, the bits were written by a field-driven technique. The writing process was generated by applying a charge current to a metal in contact to the "free" layer of the MTJ, creating an Oersted field large enough to switch the magnetization of the FM. However, downscaling the memory devices brings problems of storage stability with the increase of the bit density, since the magnetic field can modify more than one bit the magnetic fields are not localized enough. Fundamental advances in spintronics related to the optimization of TMR and the spin-transfer torque (STT) have been used to

improve the writing process in a more efficient way [10, 11]. STT was the second breakthrough in spintronics. In STT, the spins transfer an angular momentum to the magnetization of a FM, exerting a torque to the magnetization modifying the magnetic state. The second generation of MRAMs uses STT for the writing process. In this technique, the spin-polarized current is the one switching the magnetization of the free layer by exerting a torque, presenting the localization missing in the field-driven MRAM and, thus, more favorable miniaturization. STT-MRAMs offer long retention times and large read-out signals, and are already being commercialized by several companies, including tech giants (Samsumg, Intel, Qualcomm) as well as tool makers (Advanced Materials, Singulus), being able to develop STT-technologies beyond the 28 nm node with chip capacities larger than 1 Gb. However, the STT-MRAMs present some limitations in terms of the relatively large switching latency of STT and the high currents needed to reach sub-ns switching times, that can be harmful for the MTJs. The third generation of MRAMs are based on spin-orbit torque (SOT), which offers unmatched switching speed and endurance compared to STT-MRAM. SOT is based on the charge-spin interconversion provided by the spin-orbit coupling in some materials (see section 1.3) and allows for switching the free layer without passing a current through the tunnel barrier, minimizing the risk of breaking it. As well as that, the separation of write and read paths avoids write errors during read out and allows for setting the direction of the torques independently of the magnetization stack.

1.1.1 Pure spin currents

The first generation of spintronic devices we have presented, exploited the spin-polarized charge current. However, a new generation of spintronic devices is now envisioned, based only in pure spin currents. Pure spin currents are a diffusive flow of spins without a net charge flow, avoiding the heating related to the charge flow [12]. In electric conductors the charge current carries spin-up and spin-down electrons, then, the conduction in the metal can be interpreted as two independent and parallel channels, one for spins-up and other one for spins-down. In 1930, Mott proposed this *two-current model* [13], which was later applied by Fert and Campbell to describe conductivity behavior in FM metals [14, 15]. In the model, each channel has its own current density ($\boldsymbol{j}_{\uparrow(\downarrow)}$) that depends on the gradient of its own quasi-electrochemical potential ($\boldsymbol{\mu}_{\uparrow\ (\downarrow)}$):

$$\boldsymbol{j}_{\uparrow(\downarrow)} = -\frac{\sigma_{\uparrow(\downarrow)}}{e}\nabla\boldsymbol{\mu}_{\uparrow(\downarrow)} \tag{1.1}$$

where $\sigma_{\uparrow(\downarrow)}$ is the spins up (down) conductivity. The total charge current density

is $\boldsymbol{j}_c = \boldsymbol{j}_\uparrow + \boldsymbol{j}_\downarrow$, while the spin current density is defined as $\boldsymbol{j}_s = \boldsymbol{j}_\uparrow - \boldsymbol{j}_\downarrow$. In equilibrium, the relation $\mu = \mu_\uparrow = \mu_\downarrow$ holds for both FM and NM, thus $\boldsymbol{j}_s = 0$ in NM, which means that the charge current is equally distributed between spin-up and spin-down channels.

This applies for equilibrium states, however, the spin transport phenomena occurs during non-equilibrium situations when the system relaxes to an equilibrium state. The non-equlibrium state is defined by a *spin accumulation* $\boldsymbol{\mu_S} = \boldsymbol{\mu_\uparrow} - \boldsymbol{\mu_\downarrow}$, which means that

- for FM, where $\sigma_\uparrow \neq \sigma_\downarrow$:

$$\boldsymbol{j}_s = -\frac{1}{e}(\sigma_\uparrow \mu_\uparrow - \sigma_\downarrow \mu_\downarrow) \tag{1.2}$$

- for NM, where $\sigma_\uparrow = \sigma_\downarrow$:

$$\boldsymbol{j}_s = -\frac{\sigma_e}{e}\nabla \boldsymbol{\mu_s} \tag{1.3}$$

with $\sigma_e = \dfrac{\sigma_\uparrow + \sigma_\downarrow}{2}$, and in both cases the spin accumulation will follow a spin relaxation described by the spin diffusion equation:

$$\nabla^2 \boldsymbol{\mu_s} = \frac{\boldsymbol{\mu_s}}{\lambda_s^2} \tag{1.4}$$

with λ_s being the spin diffusion length, which describes the length scale over which an imbalance relaxes to equilibrium. There are different ways to generate a spin accumulation or spin imbalance. Figures 1.2(a)-(c) show different spin injection techniques by using ferromagnetic materials as the spin source, whereas in Fig. 1.2(d) the spin Hall effect present in the heavy metals is sketched [16, 17]. The pure spin currents can be detected by the reciprocal effects of the injection ones, see Figs. 1.2(e)-(h). In the case of the injection techniques by using FMs, once the pure spin current is generated, it is injected to a NM to be transported for long distances, which will depend on λ_s of the material. For example, it is necessary the use of light metals which have long λ_s, such a copper (Cu) with $\lambda_s \sim 0.3$ μm at room temperature (up to 1.0 μm at 4 K) [18]. In other cases, it is injected to a heavy metal (HM), being detected by inverse spin Hall effect, as we will explain later in Section 1.3. In HMs, λ_s is usually very short (1−10 nm) and, thus, the transport of the spin information can be an issue.

As can be seen, there is a great effort by the scientific community to study new effects and materials to be implemented in the devices for a new technological revolution. In the case of spintronics;this effort is focus on the creation, transport, storage and detection of spin information in an efficient way without the limitations of spin relaxation and Joule heating. It is at this point where the insulator-based spintronics appears to avoid the energy dissipation due to the carriers movement. Insulator-based spintronics uses electrical insulators to transport and storage the spin information. The spin information can be transported not only by conduction-electron spin currents, as we have seen previously, but it can also be transport by spin-wave spin current. In magnetic insulators (MI), the spin information can be transported by the spin angular momentum carried by collective magnetic-moment precession, know as spin waves or magnons, being transported for longer distances than light metals [19, 20] (Section 1.5.6). They key point is how to create and detect this spin information. There are different ways to do so, for instance, by using HM in contact with a MI, which leads to a plethora of different phenomena at the interface and need to be studied and understood.

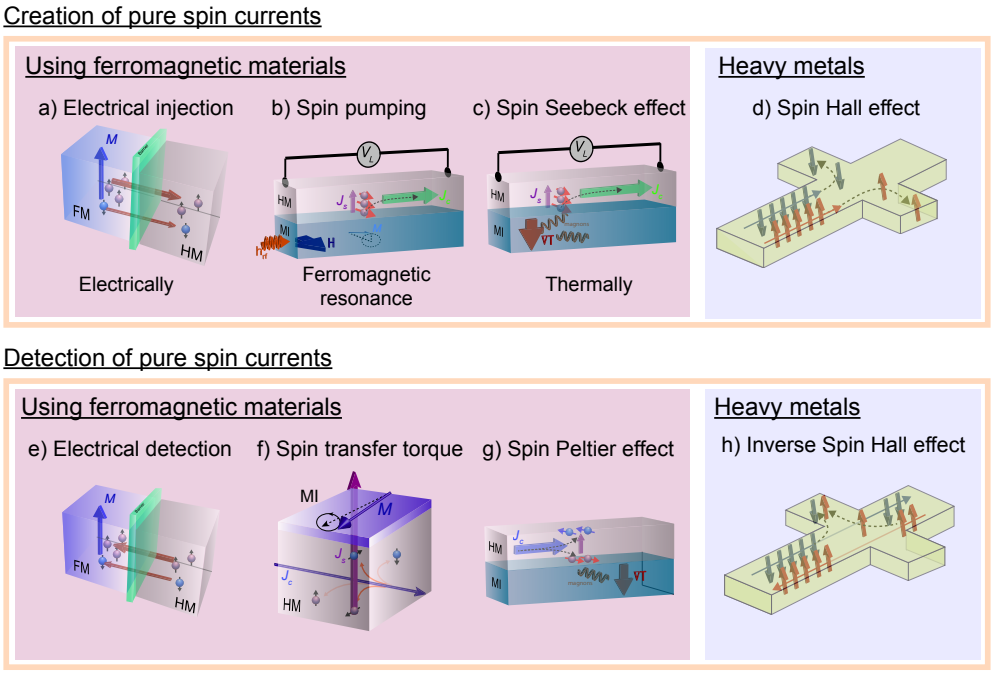

Figure 1.2: **Spin injection and detection techniques.** The top images show the spin injection techniques by using ferromagnets (a-c) or heavy metals (d). With ferromagnetic materials: (a) electrical injection, (b) spin pumping, and (c) spin Seebeck effect. By using heavy metals: (d) spin Hall effect. The bottom images show the spin detection techniques by the reciprocal effect of the spin injection techniques. Figures adapted from Refs. [21–26].

In this thesis, we will study some of these spin-dependent phenomena at HM/MI interfaces and how they relate to the creation and transport of spin information. In the following section, we will introduce all the ingredients necessary for the generation, transport and detection of spin information at HM/MI interfaces.

1.2 Spin-orbit coupling and spin orbitronics

The possibility of generating and detecting pure spin currents by using metals with strong spin-orbit coupling (SOC), without the necessity of any FM metal, opened a venue to exploit this approach in spintronics devices. All transport phenomena related to SOC is included in the new field of spin orbitronics [27,28]. In Quantum Physics, the SOC is the interaction between the spin ($\boldsymbol{S}$) and the orbital ($\boldsymbol{L}$) angular momentum of the electron around the nucleus, which is a key interaction in Condensed Matter Physics, and dominates many effects in magnetism and spintronics [29].

To understand the basis of SOC, we first need to introduce some physical concepts. First of all, when a charged particle rotates around an axis, it has an associated orbital angular momentum $\boldsymbol{L}$, which creates a magnetic moment $\boldsymbol{\mu_0}$. For the particular case of an electron, it is defined as:

$$\boldsymbol{\mu_0} = -\frac{e}{2m_e}\boldsymbol{L} \tag{1.5}$$

where e is the electron charge and m_e is electron mass. This is described by classical Physics. However, the electron has a quantum spin angular momentum $\boldsymbol{S}$, which does not have a classical equivalent, but can be naively seen as a rotation around its own axis. This means means that $\boldsymbol{S}$ points opposite for spins up and for spins down. Moreover, $\boldsymbol{S}$ has an associated magnetic moment $\boldsymbol{\mu_s}$ given by:

$$\boldsymbol{\mu_s} = -g\frac{e}{2m_e}\boldsymbol{S} = -\gamma\boldsymbol{S} \tag{1.6}$$

where γ is the gyromagnetic ratio and g is the $g-$factor that for an electron takes a value of approximately 2.

Now, we can define the SOC as a relativistic interaction of the electron into the electrical potential created by the positive charge of the nucleus. This relativistic interaction adds a correction term to the hydrogen-atom Hamiltonian that results

in a split of the energy. To understand this better, let us see from the point of view of the electron. The positive charge nucleus would orbit around the electron generating a magnetic field that interacts with the spin magnetic moment of the electron $\boldsymbol{\mu_S}$, see Fig. 1.3(a). Therefore, the Hamiltonian of the system would be:

$$\mathcal{H} = \boldsymbol{\mu_S} \cdot \boldsymbol{B} \tag{1.7}$$

where $\boldsymbol{\mu_S}$ is defined in Eq. 1.6 and depends on $\boldsymbol{S}$, and the effective magnetic field $\boldsymbol{B}$ seen by the electron depends on the orbital magnetic moment $\boldsymbol{L}$ as follows:

$$\boldsymbol{B} = \frac{1}{4\pi\varepsilon_0}\frac{Ze^2}{m^2c^2r^3}\boldsymbol{L} \tag{1.8}$$

where ε_0 is the electric constant, Z is the atomic number, c is the speed of the light and r is the distance measured from the nucleus. Therefore, if we rewrite the Hamiltonian in Eq. 1.7 as a function of $\boldsymbol{L}$ and $\boldsymbol{S}$ we obtain the spin-orbit coupling Hamiltonian:

$$\mathcal{H}_{SOC} = \frac{Ze^2}{4\pi\varepsilon_0}\frac{1}{m^2c^2r^3}\boldsymbol{L}\cdot\boldsymbol{S} = \xi\boldsymbol{L}\cdot\boldsymbol{S} \tag{1.9}$$

where this Hamiltonian can change the sign taking into account the relative orientation of $\boldsymbol{L}$ and $\boldsymbol{S}$, depending on whether the electron has spin up or down, see Fig. 1.3(b) and 1.3(c). Thus, SOC splits degenerate spin sub-bands, modifying the electronic band structure of the materials, which leads to a plethora of effects where the SOC plays an important role. For instance, it is crucial for the magneto-crystalline anisotropy, magnetic hardness or domain wall structure in magnetic materials. It also influences the transport properties in spintronics where, due to the spin-orbit coupling, the scattering events might become spin-dependent, as we show in the following sections.

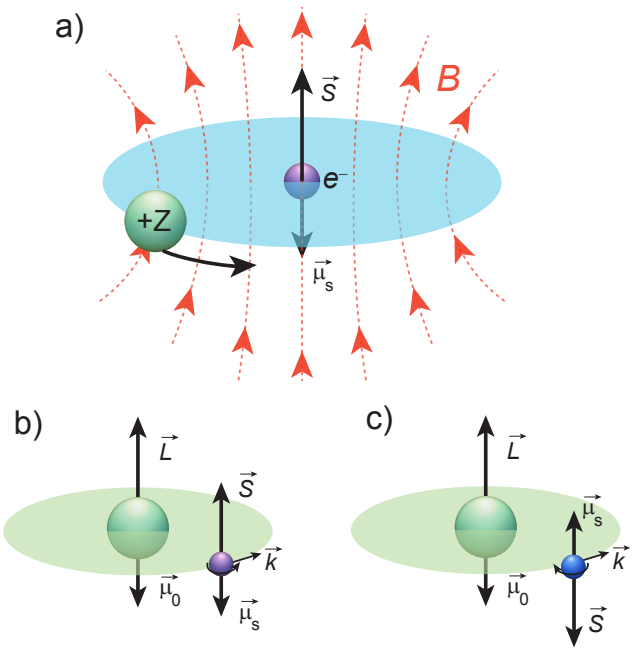

Figure 1.3: **Spin-orbit coupling.** (a) Sketch of an electron moving into the potential created by the positive charge nucleus, seen from the electron point of view. $\boldsymbol{S}$ is the spin angular momentum which generates a small magnetic moment for the electron $\boldsymbol{\mu_S}$, $\boldsymbol{L}$ is the orbital angular momentum that also generates a tiny magnetic field $\boldsymbol{\mu_0}$, $\boldsymbol{B}$ is the magnetic field induced by the electrical field because of the electron movement. (b) and (c) show the energy-split in two different energy levels depending on the relative coupling between $\boldsymbol{S}$ and $\boldsymbol{L}$, (b) parallel or (c) antiparallel. This figure is adapted from Ref. [30].

1.3 Spin Hall effect and inverse spin Hall effect

Spin Hall effect is directly related to SOC and, nowadays, is broadly used in spintronic applications for the generation of pure spin currents [31, 32]. Nonetheless, let us start from the birth date of the Hall effects. In 1879, Edwin H. Hall observed that, when a charge current $\boldsymbol{j}_c$ flows into a conductor material in presence of an out-of-plane magnetic field H, a transverse voltage to $\boldsymbol{j}_c$ and H is measured. The effect was caused by a deflection of the charge carriers as a result of the (then already known) Lorentz force. This effect is nowadays known as the ordinary Hall effect (OHE) [33], Fig. 1.4(a). The associated transverse resistivity ρ_{xy} is proportional to H,

$$\rho_{xy} = R_{OHE} \cdot H_z \tag{1.10}$$

where R_{OHE} is the Hall coefficient that is intrinsic of each material and the sign of the coefficient depends on the type of carriers (electrons or holes) of the

conductor material. Beyond the OHE in conductors, E. H. Hall performed the same experiment in magnetic conductors and observed that, apart from the OHE contribution with H, an extra contribution to the Hall resistivity was present at $H = 0$, so-called anomalous Hall effect [34]. E. H. Hall realized that this extra effect that is present at $H = 0$ in ferromagnets related to the magnetization M of the ferromagnet, see Fig. 1.4(b). AHE was experimentally discovered in 1881, but there was no phenomenological equation until 1929 by Smith and Sears [35] that included both OHE and AHE

$$\rho_{xy} = \rho_{OHE} + \rho_{AHE} = R_{OHE} H_z + R_1 M \tag{1.11}$$

where R_1 is the anomalous Hall coefficient and M the out-of-plane magnetization of the FM conductor. However, even if the equation could describe the AHE behavior in ferromagnets, the origin of the AHE was unclear for several decades until Karplus and Luttinger revealed its relation with the SOC [36]. They proposed that, when the electrons are moving into a conductor, due to the scattering events, electrons acquire a transverse 'anomalous' velocity in which the direction depends on the relative orientation of the spin, having opposite direction for spin up and down, as it is sketched in Fig. 1.4(b). Therefore, in a FM, where the conductivity of spins up and down is different, i.e., the current is spin-polarized (see section 1.1.1), not only a spin accumulation but also a charge accumulation appears at the edges, which gives rise to the 'nomalous' transverse voltage measured.

After the AHE discovery, it was not until 1971 when D'yakonov and Perel suggested that the very same mechanism of AHE should be present in NM metals [16]. In a NM, the amount of electrons with spin up is exactly the same than electrons with spin down, which means there is no charge accumulation at the edges, but only spin accumulation [Fig. 1.4(c)] which would induce a transverse pure spin current. The absence of charge accumulation was an issue to measure such effect, and it remained just as a theoretical prediction for a long time. Finally, in 1999, the effect was rediscovered by Hirsch, who named it for the first time *spin Hall effect* [17]. In this work, Hirsch proposed an experiment to measure the pure spin current in NM, pushing the experimentalists to detect it. The first challenge was the lack of direct electrical signal, that is why the first evidences of the spin accumulation in a semiconductor were detected optically [37, 38], and one year later detected electrically by the reciprocal effect of the SHE, known as inverse SHE (ISHE) [39, 40]. ISHE is a crucial effect in this thesis for the detection of the pure spin current, because whenever there is a pure spin current in a NM with SHE, a transverse charge current is induced by ISHE, see Fig. 1.4(d). It is commonly accepted that SHE and AHE show the same mechanisms [32], thus,

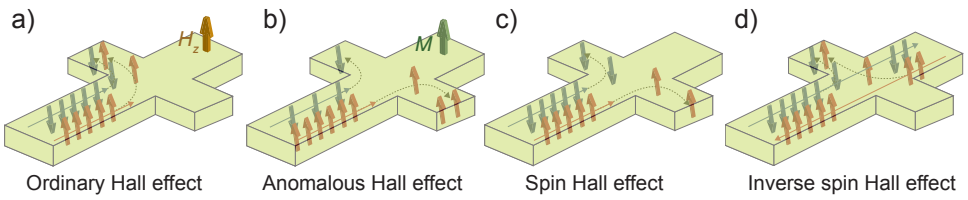

Figure 1.4: **Different Hall effects.** With a magnetic field applied out of plane: (a) Ordinary Hall effect (OHE), With the magnetization of the FM: (b) anomalous Hall effect (AHE). Without any magnetic field applied:(c) spin Hall effect (SHE) and inverse spin Hall effect (ISHE). Red (blue) arrows represent spin-up (spin-down) electrons and dotted lines their trajectories.

the SHE effect has an intrinsic contribution directly related to the band structure of the NM, and a second contribution due to impurities in the NM.

SHE can be used to generate pure spin currents [Fig. 1.2(d)] and the ISHE to detect them [Fig. 1.2(h)]. A key parameter for the SHE is the spin Hall angle θ_{SH}. θ_{SH} defines the efficiency of the charge-to-spin current conversion, which means how much pure spin current $\boldsymbol{j}_s$ is generated when a charge current $\boldsymbol{j}_c$ is applied into the NM. The equation for SHE reads:

$$\boldsymbol{j}_s = \frac{\hbar}{e}\theta_{SH}\boldsymbol{j}_c \times \boldsymbol{s} \tag{1.12}$$

Reciprocally, the ISHE can be written as:

$$\boldsymbol{j}_c = \frac{e}{\hbar}\theta_{ISH}\boldsymbol{j}_s \times \boldsymbol{s} \tag{1.13}$$

where $\boldsymbol{s}$ is the spin direction. Due to Onsager reciprocity, $\theta_{SH} = \theta_{ISH}$ [24]. θ_{SH} can be written in terms of the spin Hall conductivity σ_{SH} as follows:

$$\theta_{SH} = \frac{\sigma_{SH}}{\sigma_{xx}} \tag{1.14}$$

with σ_{xx} being the longitudinal conductivity of the material. Based on this definition, we can find in the literature materials with large θ_{SH}, which are usually heavy metals (HM) due to the strong SOC in these materials,for example, the theoretical work by Tanaka *et al.* [41] reported different intrinsic values for σ_{SH} in $4d$ and $5d$ transition metals. They show that Pt has the largest σ_{SH}. Up to date, Pt remains the most used material in (I)SHE experiments [32]. In this thesis,

Pt is used as a material with large θ_{SH} for the generation and detection of the spin current. It is worth stressing that we use exactly the same Pt systematically characterized in a previous report published by our group [42], where θ_{SH} and (λ_s) can be calculated from the Pt resistivity.

Once we have introduced the spin Hall effect in heavy metals, the next step is to introduce the magnetic insulator as the second element of the bilayers systems studied in this thesis.

1.4 Magnetic insulators

From a fundamental point of view, spintronics in magnetic insulators (MIs) is different than in metallic systems, because the transport of free-electrons are forbidden in these materials. However, there are plenty of spin-related effects where MIs play a crucial role, for instance spin pumping [43, 44], spin Seebeck effect [45, 46], spin Peltier effect [47], spin transfer torque [48] or magnon spin transport [19,20]. Before introducing the phenomena related to MIs, let us introduce the different magnetic orders present in magnetic materials.

Magnetism is a very complex subject and a detailed description is beyond the interest of this thesis. However, as a simple description, magnetic materials can be classified in two big groups; those with atoms without net magnetic moments, known as *diamagnetic*, and those with net magnetic moments. In this last group, the materials can be divided into the those without long-range order between magnetic moments, known as *paramagnetic* [Fig. 1.5(a)] and the ones with long-range order. Finally, the materials with long-range order can be distinguished according to the particular alignment that the magnetic atoms exhibit; (i) parallel, *ferromagnetic* [Fig. 1.5(b)], (ii) antiparallel, there are two cases: *antiferromagnetic* [Fig. 1.5(c)] and *ferrimagnetic* [Fig. 1.5(d)]. For an exhaustive discussion, one can refer to Ref. [49].

1.4.1 Paramagnetism

Most of the magnetic materials present a paramagnetic behavior. The main characteristics of paramagnetism is that there is no exchange interaction between the magnetic moments in the material. This means that, in thermal equilibrium and without any external magnetic field applied H, the magnetic moments are randomly oriented so that there is no net magnetization M [see Fig. 1.5(a) for $H \neq 0$]. In addition, in the presence of a magnetic field [Fig. 1.5(a) for $H > 0$], the magnetic moments partially align with H generating a net M, see magnetization

loop in Fig. 1.5(a). A prototypical example of paramagnetic insulator is *gadolinium gallium garnet* $Gd_3Ga_5O_{12}$ (GGG), material that we study in **Chapter 5**.

1.4.2 Ferromagnetism

Ferromagnetic materials are those materials that present a net M even at zero H, due to the spontaneous alignment of the magnetic moments in a preferred direction, see Fig. 1.5(b). This strong interaction that leads to the alignment of the magnetic moments is known as *exchange interaction* [50]. Figure 1.5(b) shows a typical magnetization loop for a ferromagnetic material where there is a net M at $H = 0$ T (after the first magnetization loop), the net M saturates when H is big enough and it shows a characteristic hysteresis when reversing H. These kind of materials show this behavior below the Curie temperature T_c. Above T_c, they behave as paramagnets because the thermal excitation is higher than the exchange interaction between the magnetic moments. For our specific purpose, we want to study a ferromagnetic insulator (FMI). However, FMIs are scarce materials and with quite low T_c, for instance EuS with a T_c of 16 K [51] or EuO with a T_c around 100 K [51]. In **Chapter 6**, we present the study on EuS/Pt interface.

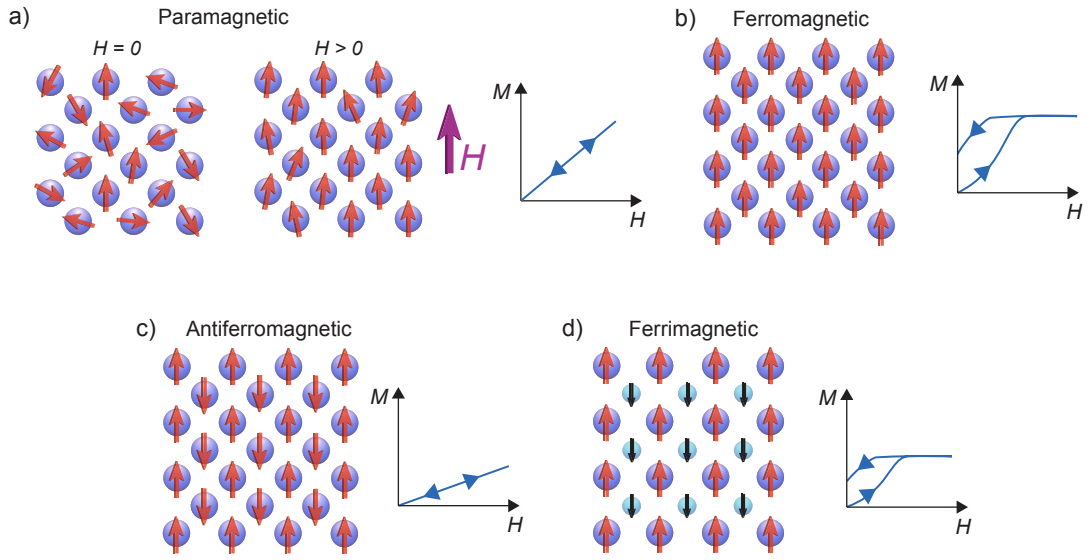

Figure 1.5: **Magnetic order.** (a) Paramagnetic order without (left) and with (right) an applied magnetic field. The plot is a sketch of a magnetization loop for a paramagnetic material. (b) Ferromagnetic, (c) antiferromagnetic and (d) ferrimagnetic orders with the corresponding plots showing their magnetization loops.

1.4.3 Antiferromagnetism and ferrimagnetism

Figures 1.5(c) and 1.5(d) show two magnetic order different from the previous ones. In these cases, the magnetic moments are preferably aligned antiparallel to each other in order to minimize the energy of the system. It can be described as two magnetic sublatices with an antiparallel alignment. When the net magnetization of each sublattice is the same, it leads to a zero M at zero H, which is known as antiferromagnetism [Fig. 1.5(c)]. Its magnetization loop is similar to the one of paramagnetic materials and it would be necessary to apply an externally large H in order to saturate it. When, the net magnetization of each sublattice is different, the system exhibits an spontaneous net M even at zero H, known as ferrimagnetism [Fig. 1.5(d)]. Its hysteresis loop is similar to the one of ferromagnets, but taking into account that one of sublattices is antiferromagnetically coupled, the net magnetization is reduced. A prototypical example of a ferrimagnetic insulator is *yttrium iron garnet* $Y_3Fe_5O_{12}$ (YIG), which is the most broadly used MI in spintronics experiments [19, 20, 52–56]. **Chapter 3** shows a study of Au/YIG interface and, in **Chapter 7**, we will study the propagation of magnons through YIG.

1.4.4 Spin waves and magnons

An interesting property of FM materials, in particular in MIs without free electrons, is that the spin currents are carried by quasiparticles known as spin waves or magnons. Ideally, in a static MI, all the magnetic moments point in the same direction without any perturbation, but it is only possible a zero T. However, the presence of any perturbation in the system leads to a collective precessional motion of the magnetic moments, due to the strong exchange interaction between them, in order to reduce the energy of the system [Fig. 1.6(a)]. These collective spin wave excitations carry a $\boldsymbol{j}_s$ with the spin polarization along the average magnetization direction of the MI, and can be generated, for instance, by applying a microwave, but it can be also thermally or electrically excited as we will show in Sections 1.5.3 and 1.5.6

In a simple situation, the spins are coupled with the nearest neighbor spin via exchange interaction, let us consider that only the nearest neighbor interaction is the important one, then, the Hamiltonian is:

$$\mathcal{H} = -2J \sum_{(i,j)} \boldsymbol{s_i} \cdot \boldsymbol{s_j} - g\mu_B \boldsymbol{H} \sum_i s_{iz} \tag{1.15}$$

where J is the exchange interaction ($J > 0$, for a ferromagnet), $\boldsymbol{s_i}$ represents

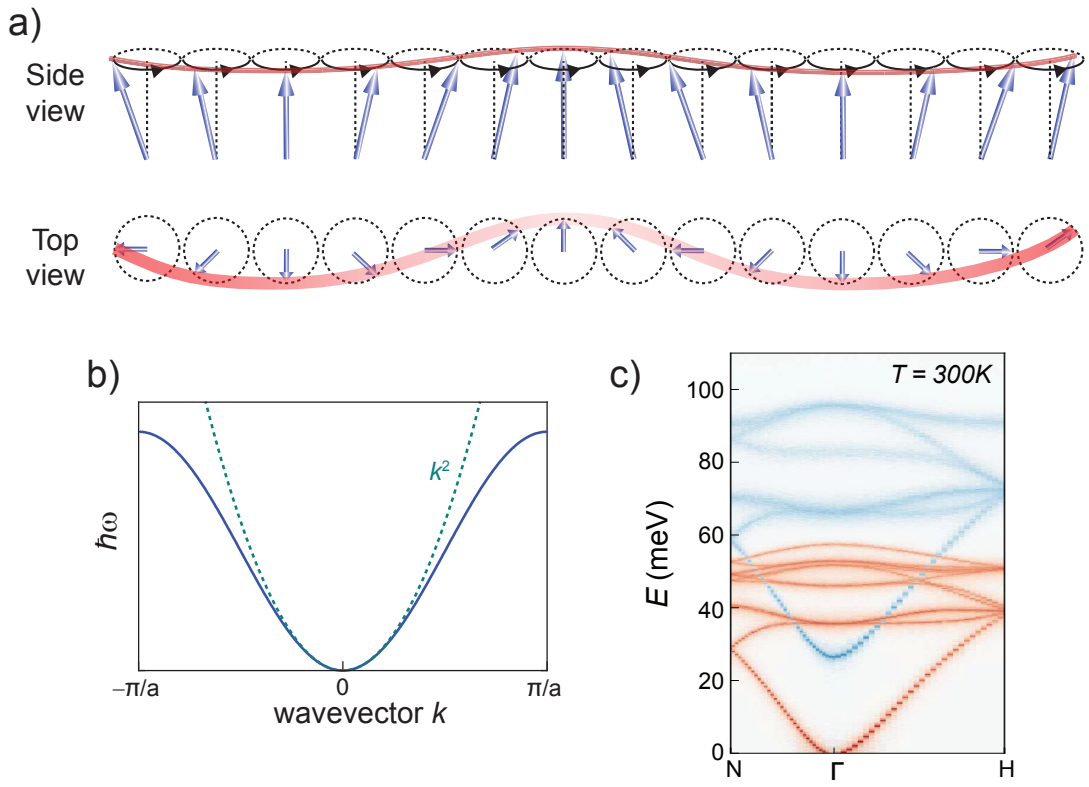

Figure 1.6: **Spin waves.** (a) Side and top views of spin waves (magnons) in magnetic insulators. Figure adapted from Ref. [12]. (b) Magnon dispersion for a simple system. (c) Magnon dispersion calculated for YIG, where the red and blue bands represent the two different magnetic sublattices in YIG. Figure adapted from Ref. [57].

the spin operator of an atom or an ion at the position i and the second term represents the Zeeman energy, where g is the $g-$factor, μ_B the Bohr magneton and $\boldsymbol{H}$ the magnetic field. The dynamics equation is

$$\frac{d\boldsymbol{s_j}}{dt} = \frac{i}{\hbar}[\mathcal{H}, \boldsymbol{s_j}] = -\frac{1}{\hbar}(\boldsymbol{\epsilon_j} \times \boldsymbol{s_j}) \tag{1.16}$$

where

$$\boldsymbol{\epsilon_j} = 2J \sum_{i \neq j} \boldsymbol{s_i} + g\mu_B \boldsymbol{H} \tag{1.17}$$

which is defined as the effective magnetic field acting on $\boldsymbol{s}_j$. The eigenfrequency of the dynamics equation is (for further details in the calculation, see Ref. [12]):

$$\hbar\omega_{\mathbf{k}} = 2JsZ(1 - \gamma_{\mathbf{k}}) + g\mu_B \boldsymbol{H} \tag{1.18}$$

where s is the total spin of the system, Z is the number of nearest neighbors, $\gamma_{\mathbf{k}}$ is a vector that depends on the wavevector $\boldsymbol{k}$. The eigenfrequency show the whole spin configuration of a crystal that behaves as an oscillatory motion with frequency $\omega_{\mathbf{k}}$ and wavevector $\boldsymbol{k}$. As an example and for simplicity lets us consider a cubic lattice with a distance a between atoms, then $\gamma_{\mathbf{k}} = (1/3)(\cos \boldsymbol{k}_x a + \cos \boldsymbol{k}_y a + \cos \boldsymbol{k}_z a)$, if we consider the simplest case for small $\boldsymbol{k}$ the dispersion relation for magnons has a quadratic behavior:

$$\hbar\omega_k = g\mu_B H + 2Jsa^2k^2 \tag{1.19}$$

Figure 1.6(b) shows the simplest magnon dispersion where, it follows a quadratic behavior at small $\boldsymbol{k}$. However, for a real crystal, the magnon dispersion is more much complicated, as it can be seen in Fig. 1.6(c) for the particular case of YIG. Magnon dispersion is complex and, depending on the way magnons are generated, they can have different energies and thus, different frequencies. This leads to different behaviors with the temperature and in the presence of an external magnetic field as we will show in **Chapter 7**.

1.5 Spin-dependent phenomena at heavy metal/magnetic insulator heterostructures

Finally, we have defined both ingredients for our heavy metal (HM)/magnetic insulator (MI) heterostructures. The spin transport at the interface is at the heart of several spin-dependent phenomena occurring in HM/MI systems and, in the following sections, we introduce the most relevant phenomena.

1.5.1 Spin transport at non-magnetic/ ferromagnetic interfaces

In section 1.1.1, we have introduced the concept of pure spin current by the *two-current model* that considers two independent channels for spin-up and spin-down electron. There is an analogue model for studying the spin transport at NM/FM interfaces, known as magnetoelectronics circuit theory [58]. This theory describes the spin transport across the interface in terms of four conductance parameters. The first two conductances are the spin-up and spin-down conductances that govern the longitudinal spin and charge transport. These two conductances would be enough for explaining the spin transport in collinear magnetoelectronics (ideal case such as GMR spin valves). Nonetheless, for non-collinear cases, in the

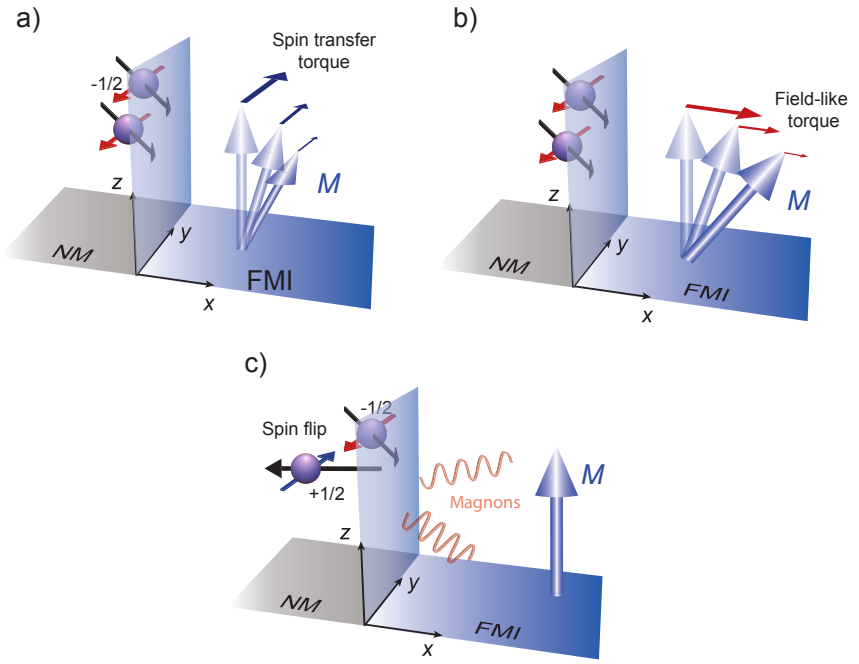

Figure 1.7: **Spin mixing conductances mechanisms.** Sketches of the spin-mixing conductances mechanisms: (a) spin transfer torque related to G_r and (b) field-like torque related to G_i. (c) The sketch shows the spin-flip mechanism related to spin-sink condcutance G_s, close related to the excitationof magnon in a FM.

2×2 unitary conductance matrix the non-diagonal elements appears; so called *spin-mixing conductance*, that governs the transverse spin currents at NM/FM interfaces. They are called 'mixing' because they connect the two "independent spin channels", and the spin-mixing conductances are material parameters independent of the spin-dependent conductances, being a pure interfacial property. The real and imaginary part of the spin-mixing conductance $G_{\uparrow\downarrow}$ determine the transverse spin current. Its physical meaning is the transfer of angular momentum from a spin accumulation in the NM to the FM. Therefore, the transport of the spin transport through a NM/FM interface is given by:

$$-e\boldsymbol{J}_{s,z} = G_s\boldsymbol{\mu_S} + G_r\boldsymbol{m}\times[\boldsymbol{m}\times\boldsymbol{\mu_S}] + G_i\boldsymbol{m}\times\boldsymbol{\mu_S} \tag{1.20}$$

where G_s is the spin-sink conductance (a.k.a. effective spin conductance), G_r and G_i are the real and imaginary terms of the spin-mixing conductance ($G_{\uparrow\downarrow} = G_r + iG_i$), $\boldsymbol{\mu_S}$ the spin accumulation at the interface and $\boldsymbol{m}$ is an unity vector pointing in the magnetization direction. The first term of the pure spin current depends on G_s, which is related to the spin-flip scattering at the interface playing an important role for the excitation of magnons in the FM [Fig. 1.7(c)] [20, 56]. G_r is related to the *anti-damping torque* (or spin-transfer Slonczewski torque)

that the spin accumulation exerts to M of the FM, and controls the direction of M, see Fig. 1.7(a). Thus, it is promising for the application in magnetic random-access memories [59]. On the other hand, G_i describes the precession of the spin accumulation around the M direction, Fig. 1.7(b). G_i acts as a *field-like torque* that also transfers an angular momentum to M, equivalent to an effective magnetic field parallel to the spin accumulation at the interface. We have introduced the general spin-mixing conductance in NM/FM interfaces, however, it can be also applied to the case in which the FM is a FMI [19, 48, 60].

As explained above, the spin-mixing conductance governs the spin transport through the interfaces and it is thus a crucial parameter for well-known spin-dependent phenomena occurring at NM/FM systems, such as *spin pumping*, *spin Seebeck* effect (SSE) or *spin Hall magnetoresistance* (SMR). In 2013, M. Weiler *et al.* performed the first experimental test of the quantification of the spin-mixing conductance simultaneously using different phenomena: spin pumping [Fig. 1.8(a)], SSE [Fig. 1.8(b)], and SMR [Fig. 1.8(c)], for different thicknesses of YIG. They found that the obtained spin-mixing conductance value corresponding to each experiment is the same for all cases [Fig. 1.8(d)], validating the spin-mixing conductance concept. In the following sections, further details on spin pumping, SSE and SMR are given.

1.5.2 Spin pumping

Spin pumping is one of the first techniques used for the generation of pure spin currents from a FM into an adjacent NM using magnetization dynamics, such as magnetization precession caused by ferromagnetic resonance (FMR). The first realization of spin pumping in 2002 was presented only to detect an enhancement in the magnetization damping [43], and explained theoretically by Tserkovnyak *et al.* in the same year [44]. Four years later, Saitoh *et al.* electrically detected spin pumping in a heavy metal adjacent to the FM by ISHE [40]. The working principle of spin pumping is related to FMR, where a spin angular momentum is continuously transferred from external microwaves to the FM, inducing magnetization precession. When the FM is in contact with a NM, the spin angular momentum can flow into the NM through the interface, creating a pure spin current into the NM, see Fig. 1.9(a). This spin current into the NM can then be detected by different means. The most common one is that the NM is a HM, and the corresponding ISHE converts the spin current into a transverse charge current. Figure 1.9(b) shows the typical measurements performed in spin pumping reproduced from Ref. [62]. The top and middle plots show the FMR microwave absorption spectra for Py and Py/Pt at $\mu_0 H = 200$ Oe, with a *ac* field with a 4 GHz frequency. The bottom plot shows the *dc* voltage measured as a function of

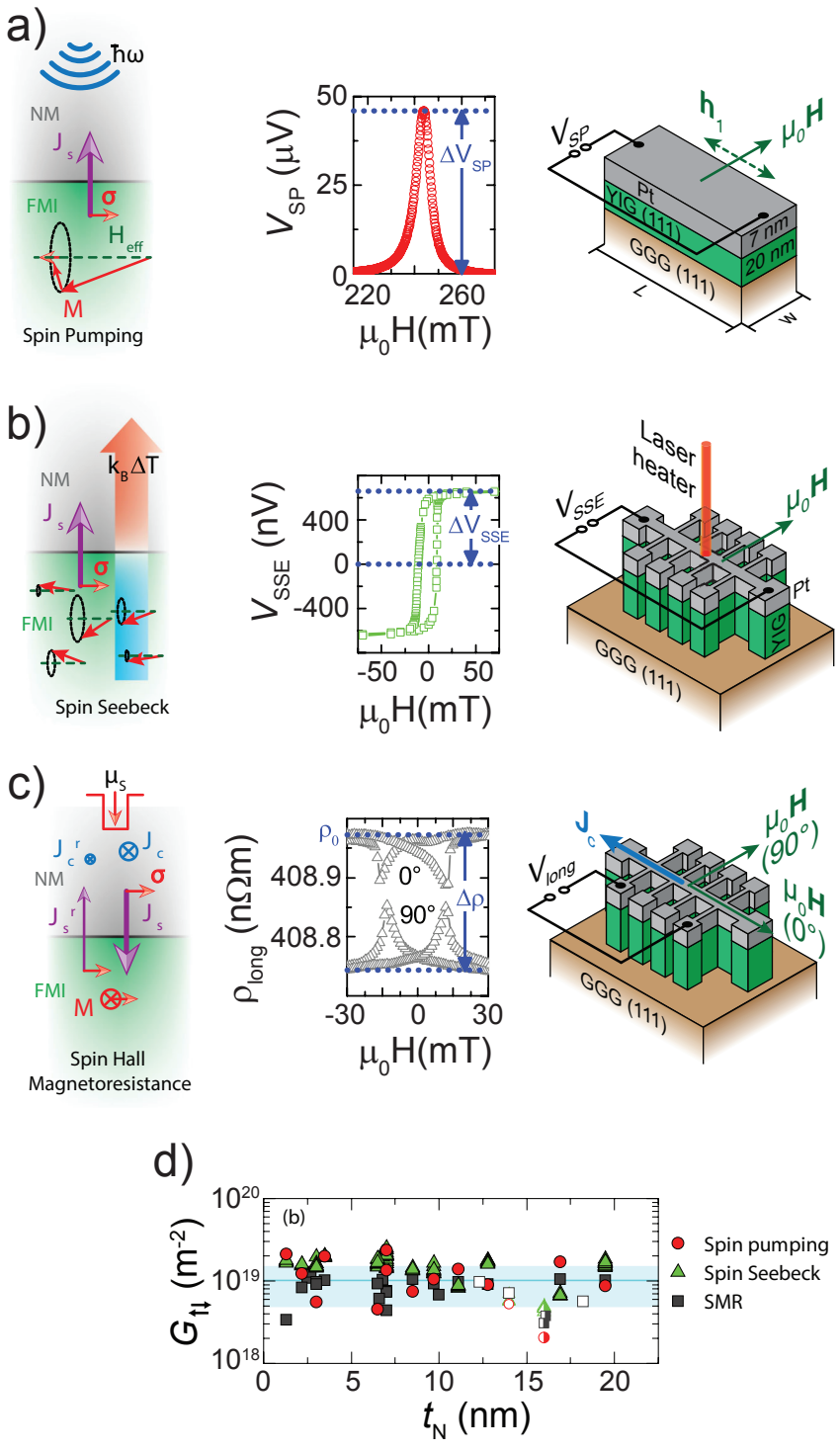

Figure 1.8: **Comparison of spin pumping, spin Seebeck effect and spin Hall magnetoresistance.** Mechanism, voltage measured by ISHE, and measurement configuration for (a) spin pumping, (b) spin Seebeck effect, and (c) spin Hall magnetoresistance. (d) Spin-mixing conductance as a function of the YIG thickness for the different experiments. Figure adapted from Ref. [61].

the external $\mu_0 H$ compared to Py and Py/Pt FMR spectra. From these voltages, one can see that there are two contributions, (i) a signal coming from ISHE in Pt and (ii) a signal with the same origin than that in the Py control sample (black triangles).

Therefore, the interface plays a crucial role in spin pumping experiments. The magnitude of the pumped spin current into the NM depends on the quality of the HM/FM interface and it is clearly related to the spin-mixing conductance. In this case, the spin current depends on the spin-mixing conductance as follows

$$\boldsymbol{j}_s \boldsymbol{s} = \frac{\hbar}{e}\left(G_r \boldsymbol{m} \times \frac{d\boldsymbol{m}}{dt} + G_i \frac{d\boldsymbol{m}}{dt}\right) \tag{1.21}$$

where $\boldsymbol{s}$ is the spin polarization and $\boldsymbol{m}$ an unity vector pointing in the magnetization direction. Spin pumping was the starting point for the study of HM/MI interfaces.

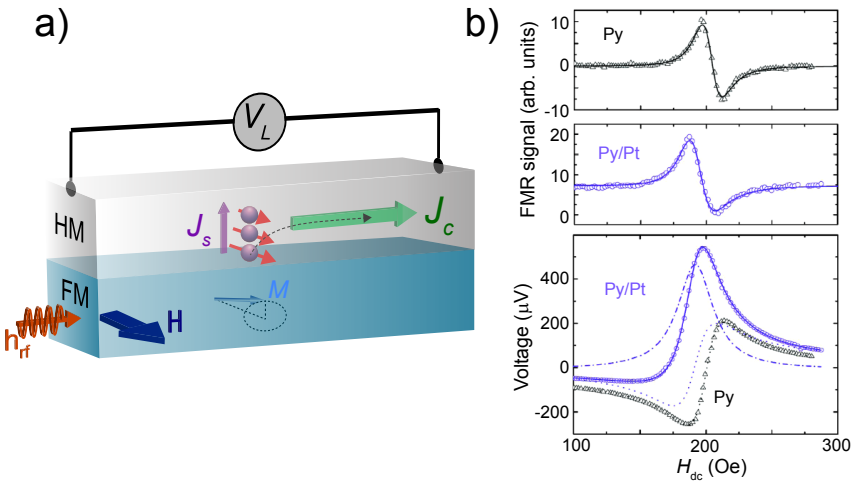

Figure 1.9: **Spin pumping.** (a) Spin pumping technique to generate a pure spin current in an adjacent heavy metal, a voltage can be detected by ISHE. H is the *dc* applied magnetic field and h_{rf} is the *ac* applied magnetic field. (b) Top and medium panel, FMR spectra for Py and Py/Pt. Bottom: Voltage measured along the sample vs the *dc* magnetic field. Figure adapted form Ref. [62].

1.5.3 Spin Seebeck effect

The field of thermoelectricity studies the coupling between the charge and heat. In 1821, Thomas Seebeck discovered an important effect, the Seebeck effect [63]. The basis of this effect is that a temperature gradient ∇T in a conductor turns into a voltage along the applied ∇T, and the voltage is proportional to the Seebeck coefficient, $\nabla V = -S\nabla T$. The physics behind the effect is based on the different conductivities of the electrons between the hot side of the material and the cold side. This effect is broadly used for termocouples.

We are interested in effects related to HM/FMI interfaces, and, in this case, a ∇T can also induce a voltage and this is why this effect is known as spin Seebeck effect (SSE). However, the mechanism of SSE is completely different to the one of Seebeck effect because it is driven by magnons instead of electrons. The density of magnons depends directly on the temperature. Therefore, when a thermal

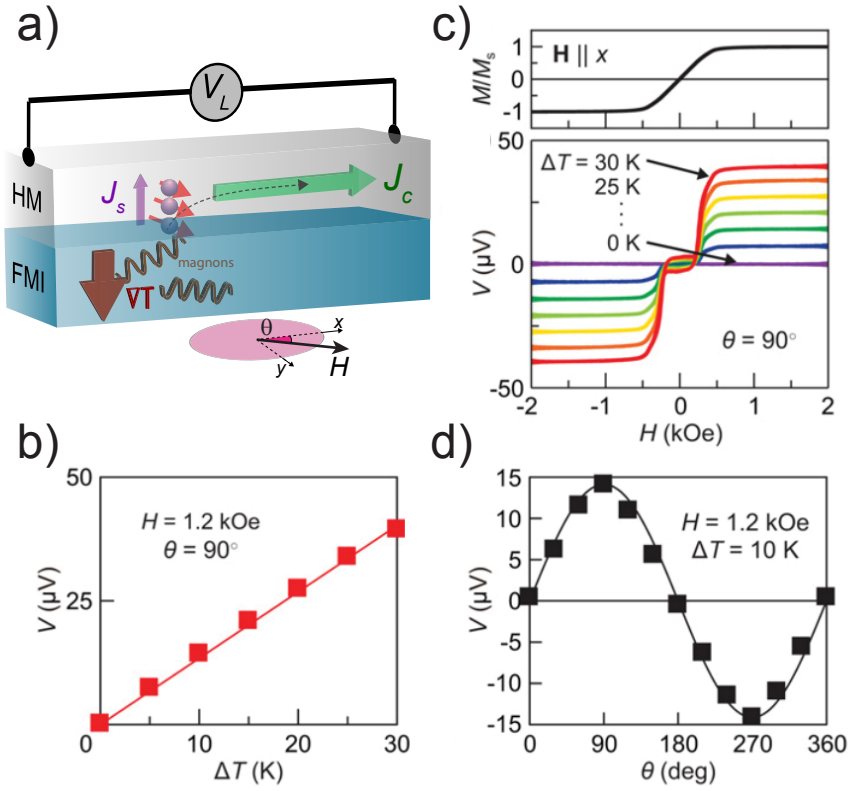

Figure 1.10: **Spin Seebeck effect.** (a) Spin Seebeck effect, where a thermal gradient (∇T) induces a magnon accumulation at the HM/FMI interface that can be detected by ISHE. (b) Linear dependence of the output voltage with applied ∇T. (c) Field-dependent measurement for YIG magnetization (top) and output voltage. (d) Angular-dependent measurement when the magnetic field is swept in the plane of the substrate. Figures (c-d) adapted from Ref. [64].

gradient $\boldsymbol{\nabla} T$ is applied in the FMI, the T difference in the MI induces a difference in the magnon density between top and bottom surface is induced, thus, drives to a magnon diffusion current into the FMI, see Fig. 1.10(a). In order to measure the effect a HM/FMI interface is necessary, because the magnon accumulation at the interface will interact with the electron-spins of the HM, inducing a pure spin current on the HM, which is then converted into a transverse voltage due to ISHE [46]. Therefore, once again the spin-mixing conductance of the interface is crucial for the generation of the spin current into the HM. As described in Ref. [55]:

$$V_{ISHE} = \sigma_{SSE} \nabla T \tag{1.22}$$

where V_{ISHE} is the ISHE voltage detected due to spin accumulation generated at HM/MI interface by SSE, σ_{SSE} is the spin Seebeck coefficient and directly depends on the spin-sink conductance (G_s).

Figure 1.10(a) shows the measurement configuration for the SSE at a HM/FMI bilayer. SSE experiments show a linear dependence of the ISHE voltage as function with the temperature gradient (Fig. 1.10(b) and Eq. 1.22). Second, Fig. 1.10(c) shows the magnetic field dependence of V_{ISHE}, where it can be seen that the voltage signal directly depends on the M orientation of the FMI, to polarized the electrons in the HM, they have to be parallel to M. Finally, Fig. 1.10(d) plots the angular-dependence of the V_{ISHE} with the field, showing the expected $sin(\theta)$ dependence taking into account the configuration of the effect [64].

1.5.4 Spin Hall magnetoresistance

In section 1.3, we introduced the SHE and ISHE present in materials with strong spin-orbit coupling, such as Pt, Pd, Ta or W. When a charge current is flowing along a HM thin film, a transverse pure spin current is induced due to the SHE. The electrons at the edge bounce into the HM inducing an extra charge current $\boldsymbol{j}_c^{'}$,via ISHE, parallel to the one applied. Therefore, there is a reduction of the Drude resistivity due to the correction that scales with the square of θ_{SH}, see Eq. 1.25. In the case of a HM in contact with a FMI, because of $\boldsymbol{j}_s$, a spin accumulation will build at the HM/FMI interface, with a spin orientation $\boldsymbol{s}$ perpendicular to the applied $\boldsymbol{j}_c$. The electron-spins will interact with the magnetic moments of the MI and, depending on the relative orientation of its magnetization, the electron-spin will:

- be reflected into the HM at the interface when $\boldsymbol{s}$ and M are parallel. Thus,

the electron-spin reflected will induce an extra charge current $\boldsymbol{j}_c^{'}$ by ISHE reducing the resistivty of the HM, see Fig. 1.11(a).

- be absorbed into the FMI by exerting a torque to M when $\boldsymbol{s}$ and M are perpendicular. In this case, the electron-spin will not be reflected back and no extra charge current by ISHE will be generated, increasing the resistivity of the HM, see Fig. 1.11(b).

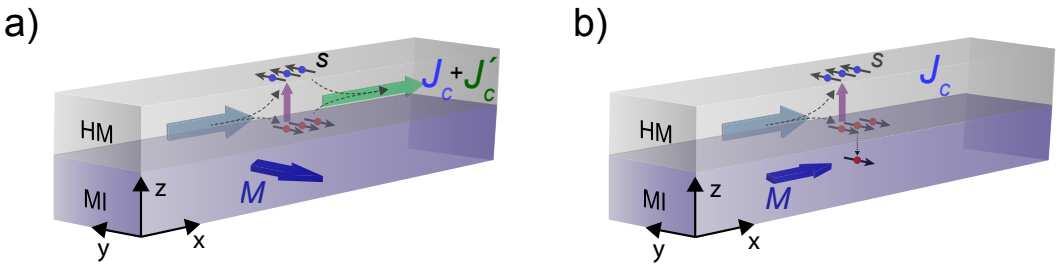

Figure 1.11: **Spin Hall magnetoresistance symmetry.** Spin Hall magnetoresistance; (a) low resistance state and (b) high resistance state.

This effect is called spin Hall magnetoresistance (SMR), and it was firstly reported theoretically by Y-T. Chen *et al.* [65], and experimentally by H. Nakayama *et al.* in Pt/YIG bilayers [66]. At the time of the publication of these works, there was a controversy about the origin of SMR, because one report by S. Y. Huang *et al.* [67] claimed that the origin of the magnetoresistance in Pt was due to a magnetic proximity effect (MPE) in Pt induced by YIG [68]. When Pt is in contact with a FM, Pt can become ferromagnetic showing anisotropic magnetoresistance (AMR) and anomalous Hall effect (AHE) that would mirror the M of the adjacent FM [67, 69–71]. While MPE in Pt with a metallic FM, such as Co, is well established by X-ray magnetic circular dichroism (XMCD) [72, 73], the same effect in YIG and other FMI has led to mostly negative results [74–76]. In spite of the controversy, it is easy to distinguish the SMR scenario from the MPE scenario, because the SMR symmetries are clearly different than those of MPE, by performing the typical angular-dependent magnetoresistance (ADMR) measurements in the three main $H-$rotating planes.

Therefore, we need to define first the longitudinal and transverse resistivities of the HM as a function of magnetization direction. In the first theory of SMR, Y-T. Chen *et al.* described the SMR resistivities as follows [65]:

$$\rho_L = \rho + \Delta\rho_0 + \Delta\rho_1 \left(1 - m_y^2\right) \tag{1.23}$$

$$\rho_T = \Delta\rho_1 m_x m_y + \Delta\rho_2 m_z \tag{1.24}$$

where ρ_L and ρ_T are the longitudinal and transverse resistivities, respectively, $\boldsymbol{m}(m_x,m_y,m_z)$ are the normalized projections of the magnetization of the FMI layer to the three main axes. ρ is the inverse of the Drude conductivity $\sigma = 1/\rho$, $\Delta\rho_0$ accounts for a resistivity correction due to the spin Hall effect [77], and $\Delta\rho_1$ and $\Delta\rho_2$ are the SMR amplitudes, which are defined as:

$$\Delta\rho_0 = -\theta_{SH}^2 \frac{2\lambda}{d_N} \tanh \frac{d_N}{2\lambda} \tag{1.25}$$

$$\frac{\Delta\rho_1}{\rho} = \theta_{SH}^2 \frac{\lambda}{d_N} \Re \left[\frac{2G_{\uparrow\downarrow} \tanh^2 \frac{d_N}{2\lambda}}{\sigma + 2\lambda G_{\uparrow\downarrow} \coth \frac{d_N}{2\lambda}} \right] \tag{1.26}$$

$$\frac{\Delta\rho_2}{\rho} = -\theta_{SH}^2 \frac{\lambda}{d_N} \Im \left[\frac{2G_{\uparrow\downarrow} \tanh^2 \frac{d_N}{2\lambda}}{\sigma + 2\lambda G_{\uparrow\downarrow} \coth \frac{d_N}{2\lambda}} \right] \tag{1.27}$$

where θ_{SH}, λ, d_N and σ are the spin Hall angle, spin diffusion length, thickness and conductivity of the Pt, respectively, and $G_{\uparrow\downarrow} = G_r + iG_i$ is the spin mixing conductance. In this simple theory G_s was neglected. Therefore, the SMR amplitudes $\Delta\rho_1$ and $\Delta\rho_2$ only depend on the HM parameters and the spin-mixing conductance at the interface.

Figure 1.12 shows SMR measurements previously performed in Pt/YIG in our group [54]. First of all, it is necessary to apply H large enough to saturate M. Figure 1.12 (a) shows ADMR measurements. In $\alpha-$ and $\beta-$planes, the M is swept from parallel to perpendicular to the spin polarization having a sin^2 of the angle modulation, which can be understood by Eq. 1.23, where the longitudinal resistivity only depends on the M projection in $y-$direction. The amplitude is defined by $\Delta\rho_1$, which means that the amplitude of the SMR for $\alpha-$ and $\beta-$planes is the same, $\Delta\rho_L(\alpha) = \Delta\rho_L(\beta)$. On the other hand, in $\gamma-$plane, M rotates always perpendicular to the spin orientation, resulting in a high resistance state with no modulation with the angle, as predicted again by Eq. 1.23 (ρ_L depends on y component of the magnetization and $\gamma-$plane corresponds to $xz-$rotating plane). Fig. 1.12(a) also plots the transverse ADMR for $\alpha-$plane that is described by Eq. 1.24, which depends on $x-$ and $y-$ magnetization projections and the amplitude is given by $\Delta\rho_1$, which means that the SMR amplitude measured in transverse ADMR is the same than that measured in longitudinal configuration. These angle

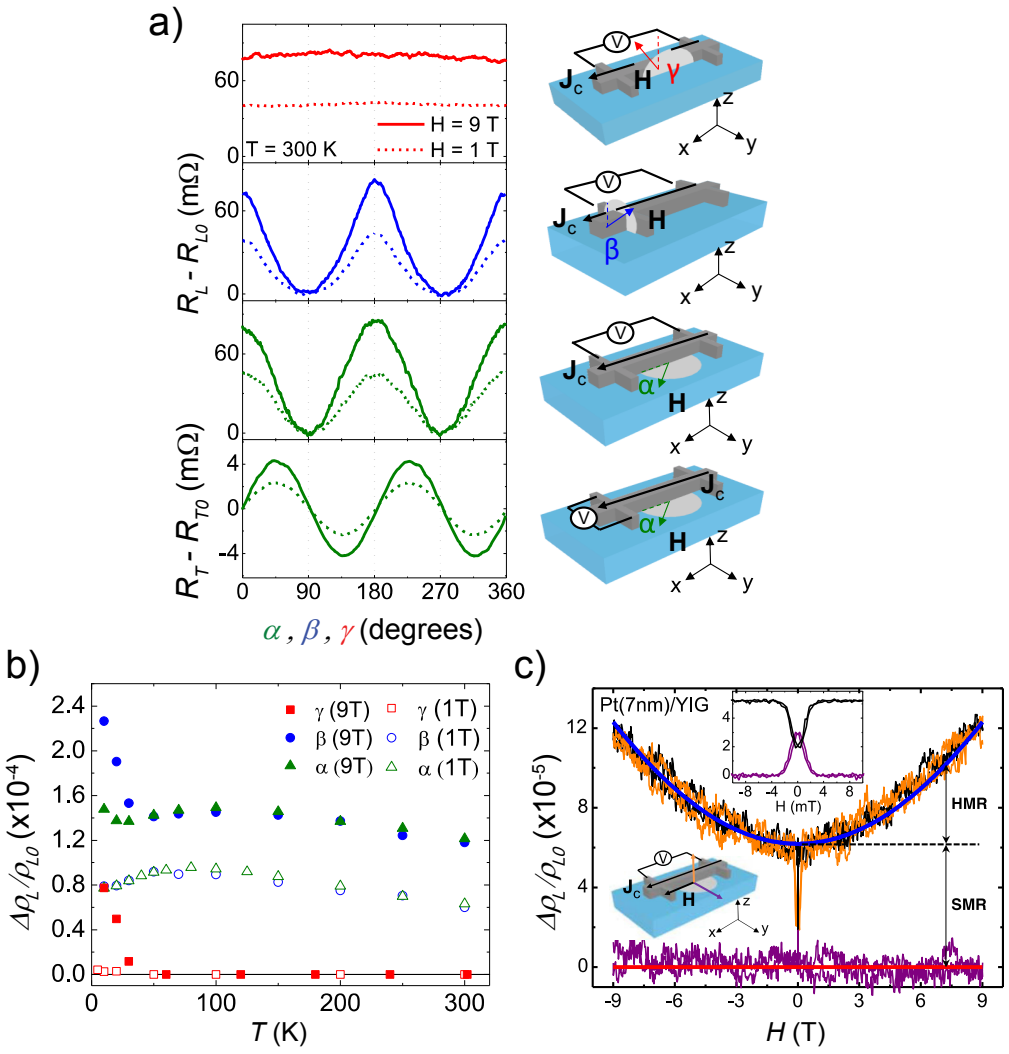

Figure 1.12: **Angular-dependent and field-dependent magnetoresistance measurements.** (a) ADMR measurements in Pt(7 nm)/YIG at 300 K and 1 T (dashed lines) or 9 T (solid lines) in three relevant $H-$rotation planes (α,β,γ). Sketches on the right side indicate the definition of the angles, axes and measurement configurations. (b) Temperature dependence of the longitudinal normalized ADMR at 1 T and 9 T, for the three $H-$rotation planes. (c) Normalized FDMR measurement performed along the three main axes at 300 K. The colors define the direction of H, orange for H_z, black for H_x, and purple for H_y. Inset: zoom at low H. Figure extracted from Ref. [54].

dependencies are unique to SMR. Figure 1.12(b) illustrates the T dependence for ADMR amplitudes showing the same amplitude and dependence with T, for $\alpha-$ and $\beta-$ planes. At very low T, there is a sharp increase of the amplitude while decreasing T. This phenomenon is due to the weak antilocalization in Pt [78], where the resistance with H_z is larger than the resistance with H_x and H_y. In the case of the field-dependent magnetoresistance (FDMR) measurement (Fig. 1.12(c)), when H is high enough, YIG is completely saturated having the SMR

amplitude as it is presented in Fig. 1.12(c). As expected for SMR, $R(H_x) = R(H_z) > R(H_y)$, which means that $R(H_x)$ $[R(H_z)]$ and $R(H_y)$ represent a high and low resistance states according to SMR symmetries. In the inset of Fig. 1.12(c) is presented the longitudinal FDMR measured in $x-$ and $y-$directions at very small magnetic fields, close to zero H, the resistance in $x-$direction decreases whereas in $y-$direction increases, which is related to the breaking into domains the M of the MI. Therefore, by SMR measurements, we can study the surface magnetic properties of the MI.

In addition, at very large H_x and H_z, an extra magnetoresistance with a clear parabolic dependence with H shows up [Fig. 1.12(c)]. This effect only appears in $x-$ and $z-$direction where the spin accumulation is perpendicular to H, but it does not appear in $y-$direction because H_y and the spin accumulation are collinear. Therefore, the symmetries are the same as those of SMR but in this case the spin accumulation interacts with H instead of the FMI magnetization. The effect is related to the precession of the spin accumulation around the external H, when it is large enough. This phenomenon is known as Hanle magnetoresistance [54].

We have described the typical measurements performed in SMR for HM/FMI heterostructures. As showed in Eqs. 1.25−1.27, the SMR amplitudes just depend on the HM parameters and the spin-mixing conductance. Therefore, if we can measure the SMR amplitudes we can extract the spin-mixing conductance. $\Delta\rho_1$ can be extracted from longitudinal and transverse ADMR, Eqs. 1.23 and 1.24. A second term appears in transverse resistivity when the magnetic field is applied out-of-plane, known as the anomalous Hall effect-like (AHE-like) second term of Eq. 1.24. The amplitude $\Delta\rho_2$ of this term depends on θ_{SH}^2 instead of θ_{SH} and it is not related to a ferromagnetic metal or the magnetic proximity effect in the HM. Although it is present in all HM/MI interfaces, $\Delta\rho_2$ is much complicated to measure than $\Delta\rho_1$, because the ordinary Hall effect (OHE) background in the HM is huge as compare to the AHE-like feature. Even if $\Delta\rho_2$ is difficult to measure, there are particular examples where the spin-mixing conductance can be studied without $\Delta\rho_2$, the best example is the case of YIG where it has been reported that G_r is at least one order of magnitude larger than G_i [48, 79, 80]. Therefore, simplifying Eq. 1.26, $\Delta\rho_1$ only depends on G_r. Thus, by extracting $\Delta\rho_1$ from the ADMR amplitude (Fig. 1.12(a)) and the Pt parameters θ_{SH} and λ_s that can be calculated from Ref. [42], we are able to quantify the real part of the spin-mixing conductance. This value varies from group to group, but it is in the $10^{12} - 10^{14}$ $\Omega^{-1}\mathrm{m}^{-2}$ range [66, 79–83]. Nonetheless, this does not mean that the AHE-like component is not present in Pt/YIG heterostructures, as we will show in **Chapter 3** for Pt/YIG and Au/YIG systems. In addition, the AHE-like contribution can be easier to measure if G_i is large enough, as we will show in

Chapters 5 and **6**.

1.5.5 Microscopic theory of SMR

Recently, the theory of SMR from a microscopic point of view has been published by X.-P. Zhang *et. al.* [84], which can be generalized to any magnetic insulator (MI) beyond FMI. The theory considers the spin transfer at a HM/MI interface *via* the interfacial exchange interaction between the conduction electron-spins in the HM and the localized spins at the MI, where the MI does not need to have long-range magnetic order. As a result of the interfacial exchange interaction, the spin relaxation time of the conduction electron in HM becomes anisotropic ($\tau_{\parallel} \neq \tau_{\perp}$), leading naturally to SMR. The microscopic theory expresses the spin-mixing conductances in terms of the microscopic parameters related to the interface and the spin-spin correlation functions of the local moments at the surface of the MI. This theory is very useful in order to study the temperature (T) and field dependence of the different terms of the spin-mixing conductance, because the original SMR theory [65] considers that M is fixed and, since there is no T nor H dependence the spin-mixing conductances are constant. The spin current at the HM/MI interfaces is given by Eq. 1.20. In this theory, the spin-sink conductance G_s, which is related to the spin-flip scattering at the HM/MI interface, is also included. The spin conductance terms are defined as a function of the microscopic parameters as follows

$$G_r = e^2 \nu_F \left(\frac{1}{\tau_{\perp}} - \frac{1}{\tau_{\parallel}} \right) \tag{1.28}$$

$$G_i = -\frac{e^2}{\hbar} n_{imp}^{2D} \nu_F J_{sd} \langle \widehat{S}_{\parallel} \rangle \tag{1.29}$$

$$G_s = -e^2 \nu_F \frac{1}{\tau_{\parallel}} \tag{1.30}$$

where ν_F is the density of the electronic states per spin species in the HM, n_{imp}^{2D} is the number of local moments per unit area at the HM/MI interface, J_{sd} is the exchange interaction between the electron-spin in the Pt and the magnetic moments of the MI, $\widehat{S}_{\parallel}$ is the longitudinal spin operator of a representative local moment, and $\langle \widehat{S}_{\parallel} \rangle$ is the spin expectation value, which is the projection of the localized moment parallel to H. In addition, $\tau_{\parallel}$ and $\tau_{\perp}$ are the longitudinal and transverse spin relaxation times per unit length for the itinerant electrons, and are defined as:

$$\frac{1}{\tau_{\parallel}} = \frac{2\pi}{T} n_{imp}^{2D} \nu_F J_{sd}^2 \omega_L^m n_B\left(\omega_L^m\right)\left[1 + n_B\left(\omega_L^m\right)\right] |\langle \widehat{S}_{\parallel} \rangle| \tag{1.31}$$

$$\frac{1}{\tau_{\perp}} = \frac{1}{2\tau_{\parallel}} + \frac{\pi}{\hbar} n_{imp}^{2D} \nu_F J_{sd}^2 \langle \widehat{S}_{\parallel}^2 \rangle \tag{1.32}$$

where T is the temperature, $n_B(\omega) = 1/\left(e^{\hbar\omega/T} - 1\right)$ is the Bose-Einstein distribution function, $\omega_L^m = \omega_B \langle \widehat{S}_{\parallel} \rangle \Sigma_j J_{ij}/\hbar$ with J_{ij} being the coupling constant of the Heisenberg ferromagnet, $\omega_B = g\mu_B B/\hbar$ with μ_B the Bohr magneton, and $\langle \widehat{S}_{\parallel}^2 \rangle$ is the spin-spin correlation function obtained from $\widehat{S}_{\parallel}$. Then, the SMR amplitudes can be described as a function of the microscopic parameters as

$$\frac{\Delta\rho_1}{\rho} = \theta_{SH}^2 \{\mathfrak{F}(G_s, \lambda) - \Re\left[\mathfrak{F}(G_s - G_{\uparrow\downarrow}, \Lambda)\right]\} \tag{1.33}$$

$$\frac{\Delta\rho_2}{\rho} = \theta_{SH}^2 \Re\left[\mathfrak{F}(G_s - G_{\uparrow\downarrow}, \Lambda)\right] \tag{1.34}$$

where $\frac{1}{\Lambda} = \sqrt{\frac{1}{\lambda^2} + i\frac{1}{\lambda_m^2}}$ with $\lambda_m = \sqrt{\frac{D\hbar}{g\mu_B|B|}}$, D the diffusion coefficient of the HM, g the gyromagnetic factor and the auxiliary function $\mathfrak{F}(G,\lambda)$ is defined as

$$\mathfrak{F}(G, \lambda) = \frac{2\lambda}{d_N} \tanh\left(\frac{d_N}{2\lambda}\right) \frac{1 - \rho G \lambda \coth\left(\frac{d_N}{2\lambda}\right)}{1 - 2\rho G \lambda \coth\left(\frac{d_N}{2\lambda}\right)} \tag{1.35}$$

Equations 1.33−1.34 include the correction from G_s to the SMR amplitudes and the Hanle magnetoresistance contribution through λ_m, and recovery Eqs. 1.26−1.27 when $G_s = 0$, which correspond to the same boundary condition used by Chen *et. al.* [65].

Up to now, we have introduced the SMR amplitudes, the spin-sink and the spin-mixing conductance terms. This theory describes the physics behind any HM/MI interface, independently of the magnetic order of MI. Therefore, G_s originates from the spin-flip processes and can be associated to the creation and absorption of magnons. $G_r - 1/2 G_s$ is proportional to $\langle \widehat{S}_{\parallel}^2 \rangle$, which is the dephasing contribution and it originates from the elastic spin-scattering processes, which do not involve any exchange of angular momentum with the MI because it is elastic. Finally, G_i represents exchange field at the interface and it is proportional to $\langle \widehat{S}_{\parallel} \rangle$.

Figure 1.13 shows an example of the magnetic field $B(\mu_0 H)$ dependence for the spin conductances for a paramagnetic insulator (PMI), and the T dependence for a FMI with a $T_c = 100$ K. It can be seen that G_s tends to zero and G_r tends to saturate when M saturates (i.e. high field or low temperatures), and we can clearly see that in both cases, G_i follows the very same trend as M (Fig. 1.13(a) and Fig. 1.13(b)).

This microscopic theory developed by our collaborators X.-P. Zhang, S. Bergeret and V. N. Golovach is really useful for this thesis. They performed the fitting of our SMR results in **Chapter 5 and 6**, where we study the interface between Pt/GGG and Pt/EuS, where GGG and EuS are a PMI and FMI, respectively.

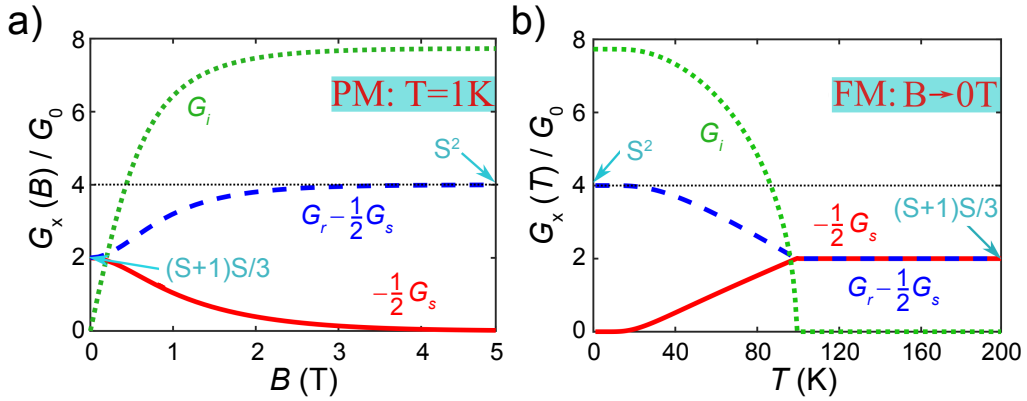

Figure 1.13: **Magnetic field dependence of the spin conductances for a paramagnetic material and temperature dependence for a ferromagnetic material.** Spin conductances G_x, with $x = r, i, s$ arranged in combinations of $-1/2G_s$, $G_r - 1/2G_s$ and G_i to describe the spin flips (magon generation), the spin dephasing (no spin transfer to MI) and exchange field at the interface, respectively. (a) Magnetic field dependence for PMI at $T = 1$ K. (b) Temperature dependence for a FMI with a Curie temperature of $T_c = 100$ K. Figure extracted from Ref. [84].

We have introduced the state of the art for the first part of this thesis, that covers **Chapters 3, 4, 5** and **6**. The second part of the thesis is also related to HM/MI interfaces but taking a look on what happens in the MI. As we explained above, G_s is related to the generation and absorption of magnons at the interface. These magnons (a collective precession of the magnetic moment carrying spin information) can diffuse through the MI and can be detected up to tens of microns. In the following section, we introduce how to excite/detect magnon currents.

1.5.6 Magnon-spin transport through magnetic insulators

In section 1.1.1, we have discussed how spin information can be transported through conduction electrons, i.e. a conduction-electron spin current [Fig. 1.14(a)]. This transport implies the diffusion of charges and some heat dissipation

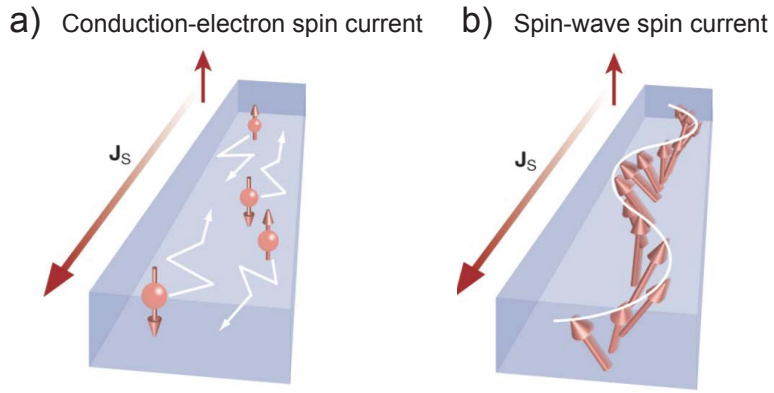

Figure 1.14: **Different types of spin currents.** Transport of spin information by (a) conduction-electron and (b) spin-wave spin currents. Figure adapted from Ref. [19].

is associated. Nonetheless, the transport of spin information through insulators with long-range magnetic order is also possible. The spin transport in FMI is possible thanks to the spin waves or magnons [Fig. 1.14(b)], without the ohmic losses associated to the electron conduction [19, 20]. Interestingly, it has been reported that these magnons may have longer diffusion length than the one of the conduction-electron spins for the best metals. Therefore, magnon-based spintronics offers a promising alternative for the transport of spin information for long distances.

The generation of magnon spin currents FMIs can be achieved by exciting the ferromagnetic resonance of the FMI [19, 85] (low frequency coherent magnons), by inducing thermal gradient [86] (high frequency incoherent magnons), or electrically by making use of the spin Hall effect (SHE) of heavy metals such as Pt [20] (high-frequency incoherent magnons), whereas the magnon currents can be detected ellectrically by employing the inverse spin Hall effect (ISHE). In the following section we focus on the electrically and thermally generated magnons as in Ref. [20].

Electrical excitation and detection

In 2015, L. J. Cornelissen *et al.* [20] demonstrated for the first time how to electrically excite and detect magnons into YIG, which is a ferrimagnetic insulator. The mechanism of creation of a magnon imbalance at the HM/FMI interface is governed by G_s, where a spin-flip of the conduction electron in the HM excites a magnon in the FMI. Reciprocally, a magnon accumulation in the FMI side will generate a spin accumulation due to magnon absorption (Fig. 1.15). In order to study the magnon transport through a FMI, it is necessary to employ a non-local configuration as shown in Fig. 1.16(a). This device scheme allows exploiting the

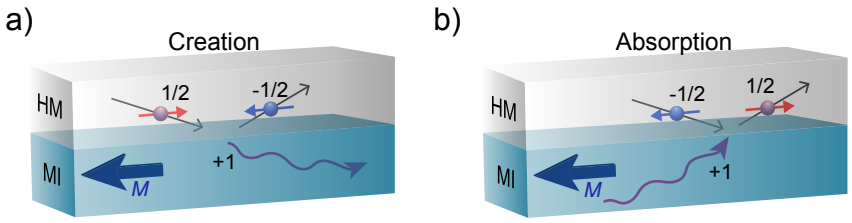

Figure 1.15: **Electrical creation of magnon imbalance.** How magnons are (a) created or (b) absorbed at the HM/MI interface, inducing a magnon imbalance. Figure adapted from Ref. [20].

large SHE in HMs [42, 87–89] to electrically excite and detect magnon currents in MI. By applying a charge current along a HM strip, a spin accumulation is induced at the HM side of the HM/FMI interface due to the SHE [which is in the plane of the film and perpendicular to the current, see vector notation in Fig. 1.16(a)]. When the FMI magnetization and spin polarization of the spin accumulation in HM are parallel (antiparallel), a magnon is annihilated (created) due to exchange interaction between the HM electron spins and the FMI magnetic moments, leading to a magnon imbalance that modifies the magnon chemical potential close to the interface [55]. This gives rise to a diffusion of magnons (magnon spin current) that can propagate for several microns along the FMI, for instance in YIG [20, 52, 56, 90–94]. By the reciprocal process, a second HM strip can detect the magnon imbalance, as the induced spin accumulation in HM (due to the magnon-to-spin conversion at the interface) is finally converted to a voltage by the ISHE.

As an example, we show in Fig. 1.17(a) the first harmonic response of the non-local voltage signal (normalized to the applied current) measured in a representative device at two different currents while rotating the in-plane magnetic field, performed by L. J. Cornelissen *et al.* in Pt/YIG non-local device [20]. Note that the angular dependence of the first harmonic non-local signal shows the expected sin^2 dependence, which is due to the symmetry of the SHE and the ISHE at the injector and detector Pt stripes, respectively, and their relative orientation with the magnetization of the YIG layer [20, 52, 53]. The non-local configuration and the electrical injection has been broadly used for magnon spin transport since the first report in 2015 [20, 52, 53, 55, 56, 86, 91–93, 95–98].

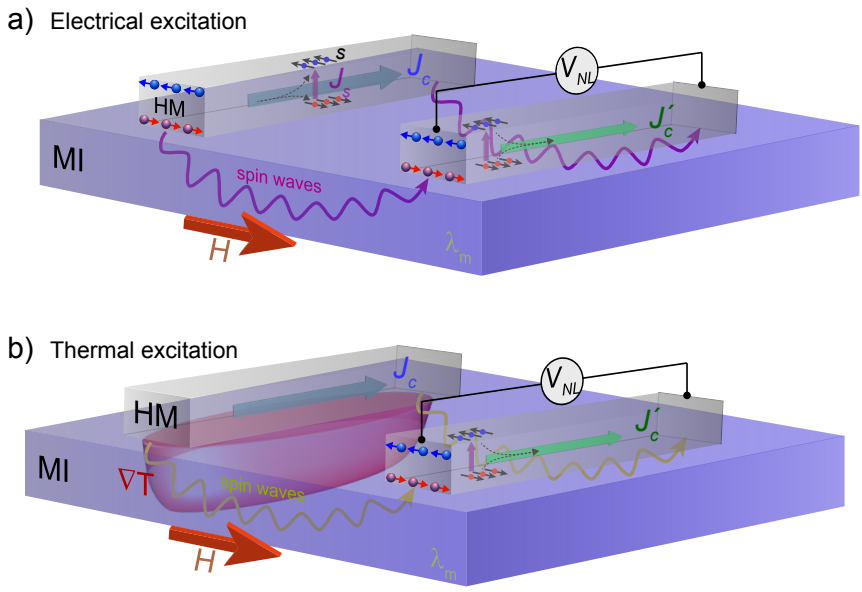

Figure 1.16: **Non-local magnon excitation and detection configuration.** How to excite magnons (a) electrically and (b) thermally, being detected both electrically. Figures adapted from Ref. [20].

Thermal excitation

On the other hand, magnons can also be thermally excited. In ferromagnetic materials, a thermal gradient drives a magnon spin current parallel to the induced heat flow due to the spin Seebeck effect [46], as explained in Section 1.5.3. Therefore, by making use of the Joule heating when driving charge current in the HM stripe, a thermal gradient can be generated in the FMI film beneath, resulting in a diffusive magnon current that can be non-locally detected by employing the ISHE of a second HM strip [Fig. 1.16(b)] [20, 86, 91, 96, 97, 99]. In this non-local spin Seebeck configuration, the second harmonic response of the voltage scales quadratically with the applied charge current. Figure 1.17(b) shows the angular dependence of the second harmonic non-local signal in Pt/YIG, showing a *sin* dependence with α, because in this case only the ISHE symmetry of the detector plays a role [20, 52].

Magnon diffusion length

In these type of non-local experiments the quality of the interface is important for the optimal excitation and detection of magnon currents flowing through the FMI. Nonetheless, the key parameter, which defines the transport of magnons, is the magnon diffusion length (λ_m). λ_m defines the characteristic length to which magnons can propagate. In order to extract λ_m, it is necessary to use the non-local configuration shown in Fig. 1.16(a) and Fig. 1.16(b), changing the distances between the injector and the detector. As an example, Figs. 1.17(c) and 1.17(d) show

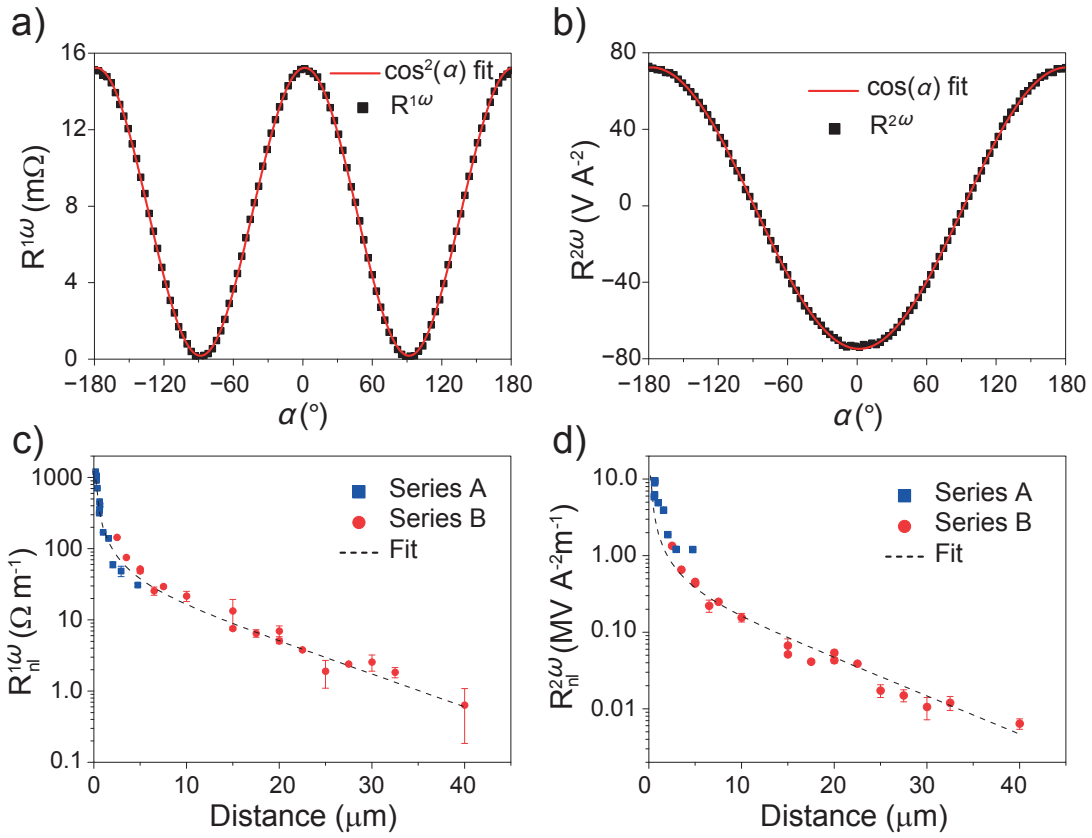

Figure 1.17: **Non-local magnon spin transport measurements.** Non-local ADMR measurements for (a) electrically and (b) thermally excited magnons. (c-d) Distance dependence of the non-local resistance for both excited magnons. The dashed line represent the fitting for extracting the magnon diffusion length. Figures adapted from Ref. [20].

the distance dependence of the non-local resistance for electrically and thermally excited magnons, respectively. The dashed line represents the fitting performed in order to extract λ_m, using the following equation:

$$R_{NL} = \frac{C}{\lambda_m} \frac{e^{d/\lambda_m}}{1 - e^{2d/\lambda_m}} \tag{1.36}$$

where R_{NL} is the non-local resistance detected by ISHE in the second HM stripe, d is the injector-detector distance and C is a constant that depends on the efficiency of magnon injection (governed by G_s). There are two different limits that defined the regimes shown in Fig. 1.17(d):

- For $d/\lambda_m << 1$:

$$R_{NL} \sim \frac{1}{d} \tag{1.37}$$

- For $d/\lambda_m > 1$:

$$R_{NL} \sim e^{-d/\lambda_m} \tag{1.38}$$

When the magnons are generated, they first diffuse and then relax, Eq. 1.37. It is during the relaxation process (also known as *exponential regime*, see Eq. 1.38) where λ_m plays the important role, defining up to which distance the magnon scan be detected. λ_m value has been studies in YIG as a function of the temperature [56, 90, 97], magnetic field [100], thermal gradient [86], and thickness [96]. An earlier report suggested that λ_m is the same regardless of the mechanism by which the magnons are excited (by thermal gradients or by electrical excitation) [56], but more recent works showed that those values might be different [90, 96]. It is thus not clear whether the thickness of the FMI layer might play a role on λ_m or the nature of the excited magnons, and thus their diffusivity, might be different due to the different energy scales involved in the two types of generation methods. In **Chapter 7**, we study the magnon spin transport in a $2-\mu$m$-$thick YIG. In addition, λ_m has been studied in other MI with long-range order such as AFM like $NiFe_2O_4$ [90] or $\alpha-Fe_2O_3$ [101].

1.6 This thesis

The results presented in this thesis are divided in two parts. The first part (**Chapters 4**, **5**, **6** and **7**) focuses on the study of spin Hall magnetoresistance in magnetic insulators with different magnetic order. In the second part (**Chapters 8** and **9**), we focus on the study of the spin transport properties through magnetic insulators *via* spin waves (magnons) in prototypical YIG.

- **Chapter 1** presents a general introduction to spintronics, important discoveries and applications. After that, we introduce the heavy metal and magnetic insulators systems and the spin-dependent phenomena occurring in these heterostructures.
- **Chapter 2** describes the experimental techniques used in this thesis to characterize the structure and transport properties of our heavy metal/magnetic insulator bilayers.

Part I. *Spin Hall Magnetoresistance in Magnetic Insulators*

- **Chapter 3**. We show the presence of the SMR in prototypical ferrimagnetic YIG and the confirmation of the effect by replacing the Pt with Au.

- **Chapter 4**. This chapter presents an insulating garnet bilayer, formed by YIG and GdIG. We perform SMR measurements, where we observe that both magnetic layers are antiferromagnetically coupled. Furthermore, we observe a memory effect at low temperatures that is detected by SMR.

- **Chapter 5**. We report the first study of SMR in a paramagnetic insulator GGG ($Gd_3Ga_5O_{12}$). We show the evolution of the *spin-mixing conductance* terms as a function of the magnetic field and its relation with the magnetization of the magnetic insulator, which fits very well with a newly developed microscopic theory for SMR.

- **Chapter 6**. We performed SMR measurements in a ferromagnetic insulator (EuS). We investigate the spin conductance terms, where usually the contribution of G_r is much larger than that of G_i. However, in this chapter, we report for the first time a HM/MI system that the *field-like* torque exerted to the magnetization is larger than the *spin-transfer* torque in ferromagnetic insulators.

Part II. *Magnon Spin Transport in Magnetic Insulators*

- **Chapter 7** shows the comparison between the transport of electrically and thermally excited magnons in a 2-μm-thick YIG film. We demonstrate the different transport characteristic lengths and behavior as function of the temperature and magnetic field and, thus, the different nature of the two types of magnons.

- **Chapter 8**. We study the long-distance spin information transport in materials without crystal structure, in this case amorphous YIG. However, we discuss that the measured non-local signals are caused due to leakage current through the insulator because of the resistivity drop with increasing temperature, and no evidence of magnon current is observed.

1

Chapter 2

Experimental techniques

In this chapter, we explain how we fabricated and characterized the devices used in this thesis; Hall bars for the spin Hall magnetoresistance experiments and non-local devices for the magnon spin transport measurements.

2.1 Fabrication techniques

All the devices have been fabricated in a clean room, where the number and size of particles per cubic meter is controlled. These devices have two techniques in common, electron-beam lithography (eBL) for defining the structures and metallic deposition *via* sputtering. Figure 2.1 shows the different steps we followed to fabricate our samples and two different paths to perform the nanofabrication: (i) by using a negative resist and subsequent etching (etching procedure), and (ii) by using positive resist and subsequent lift-off (lift-off procedure). The different steps are described as follows:

- **Etching procedure** [Fig.2.1(a)]. After cleaning the substrate, the steps one the following: (i) material deposition by sputtering or evaporation; (ii) spin coating of the negative resist; (iii) eBL process to design the structure; (iv) developing: during the developing with negative resist all the resist that has not been exposed is removed; (v) Ar^+-ion miller to remove the material not covered by the resist, and, finally, (vi) the sample is placed in the resist remover. This procedure is mainly used to design the Pt nanostructures for magnon spin transport and Pt Hall bars for spin Hall magnetoresistance (SMR).

- **Lift-off procedure** [Fig.2.1(b)]. This process was mainly used to make large contact pads for the nanostructures: (i) spin coating the positive resist;

(ii) eBL process to pattern the contacts; (iii) developing, in the case of positive resist, during the developing the areas which has been exposed are the ones that are removed; (iv) Material deposition, for contacts we use electron-beam evaporation of Ti as a buffer layer and then thermal evaporation of Au; (v) the lift-off to remove the resist and the material on top of the resist, by immersing the sample in acetone. We used the "lift-off procedure" for the first HM/MI samples in this thesis, however, we realized that the interface was not as reproducible as we would like. Therefore, we change to the "etching procedure" in order to ensure the quality of the interface and, thus, the interface reproducibility. This process is useful for our samples because we realized that the interface quality between the Pt and the MI is much better compared to the one using positive resist that usually leaves some waste from the resist after the developing.

In this thesis, we fabricated two different type of devices: Hall bars and magnon transport devices. On the one hand, the Hall bar devices were used to perform the spin Hall magnetoresistance measurements in the magnetic insulator/heavy metal interfaces that we present in **Chapters 3**, **4**, **5** and **6**. For these devices, we only used the fabrication method depicted in Fig. 2.1(a). For specific details of the samples, each chapter describes the recipe of the fabrication. On the other hand,

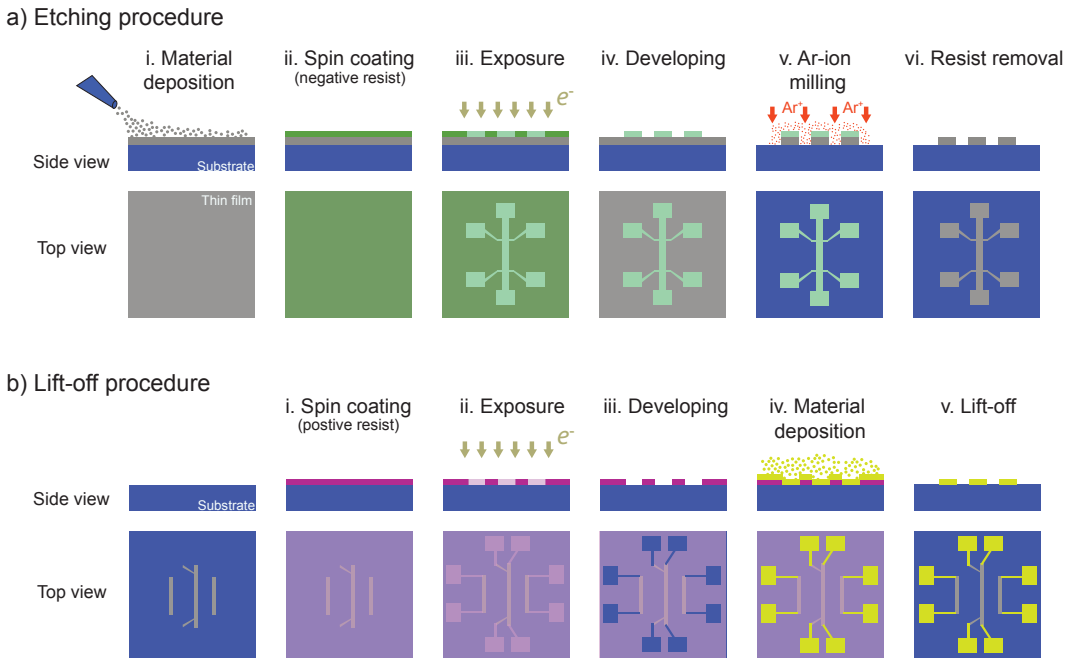

Figure 2.1: **Nanofabrication methods.** (a) Etching procedure with negative resist, and (b) lift-off procedure with positive resist. Each procedure is based on several steps that are sketched and named.

the magnon transport devices in **Chapters 7** and **8** were fabricated by using the "etching procedure" for the Pt nanostructures (the Pt injector and non-local detector strips), and the "lift-off procedure" for the larger Ti/Au contact pads.

In the following sections, we explain in detail the techniques used for fabricating and characterizing our different samples.

2.1.1 Cleaning process

In this thesis we used several substrates: $Y_3Fe_5O_{12}$ (YIG), $Gd_3Ga_5O_{12}$ (GGG), SiO_2 and amorphous $Y_3Fe_5O_{12}$ (a-YIG) and, in all cases we used the same cleaning process. First of all, we performed a sonication in acetone for 5 minutes. After that, we repeat the process, but with the substrate immerse in isopropanol (IPA) instead of acetone. Later, we immerse the substrate in water and dry it first with a N_2 gun and then in a hot plate for 5 minutes at 140^oC to remove all the liquid water.

2.1.2 Magnetron sputtering

Magnetron sputtering deposition is a technique that consists in bombarding a material with ions of an inert gas to remove material from the target and deposit it in a substrate. Figure 2.2 schematically shows how sputter deposition works and the different parts of a magnetron sputtering system. In our case, we used Ar as a inert gas. Because of the voltage applied between the anode (sample holder, top part of the chamber) and cathode (magnetron, bottom part), there are electrons flowing in the chamber and hitting the Ar atoms, ionizing them (Ar^+). The Ar^+ are attracted by the cathode creating a plasma close to the magnetron, where a magnetic field is used to increase the plasma density. These Ar^+ ions strongly strike and blast loose the material target, generating a vapor of the material in the chamber that is deposited in the substrate and, by rotating the sample holder, we can get an uniform thin film. By using this technique, we deposited our Pt thin films on top of the magnetic insulators substrates, in an ultra-high vacuum (UHV) Magnetron Sputtering system by *AJA* that contains seven material targets.

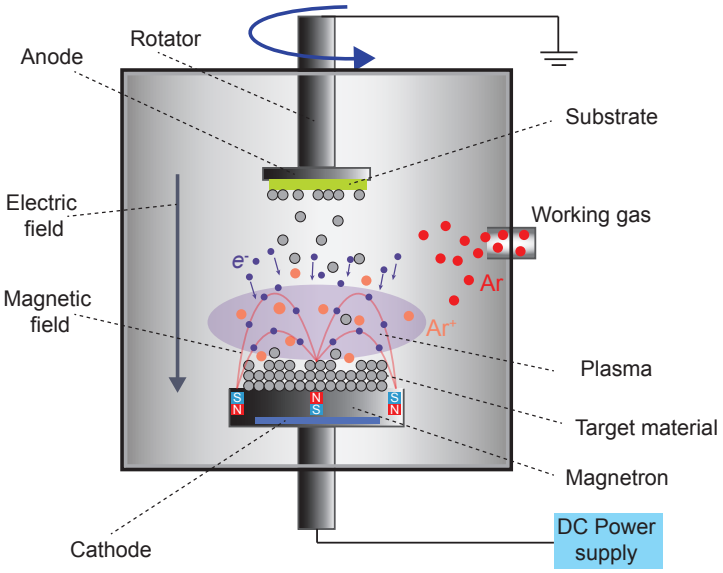

Figure 2.2: **Schematic illustration of magnetron sputtering.** (a) The rotator with the sample holder is located at the top part of the chamber, which works as the anode to apply the bias voltage. The magnetron where the material target is placed is located at the bottom part. The blue circles represent the electrons (e^-) accelerated from the anode to the cathode. The red circles represent the inert gas (Ar) and the orange ones are the ionized Ar (Ar^+) after crashing with the electrons. These Ar^+ ions strike and blast loose the material target. Figure adapted from Ref. [102].

2.1.3 Electron-beam and thermal evaporation

Furthermore, we used electron-beam (e-beam) and thermal evaporation to deposit thin layers, both evaporation were performed in a high vacuum evaporator system by *Kurt J. Lesker*. A schematic e-beam evaporator is shown in Fig. 2.3(a). For this e-beam evaporation a filament is needed, usually a W filament. A high current is applied in the W filament in order to emit electrons with high energies by thermoionic emission that are focused to the target or reservoir material by magnets. The electron current heats up the material up to the melting point of the metal. This creates a vapor of the material that is deposited on the substrate. This technique is powerful to evaporate metals with high melting point in a low pressure conditions, $10^{-5} - 10^{-6}$ Torr. In our case, we used to evaporate the buffer layer of Ti in order to deposit *in situ* Au contacts on top. We deposited the Au contacts by thermal evaporation, see Fig. 2.3(b). This technique consist on melting the material by heating the crucible with an electrical current by Joule effect. This current is applied around the crucible as it is shown in the sketch of Fig. 2.3(b).

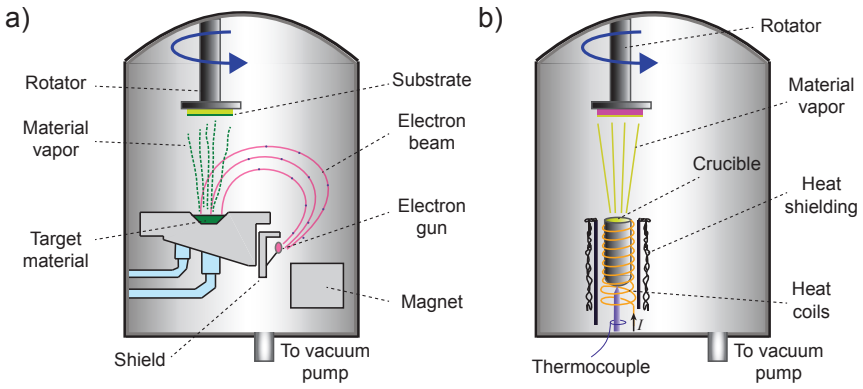

Figure 2.3: **Schematic illustration of electron-beam and thermal evaporation.** Sketch of (a) an electron beam evaporator and (b) a thermal evaporator, where the different parts are shown. Figures adapted from Refs. [103, 104].

2.1.4 Electron-beam lithography and photolithography

For our devices, we need to define nanostructures. Electron-beam lithography (eBL) is a very convenient way to define structures with very good definition. The eBL system consists of a vacuum column of mirrors that focus and accelerate the electrons, and expose an area controlling the charge density. The electrons are focused directly to an XY stage, controlled by a piezolectric micromanipulator, where the substrate is placed. By moving the stage in the XY−plane, we can define our structure with a resolution down to $\sim$ 10 nm. In our case, we have access to two different eBL systems: *Raith 150-TWO* and *Raith e-Line*.

The working principle of the eBL is related to the crosslinking of the polymer used as resists when they are exposed to the impact of energetic electrons [105]. There are two groups of resists, positive and negative. The group is defined depending if the resist becomes sensitive or insensitive, after the interaction with the electrons, to the specific chemistry solvents that allow them to be selectively dissolved or developed. When the electrons penetrate into the resist, they break crosslinkers of the polymeric chain. Then, after the exposure of the resist, the sample is submerged in a developing solvent that removes the polymer that was or was not exposed. If the resist is negative (positive), the resist that was not exposed is removed (kept) by the developer. This means that, depending on the structure to design and the materials in the sample, it is more convenient to use one or the other resist. In the particular case of this thesis, we mainly used negative resist. This is because we performed our experiments at the interface of the MI/HM heterostructures and to ensure the best quality of the interface, we deposited the Pt layer right after cleaning the sample. After patterning our nanostructure by eBL, we remove the Pt outside the pattern by Ar-ion milling (as we explain in the next section). However, we also used positive resist for

patterning the Ti/Au contacts using the lift-off procedure defined in Fig. 2.1(b).

Some of the samples used in this thesis were made also by photolithography, where the working principle is similar to the eBL, but ultraviolet (UV) light instead of electrons is used. In this case, when the sample is being illuminated, a mask on top of the substrate is used to define the structure needed.

2.1.5 Ar-ion milling

Ar-ion milling is a technique that was broadly used in this thesis to remove Pt when we define our nanostructure to ensure the interface quality. This process was also used before evaporating the Ti/Au contacts for cleaning the resist that could remain after developing the positive resist.

Ar-ion milling (*a.k.a.* ion beam etching) is a purely physical process used for etching away material and cleaning surfaces. The technique consists in bombarding the material that we want to remove with Ar ions perpendicular to the surface. In order to do that, the Ar ions are created with a plasma source and accelerated in a special grid, creating an ion beam that impacts the surface of the material with high energy, removing material from the sample. In this thesis we used an Ar-ion miller equipment from *4wave*.

2.2 Characterization techniques

In this section, we introduce different characterization methods used in this thesis to study the electrical, magnetic and structural properties of our samples.

2.2.1 Transport measurements

Electrical measurements under a magnetic field and a thermal bath were carried out in a Physical Property Measurement System developed by *Quantum Design*, see Fig. 2.4. In order to measure our sample, we stick the sample to a sample holder, also known as *puck*, which has 8 electrical contacts for the transport measurements. Depending on the measurement configuration for applying the magnetic field we have two different pucks: Fig. 2.4(a) shows a *normal puck*, this configuration allows to apply the magnetic field in the out-of-plane of the sample, as well as perform measurements by changing the plane of the magnetic field from out-of-plane configuration to in-plane configuration, thanks to the rotator (Fig. 2.4(c)). In the case of the second puck, known as *T-puck* (Fig. 2.4(c)), this puck is useful for rotating the magnetic field in the plane of the sample. The

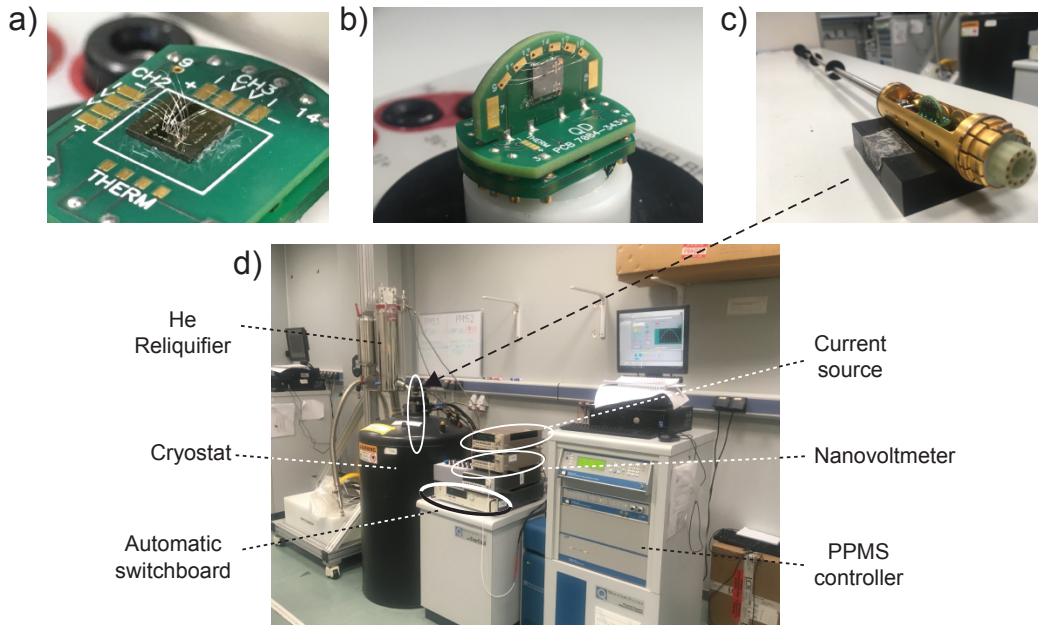

Figure 2.4: **Physical Property Measurement System and sample holders.** (a)-(b) Sample holders of the PPMS for electrical measurements with 8 contacts, known as puck. On the one hand, (a) normal puck, used to apply the magnetic field out-of-plane and, which allows to sweep the magnetic field from in-plane to out-of -plane configuration. On the other hand, (b) T-puck, this puck is useful to apply the magnetic field in-plane configuration. (c) Rotator where the puck is placed to be introduced into cryostat. (d) The Physical Properties Measurement System (PPMS) and its different components.

combination of both pucks allows us to perform measurements while rotating the direction of H in three different rotation planes. We use a *wire bonder* system developed by *West Bond* to electrically contact the puck with the sample by using Al wires (SiO_2 coated). The *wire bonder* is useful for our nanodevices because we can make contacts in very small pads (down to 200 μm x 200 μm), which allows us to include more nanodevices in the same chip. Once the sample is on the puck and contacted, we place it in the PPMS rotator, see Fig. 2.4(c), and insert the rotator into the the liquid-He cryostat, see Fig. 2.4(d). Inside the cryostat, we can control the temperature between 2 K and 400 K and apply a magnetic field up to 9 T by the PPMS controller.

Moreover, in order to perform the electrical measurements we have connected an automatic switchboard to choose the contacts for applying the charge current and measuring the voltage. For that purpose, we have a current source *Keithley 6221* and a nanovoltmeter *Keithley 2182A*. Therefore, we apply a *dc* charge current and measure the voltage drop in different contacts depending on the type and configuration of the measurements. In the case of the SMR measurements, we measure the voltage locally 4-probes method, which means the voltage is mea-

sured in the same wire where the current is applied. The measurements are realized by using a "*dc* reversal" technique, also known as *delta mode*. This method allows to remove thermoelectric effect and reduce the noise, being suitable for low-resistance measurements. Delta mode consists of injecting alternated positive and negative currents and measuring the voltage each time that the polarity of the current change

$$V = \frac{V(+I) - V(-I)}{2} \tag{2.1}$$

where $V(+I)$ and $V(-I)$ are the local voltage for the positive and negative charge current polarity, respectively. This method is used for the local measurements in SMR experiments as well as for the electrical detection of magnons in magnon transport experiment, because delta mode is equivalent to measure the 1^{st} harmonic signal when using an *ac* measurement. However, in the non-local experiment for thermal magnon we the current is reversed as well and the non-local voltage is the sum instead of the difference:

$$V_{NL}^{th} = \frac{V_{NL}(+I) + V_{NL}(-I)}{2} \tag{2.2}$$

In the SMR measurement, we measure the voltage and divided by the applied current, getting the measured resistance. And we normalized the resistance for extracting $\Delta\rho_L/\rho$ and $\Delta\rho_T/\rho$ by:

$$\Delta\rho_L/\rho = [R(H(0^o)) - R(H(90^o))]/R(H(90^o)), \tag{2.3}$$
$$\Delta\rho_T/\rho = (L/w)[(R(H(45^o)) - R(H(135^o)))/\rho], \tag{2.4}$$

where L and w are the length and the width of the Hall bar, and ρ is the resistivity of the HM thin film.

In Figure 2.5 we show the measurement configurations used in this thesis. Figures 2.5(a-c) show the angular-dependent magnetoresistance (ADMR) configurations for the three main sweeping angles; (a) $\gamma-$plane where H is swept in the plane of the charge current, (b) $\beta-$plane where H is swept in the plane perpendicular to the charge current, and (c) $\alpha-$plane where H is swept in the plane of the sample. For the field-dependent magnetoresistance (FDMR) case, we use the configuration shown in Fig. 2.5(d), sweeping the magnetic field along the three main axes of the sample (x,y,z). Figure 2.5(e) shows the Hall configuration measurement, where H is swept in out-of-plane while measuring the transverse voltage.

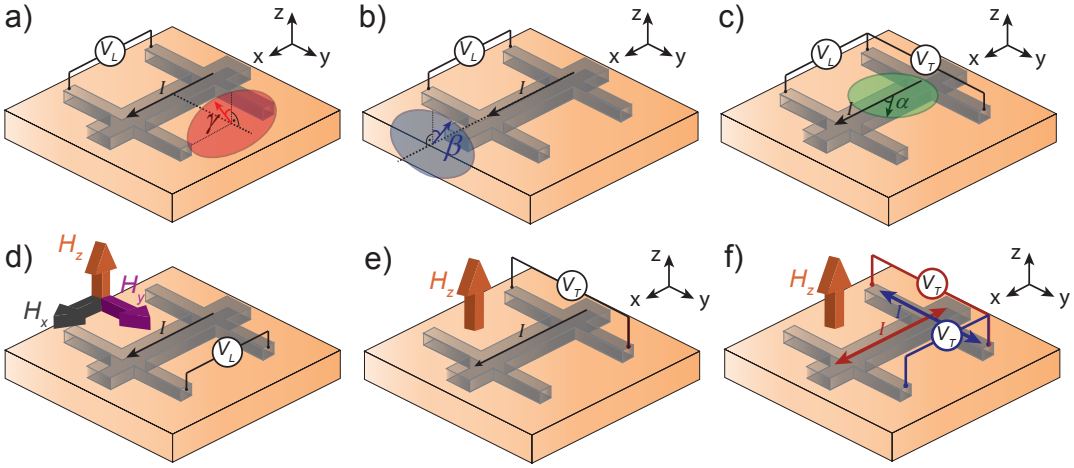

Figure 2.5: **Magnetoresistance measurement configurations.** (a)-(c) Angular dependence magnetoresistance configuration for γ, β and $\alpha-$planes, respectively. (d) Field dependence magnetoresistance configuration, where the magnetic field is swept in the main three axes (x, y, z). (e) Hall configuration method. (f) Zero-offset-Hall configuration method.

Finally, Fig. 2.5(f) represents the zero-offset-Hall configuration. This technique is really useful to measure the transverse magnetoresistance when the amplitude of the signal is really small and much larger contribution background contributions can mask the signal. The charge current is applied alternate in different contacts (blue and red arrows in Fig. 2.5(f)) while measuring the transverse voltage, as it shown in Fig. 2.5(f).

2.2.2 Magnetometry techniques

For the magnetic measurements, we use different techniques; in the case of **Chapter 4** we used x-ray magnetic dichroism because it allows us to select the energy of a specific magnetic atom you want to characterize. For **Chapters 5** and **6**, we used the superconducting quantum interference device (SQUID) technique, whereas in **Chapter 8** we performed vibrating sample magnetometry (VSM) technique.

VSM and SQUID

VSM and SQUID are used to characterize the magnetic properties of materials as a function of magnetic field, temperature and time. To study the behavior of the magnetization M of the substrates as a function of the temperature T, we perform field cooled (FC) and zero field cooled (ZFC) measurements. Before each measurement and before cooling down the sample, it is demagnetized by an

alternate magnetic field H. For the FC measurement, the sample is cooled down under the presence of a strong H. Then, at low T, the H is reduced, performing the M measurement while increasing T.

However, for the case of the ZFC, the sample is cooled down without any magnetic field applied, and then M is measured while T increases. Moreover, to study the magnetism at any particular temperature, we performed hysteresis loops, where M is measured as a function of H. The VSM measurements where performed in a liquid-He crysotat in PPMS by *Quantum Design* with a T between 2 and 300 K and with an external field up to 9 T, with a magnetic moment resolution of $10^{-5}-10^{-6}$ emu. SQUID measurements were performed in a *Quantum design SQUID-VSM*, in which the range of T is 2−400 K, with magnetic fields up to 7 T and a magnetic moment resolution of 10^{-8} emu.

X-ray magnetic circular dichroism

X-ray magnetic circular dichroism (XMCD) is a technique that allows to extract information of the magnetization associated with each atomic species. First of all, it is necessary to measure the x-ray absorption spectrum (XAS) for circular polarized x-ray light. In order to measure the spectrum is necessary to apply light circular polarized to the right (C^+) and to the left (C^-). When the light is polarized to the right (left) one of the spin population increases (decreases), then, $(C^+ + C^-)/2$ gives the XAS spectrum, whereas the difference between both spectrum with C^+ and C^- defines the XMCD spectrum, having XMCD spectrum as a function of the energy can be extracted. Then, by fixing the energy and measuring its variation with and external magnetic field we are able to measure the hysteresis loop at different temperatures. These experiments were perfomed by J. López-López and Dr. S. Blanco-Canosa at the BL29-BOREAS beamline [106] of the ALBA Syncrothron Light Source facilities, using surface-sensitive total electron yield (TEY) detection.

2.2.3 Electron microscopy

Scanning Electron Microscopy

We use the scanning electron microscopy (SEM) to check the morphology of our samples, which means to check the dimensions (lengths and widths) of the devices with nanometric resolution. SEM is a microscopy technique that is based on focusing high energy electrons to the sample and scan the sample point by point measuring the secondary electrons or backscattered electrons from the sample. These electrons are coming from the interaction of the incident electrons with the surface of the sample, giving rise to high resolution images on the topography

and composition of the sample. The SEM used in this thesis in the same one of the eBL systems, *Raith 150-TWO* and *Raith e-Line*.

Transmission Electron Microscopy and Scanning Transmission Electron Microscopy

Transmission electron microscopy (TEM)/ scanning transmission electron microscopy (STEM) is a technique to identify the crystallographic phase and the composition of our films. In this case, the electrons that formed the image cross through the sample, that is why the samples need to be thin and are usually a thin section or lamella. The TEM images of this thesis were performed by Prof. A. Chuvilin on a Titan 60-300 electron microscope (FEI Co., The Netherlands) equipped with EDAX detector (Ametek Inc., USA), high angular annular dark field (HAADF)-STEM detector and imaging Cs corrector. The composition profiles were acquired by STEM mode utilizing energy dispersive X-ray spectroscopy (EDX) signal.

2.2.4 X-ray diffraction and X-ray reflectivity

X-ray reflectivity (XRR) measurements have been used to extract the thickness of the films. We mainly used this technique to calculate the deposition rates of the metals in order to have the control of the thickness in our films. X-ray diffraction (XRD) has been used to characterize the crystallinity of the samples. Both measurements were performed in a *X'Pert PRO* by *PANalytical*. The X-ray tube of this system has a wavelength $\lambda = 0.154$ nm that corresponds to CuK_α radiation, as the anode of the X-ray generator is made of Cu.

As crystals consists of regularly space atoms, the interaction of the incident x-rays with the crystal gices to scattered x-rays. Depending on the optical path of the x-rays into the thin film, the reflected rays will interfere constructively or destructively. The spatial variation of the intensity forms a diffraction pattern that contains information of the crystallographic structure of the material, Fig. 2.6. Bragg's law describes the condition for constructive interference:

$$n\lambda = 2dsin(\theta) \tag{2.5}$$

where n is the interference order, λ is the wavelength of the incident wave, d is the distance between the atomic planes and θ is the scattering angle respect to the surface plane, Fig. 2.6.

In the XRR case, the x-ray incident beam angle and detection angle have the

same grazing incidence value during the scan. The interference is generated at the top and the bottom surface of the film, giving rise to the Kiessig fringes in the measured intensity. From the periodicity of the fringes we can can calculate the thickness of the material [107].

In the case of the XRD, the angle θ is swept to higher angles getting the intensity of the reflected x-ray. The reflection of the incident x-rays will vary depending on the atom distances in the crystalline structure, Fig.2.6(b). By sweeping the detection angle, we can get the diffraction spectrum that can be compared to a database to identify the crystallographic phases present in the sample [108].

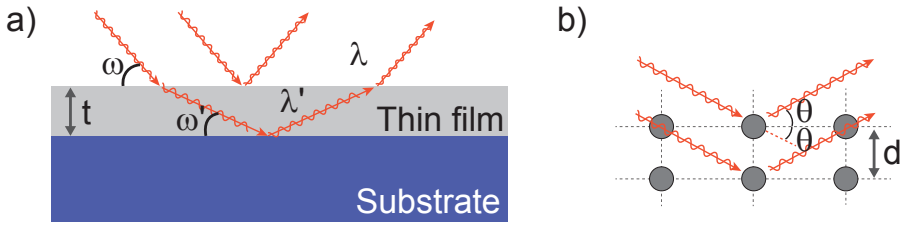

Figure 2.6: **X-ray diffractometer working principle.** (a) X-ray reflectivity configuration method, where ω is the incident angle of the X-rays, λ and λ' are the wavelengths in air and in the film respectively, and t is the film thickness. (b) Schematic illustration of X-ray scattering in crystalline samples.

Results. Part I

Spin Hall Magnetoresistance in Magnetic Insulators

2

Chapter 3

Spin Hall magnetoresistance in Au thin films on $Y_3Fe_5O_{12}$

Magnetoresistance signals in platinum in contact with magnetic insulators are common observations that could be explained by either proximity magnetization or spin Hall magnetoresistance. In this chapter, longitudinal and transverse magnetoresistances are measured in a pure gold thin film on the ferrimagnetic insulator YIG. We show that both the longitudinal and transverse magnetoresistances have quantitatively consistent scaling in YIG/Au and in a YIG/Pt reference system when applying the Spin Hall magnetoresistance framework. No contribution of an anomalous Hall effect due to the magnetic proximity effect is evident. This work was done in collaboration with Prof. Denys Makarov and Dr. Tobias Kosub from *Helmholtz-Zentrum Dresden Rossendorf (HZDR).*[*]

[*] Published as: Tobias Kosub, Saül Vélez, Juan M. Gomez-Perez, Luis E. Hueso, Jürgen Fassbender, Fèlix Casanova and Denys Makarov,"Anomalous Hall-like transverse magnetoresistance in Au thin films on $Y_3Fe_5O_{12}$", *Appl. Phys. Lett.* **113**, 222409 (2018)

3

3.1 Introduction

In section 1.5.1, we introduced the importance of the interface in HM/FM heterostructures and the role of the real part (G_r) and imaginary part (G_i) of the spin-mixing conductance ($G_{\uparrow\downarrow}$). In the case of YIG, it is known that G_r is at least one order of magnitude larger than G_i [48, 79, 82]. To extract both G_r and G_i is necessary to obtained both SMR amplitudes, one should measure the longitudinal (ρ_L) and transverse (ρ_T) resistivity, as described in Eq. 1.23 and Eq. 1.24. In the particular case of $G_r >> G_i$ [48, 79, 82] then we can combine Eqs. 1.26 and 1.27 to obtain the ratio between G_r and G_i,

$$\frac{G_r}{G_i} \approx -\frac{\Delta\rho_1}{\Delta\rho_2}\frac{1}{1+2\rho_0\lambda G_r coth(\frac{d_N}{\lambda})}. \tag{3.1}$$

Although SMR has been well established, in most cased Pt has been used as the HM, because of its strong SOC and large θ_{SH}. However, Pt is close to Stoner criterion for ferromagnetism and can thus show a strong magnetic proximity effect [68]. For this reason, Pt could become ferromagnetic in contact with a magnetic material showing a clear anomalous Hall effect (AHE) that would mirror the magnetization of a nearby magnetic insulator [67,69–71]. SMR theory predicts an anomalous Hall-like component in the ρ_T that scales with θ_{SH}^2 instead of the usual AHE that scale just with θ_{SH}. This means that, in the case that Pt presents an AHE-like signal in ρ_T, an ambiguity about its origin (SMR or MPE) appears in the Pt/FMI system.

In this chapter we present SMR measurements in Au/YIG and compare to a Pt/YIG reference. Au shares the excellent electrical properties of Pt and, at the same time, static proximity magnetization is not expected for Au [109].Therefore, we are excluding the possible influence of MPE and its associated AHE.

3.2 Experimental details

We prepared Au (10 nm)/YIG and Pt (2 nm)/YIG bilayers. In both cases the metal layers were deposited by using DC sputtering with a power of 60 W (Au) and 80 W (Pt), in an Ar atmosphere of 3 mTorr. After the thin film deposition, a Hall bar (width 100 μm, length 800 μm) was patterned by negative e-beam lithography and Ar-ion milling for removing the material following the same procedure described in section 2.1.

The longitudinal ADMR and Hall measurements were performed as it was described in section 2.2.1.

3.3 Results and discussion

First of all, we measured the ADMR for the Pt/YIG sample rotating the magnetic field ($H = 1$ T to saturate the YIG magnetization) in the three main angles (defined in 3.1(a)). The ADMR reveals the behavior expected for SMR, Fig. 3.1(c), a sin^2 modulation appears in $\alpha-$ and $\beta-$planes and no modulation in $\gamma-$plane. From the ADMR measurements in Pt/YIG, we can get the base resistivity $\rho_0 = 51.6$ $\mu\Omega$·cm in our Pt film and, based on empirical relationships

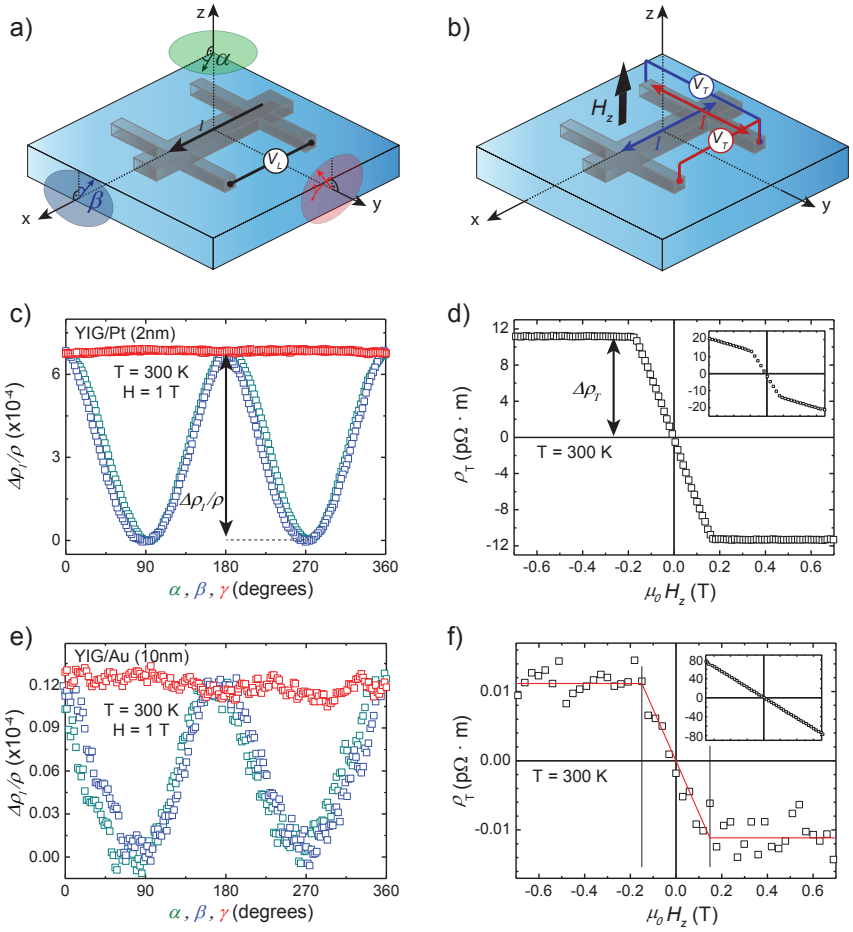

Figure 3.1: **Device geometries and spin Hall magnetoresistance measurements.** Magnetoresistance measurements geometries: (a) longitudinal resistivity measurement geometry with the magnetic field applied along the three relevant H-rotation planes; α (green), β (blue) and γ (red). (b) Transverse resistivity measurement geometry with the magnetic field applied out-of-plane. Panels (c) and (e) show the longitudinal ADMR measurements at room temperature and $H = 1$ T for Pt/YIG and Au/YIG, respectively. Panels (d) and (f) show the Zero-Offset Hall measurements after subtracting the normal Hall effect for Pt/YIG and Au/YIG, respectively. Grey lines in (f) indicates the saturation field of the YIG and the red line is a data fit. The insets show the data before the subtraction of the Hall effect.

Table 3.1: **Overview of the obtained quantities for Pt/YIG and Au/YIG.** In this table are presented the experimental parameters for the Pt/YIG and Au/YIG: resistivity ρ_0, the relative longitudinal and transverse amplitudes of the spin Hall magnetoresistance $\Delta\rho_L$ and $\Delta\rho_T$, spin diffusion length λ, spin Hall angle θ, and real and imaginary part of the spin mixing conductivities G_r and G_i. *Spin-mixing conductances are calculated for Pt/YIG and assumed to be identical for Au/YIG.

	Pt (2 nm)	Au (10 nm)
ρ_0 ($\mu\Omega$·cm)	51.6	8.4
$\Delta\rho_1/\rho$	6.8×10^{-4}	1.3×10^{-5}
$\Delta\rho_2/\rho$	2.2×10^{-5}	1.3×10^{-7}
λ (nm)	1.2 ± 0.2	25^{+12}_{-8}
θ	0.18 ± 0.02	$0.017^{+0.016}_{-0.008}$
$G_r(10^{14}\Omega^{-1}\mathrm{m}^{-2})$	0.95 ± 0.25	0.95^*
G_r/G_i	22 ± 3	22^*

found in Ref. [42] we obtain the values $\lambda_{Pt} = (1.2 \pm 0.2)$ nm and $\theta_{SH,Pt} = 0.09 \pm 0.01$. We extract $\Delta\rho_1/\rho$ from the fitting of the AMDR to the sin^2 in Fig. 3.1(c); for the Pt case $\Delta\rho_1/\rho = 6.8 \times 10^{-4}$. Now, with all these parameters and taking into account that $G_r >> G_i$ we can calculate G_r by Eq. 1.26, $G_r = (3.8 \pm 1.0) \times 10^{14}\ \Omega^{-1}\mathrm{m}^{-2}$. This value is in good agreement with previous reports in the same Pt/YIG bilayers [9,11,13,15,18,19]. In order to calculate the ratio G_r/G_i, we need to measure $\Delta\rho_2$, then we sweep the magnetic field out-of-plane while measuring the transverse resistance, see Fig. 3.1(b) for the measurement configuration. Figure 3.1(d) shows the transverse resistivity with the magnetic field applied out-of-plane, we can see that the YIG is saturated for $|H| > 0.2$ T. From Fig. 3.1(b) we can extract $\Delta\rho_2/\rho = 2.2 \times 10^{-5}$ and, by using Eq. 3.1, the ratio $G_r/G_i = 22 \pm 3$ in Pt/YIG sample (Table 3.1). This ratio is also in good agreement with the theoretical calculation $G_r/G_i \approx 20$ [48], as well as experimental values of $G_r/G_i \approx 16 \pm 4$ [82] and $G_r/G_i \approx 33$ [79].

The experimental values $\Delta\rho_{1,Au}/\rho = 1.3 \times 10^{-5}$ and $\Delta\rho_{2,Au}/\rho = 1.3 \times 10^{-7}$ of Au/YIG are obtained in the same manner as for the Pt/YIG reference sample [see Fig. 3.1(e) and Fig. 3.1(f)]. To actually measure a transverse magnetoresistance at this really samll signal (Fig. 3.1(f)), special care must be taken to isolate the AHE-like signal from the much larger backgrounds contributions, which we accomplish by eliminating the longitudinal resistance by Zero-Offset Hall measurements, as it was explained in section 2.2.1.

In the following, we will provide an independent calculation of the SMR mag-

nitudes for Au/YIG. First of all, we have to estimate λ_{Au} and $\theta_{SH,Au}$. For the case of λ_{Au} is well established that the spin relaxation in metals is dominated by the Elliott-Yafet mechanism ($\lambda \propto \rho^{-1}$), then based on our Au resistivity ($\rho_0 = 8.4\mu\Omega$m) and empirical data [110–118]. Figure 3.2(a) illustrates how we obtained $\lambda_{Au} \sim 25$ nm. Regarding $\theta_{SH,Au}$, different mechanisms have been suggested to contribute in Au [111, 114, 115], but the origin of the SHE is not well established yet. In our case, for simplicity, we consider that the intrinsic contribution dominates the spin Hall effect in Au. Therefore, $\theta_{SH,Au} = \sigma_{SH}^{int} \times \rho$ holds, and the intrinsic spin Hall conductivity σ_{SH}^{int} depends on the band structure and is thus constant for a given material. In the case of Au, the values reported are $\sigma_{SH}^{int} = (2.0^{+2.0}_{-1.0}) \left[\frac{\hbar}{2e}\right] 10^5\ \Omega^{-1}\text{m}^{-1}$ [111–115, 117–119]. The fitted σ_{SH}^{int} value leads to a $\theta_{SH,Au} = 0.017^{+0.016}_{-0.008}$ for our films as shown in Fig. 3.2(b).

Furthermore, we assume identical interface spin-mixing conductances in our reference Pt system and the Au systems $G_{Pt/YIG} \equiv G_{Au/YIG}$, owing to the identical fabrication conditions, similar chemical qualities of the metals and similar Fermi energies, and Sharvin conductivities of the metals [65]. With all the Au parameters extracted, we estimate the SMR amplitudes $\Delta\rho_1/\rho = 0.21^{+3.2}_{-0.4} \times 10^{-5}$ and $\Delta\rho_2/\rho = 0.21^{+3.8}_{-0.2} \times 10^{-7}$. The calculated values are quantitatively consistent with the measured values, from Fig. 3.1(e) and 3.1(f) we get $\Delta\rho_1/\rho = 1.3 \times 10^{-5}$ and $\Delta\rho_2/\rho = 1.7 \times 10^{-7}$, respectively (Table 3.1).

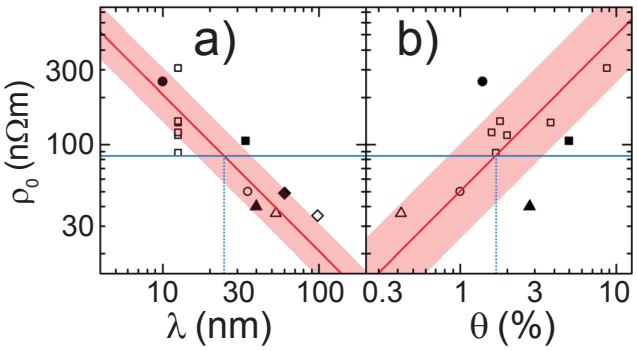

Figure 3.2: **Spin diffusion length and spin Hall angle for Au.** Reported λ and θ_{SH} for Au thin films as a function of the film resistivities ρ_0 and fits in context of the Elliot-Yafet relation (a) and resistivity dependence on the intrinsic spin Hall effect (b) shown as red lines. The data points are empirical data taken from Kimura *et al.* [110] (solid diamond), Brangham *et al.* [111] (hollow squares), Vlaminck *et al.* and Obstbaum *et al.* [112,113] (hollow circle), Isasa *et al.* [114] (hollow triangle), Niimi *et al.* [115] (solid triangle), Mosendz *et al.* and Obstbaum *et al.* [116,119] (solid square), Laczkowski *et al.* [117] (hollow diamond) and Qu *et al.* [118] (solid circle). θ_{SH} values from Refs. [114, 115] have been multiplied by 2 for a proper comparison. The solid blue line denotes the resistivity of the Au film in the present YIG/Au system; dashed blue lines show the obtained spintronic quantities λ and θ_{SH} for our Au film.

We conclude that the observed magnitudes of the longitudinal and transverse magnetoresistances in both studied systems, Au/YIG and Pt/YIG, are consistent with the same physical picture. Therefore, the AHE-like signal that appears in HM/FMI systems can be fully understood only by spin Hall magnetoresistance due to the imaginary part of the spin-mixing conductance, without any signal of the presence of magnetic proximity effect.

This chapter is a good introduction for **Chapters 4, 5** and **6**. In the case of **Chapter 4**, we will study an ultrathin YIG, demonstrating that SMR is a powerful tool for studying the evolution of the surface magnetization thanks to the relation between G_r and the magnetization of the FMI. In the case of **Chapters 5** and **6**, we will perform an exhaustive study in the evolution of G_r, G_i and G_s in a paramagnetic and ferromagnetic insulator, respectively.

Chapter 4

Spin Hall magnetoresistance in ultrathin YIG: Synthetic antiferromagnetic coupling between ultrathin insulating garnets

In this chapter, we present a ultra-thin yttrium iron garnet (YIG) / gadolinium iron garnet (GdIG) insulating bilayer on gadolinium gallium garnet (GGG). From spin Hall magnetoresistance (SMR) and X-ray magnetic circular dichroism measurements, we show that the YIG and the GdIG layers magnetically couple antiparallel even in moderate in-plane magnetic fields. The results demonstrate an all-insulating equivalent of a synthetic antiferromagnet in a garnet-based thin film heterostructure and could open new venues for insulators in magnetic devices. As an example, we demonstrate a memory element with orthogonal magnetization switching that can be read by SMR. This work was performed in collaboration with the group of Prof. Jason W. A. Robinson from Cambridge University, who grew the ultra-thin substrates.*

*Published as: Juan M. Gomez-Perez, Saül Vélez, Lauren McKenzie-Sell, Mario Amado, Javier Herrero-Martin, Josu López-López, S. Blanco-Canosa, Luis E. Hueso, Andrey Chuvilin, Jason W. A. Robinson and Fèlix Casanova,"Synthetic Antiferromagnetic Coupling Between Ultrathin Insulating Garnets",*Phys. Rev. Appl.* **10**, 044046 (2018).

4.1 Introduction

Downscaling is an important factor for spintronics devices and so maintaining magnetic properties of the FMI at reduced dimensions is considered key for deterministic magnetization reversal due to spin-orbit torque [120, 121], or for guiding magnons [122]. Since a top-down approach to nanofabrication requires the use of thin film materials, there is much effort focused on obtaining high quality YIG thin films. Standard growth techniques such as liquid phase epitaxy (LPE) are being pushed towards the 100 nm thickness [123], but sub-100-nm-thick films still require alternative techniques such as pulsed laser deposition (PLD) [124–126] or magnetron sputtering [127–130]. However, material quality in these cases is not as consistently high as seen in LPE-based YIG. For example, recent works report unusual magnetic anisotropy related to Fe^{+3} vacancies in PLD-grown YIG [124, 125], and either exceptionally high magnetization [130] or a magnetization suppression [129] in sputtered films that could be related to the interface between YIG and the used substrate $Gd_3Ga_5O_{12}$ (GGG). The variety in the results and interpretations than can be found in the literature calls for an in-depth characterization of those thin YIG films.

In this chapter, we show a ultra-thin (13 nm thick) epitaxial YIG on GGG. The structural and compositional analysis by transmission electron microscopy (TEM)/scanning TEM (STEM) reveal a well-defined GdIG interlayer at the YIG/GGG interface. The magnetic properties of the top YIG layer, characterized by SMR and X-ray magnetic circular dichroism (XMCD) measurements, are dramatically modified with the YIG magnetization pinned antiparallel to the GdIG one. The results demonstrate the presence of a negative exchange interaction between YIG and GdIG that constitutes a novel insulating synthetic antiferromagnetic state, with a potential use in insulating spintronic devices [131]. For instance, we show that the complex interplay between the negative exchange interaction and the demagnetizing fields of the layers induce a memory effect that could be exploited as as a device.

4.2 Experimental details

The epitaxial YIG films (13 nm thick) are grown on (111) oriented GGG by pulse laser deposition (PLD) in an ultra-high vacuum chamber with a base pressure of better that 5×10^{-7} mbar. Prior to film growth, the GGG is rinsed with deionised water, acetone and isopropyl alcohol and annealed *ex situ* in a constant flow of O_2 at 1000^oC for 8 hours. The YIG films is deposited using KrF excimer laser (248 nm wavelength) with a nominal energy of 450 mJ and fluence of 2.2 W/cm^2. The films are grown under a stable atmosphere of 0.12 mbar of O_2

at 750oC and fixed frequency of 4 Hz for 20 minutes. An *in-situ* postannealling at 850^{o}C is performed for 2 hours in 0.5 mbar partial pressure of static O_2 and subsequently cooled down to room temperature at a rate of -5^o/min. The growth process and the quality characterization were performed by Prof. Jason W. A. Robinson's group. Once we have the film, a 5-nm-thick Pt layer was magnetron-sputtered *ex situ* (80 W; 3 mtorr of Ar atmosphere) and a Hall bar (width 450 nm, length 80 μm) was patterned by negative e-beam lithography and Ar-ion milling. For the TEM/STEM and XMCD measurements, unpatterned samples were capped with 2-nm-thick layer of sputtered Pt.

TEM/STEM was performed on a Titan 60-300 electron microscope (FEI Co., The Netherlands) equipped with EDAX detector (Ametek Inc., USA), high angular annular dark field (HAADF)-STEM detector and imaging Cs corrector. High resolution TEM (HR-TEM) images were obtained at 300 kV at negative Cs imaging conditions [132] so that atoms look bright. Composition profiles were acquired in STEM mode with drift correction utilizing energy dispersive X-ray spectroscopy (EDX) signal. Geometrical Phase Analysis (GPA) was performed on HR-TEM images using all strong reflections for noise suppression [133]. Magnetotransport measurements were performed as explained in section 2.2.1. XMCD measurements were performed across the Fe-$L_{2,3}$ absorption edges at the BL29-BOREAS beamline [106] of the ALBA Synchrotron Light Source (Barcelona, Spain), using surface-sensitive total electron yield (TEY) detection.

4.3 Results and discussion

4.3.1 Structural characterization

Figure 4.1 shows the structural analysis of a Pt/YIG film by TEM/STEM. Figure 4.1(a) shows a HR-TEM cross-sectional micrograph where the top layer corresponds to Pt (polycrystalline), with epitaxial YIG on the single crystal GGG beneath. The YIG/GGG interface reveals an extended region with visually different contrast. Comparison of high-resolution contrast in the YIG, interfacial and GGG regions [averaged unit cells are shown in the insets in Fig. 4.1(a)] show that within the same crystallographic structure there is a variation in distribution of heavy atoms from region to region. To confirm the nature of this middle region, we performed EDX analysis of a spatial distribution of the elements along the out-of-plane direction [see Fig. 4.1(b), the scan line is indicated in Fig. 4.1(a)]. From this analysis, we confirm that our film consists of 2-nm-thick Pt on the top surface, followed by 12-nm-thick YIG layer that is Ga-doped. The interface between Pt and YIG is assumed to be atomically sharp, thus the inclination of Y curve and declination of Pt curve give the estimation of spatial resolution of

composition measurement, which is of the order of 1 nm. At the depth of 12 nm, Y concentration decreases to zero, though the slope of declination is lower that at the upper interface, indicating a smooth change of concentration in this case. Gd concentration in the same region increases complementarily to Y. At the same time the decrease of Fe concentration is delayed by $\sim$ 3 nm relative to Y, and Ga concentration changes complementarily to Fe. Thus, it may be concluded that, starting from a depth of 12 nm, Gd gradually (within a range of $\sim$ 2 nm) substitutes Y in the lattice; similarly, Ga substitutes Fe but with $\sim$ 3 nm delay in depth. This delay results in the formation of a 2.8-nm-thick interlayer with a nominal composition corresponding to gadolinium iron garnet (GdIG). By making an analytical deconvolution of concentration profiles (Fig. 4.1(b)) at the interface we can extract the real thickness of pure GdGIG layer, which is 2.2 nm.

Further insight into the nature of the layer can be obtained from the analysis of the interplanar distances in the direction normal to the surface. This is done by generalized GPA on the base of HR-TEM images [133]. Variations of the interplanar distance are calculated in term of strain with respect to the GGG lattice. The obtained strain profile is presented as a black line in Fig. 4.1(b) and shows that the region corresponding to GdIG composition is expanded by 1.1% with respect to GGG. This is lower that the 2.3% theoretically expected in epitaxial GdIG on GGG [134], which could be explained by the presence of an inter-diffusion layer between GGG and GdIG that reduces the strain compared

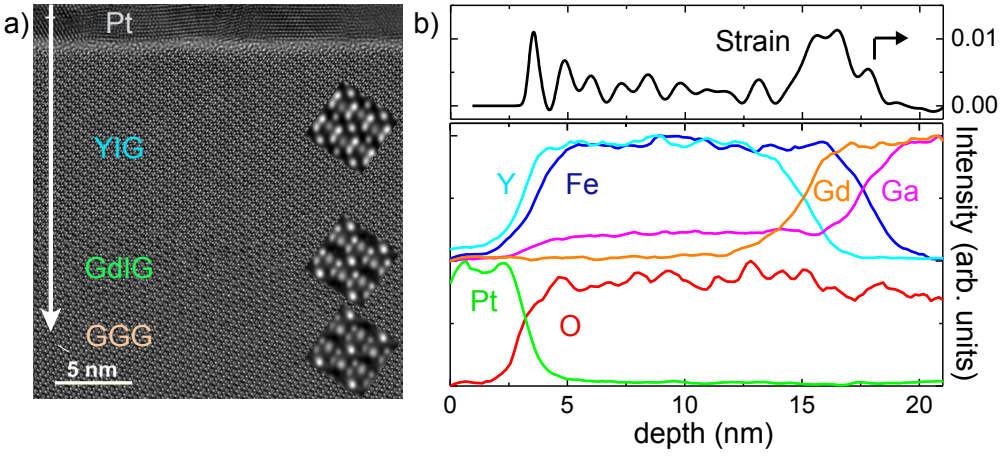

Figure 4.1: **Transmission electron microscope image of YIG/GdIG bilayer.** (a) High resolution TEM micrograph Pt (2 nm)/YIG (13 nm) (thicknesses are nominal) on GGG (111). Inset: averaged unit cells obtained in the different regions shown corresponding to YIG, GdIG, and GGG from the top to bottom. (b) Spatial distribution of the elements extracted along the white arrow in (a) by spatially resolved EDX. The strain, extracted from the HR TEM image as a variation of the interplanar distance with respect to the GGG lattice, is also plotted as a black line. A strain of +0.01 means a lattice expansion by 1% in the out-of-plane direction.

to a sharp interface. The YIG layer shows an unexpected 0.2% expansion of the lattice (on average) with respect to GGG, in spite of the very similar lattice constant [134]. This detailed analysis confirms that we have a magnetic garnet bilayer. The presence of a Gd-doped YIG interlayer in YIG/GGG films after similar postannealing treatments has been recently reported [128,129], but in our case we can confirm a well-defined, 2.2-nm-thick GdIG layer, and the fact that the YIG layer is Ga-doped.

4.3.2 Spin Hall magnetoresistance

The ultra-thin garnet bilayer could only be measured by standard magnetometry and ferromagnetic resonance at room temperature and with significant averaging, due to the weak moment compared to the paramagnetic substrate and small magnetic volume. At lower temperatures, both signal are reduce beyond detection. A convenient alternative for magnetic characterization is the use of SMR, which is surface sensitive and does not depend on the magnetic volume. Therefore, we performed longitudinal SMR measurements, which only probe the top surface magnetization [53, 76, 135] (the penetration depth of the conduction electrons into YIG is $\sim 3{-}4$ Å [48]) and thus the magnetization of the GdIG intelayer is not expected to influence the SMR signal [129]. As shown in Eq. 1.23, SMR depends on the relative angle of the surface magnetization in the FMI and the spin accumulation in the HM. When the spin accumulation and the magnetization are parallel (perpendicular) the longitudinal resistance state is low (high). The patterned Hall bar on the YIG corresponds to a Pt/YIG structure widely measured before [52–54,66,80,82], as it was done in previous chapter (Fig. 3.1(c)). Figure 4.2 shows the longitudinal resistance R_L from a $4-$point configuration at 2 K (a), 30 K (b), 100 K (c) and 300 K (d) as a function of the external magnetic field H applied along the three main axes of the sample [see Fig. 4.2(a)]. These FDMR curves are expected to shown the features of SMR: i) a low resistance when the magnetic fields saturates the magnetization in the $y-$direction (i.e., parallel to the the spin-Hall-induced spin accumulation in Pt) with a peak at low H corresponding to the magnetization reversal of the YIG film; ii) a high resistance value when H saturates the magnetization in the $x-$ or $z-$direction (i.e., perpendicular to the spin accumulation in Pt) with a dip at low magnetization due the magnetization reversal. However, the FDMR curves are very different from the ones observed so far in YIG [53, 54, 66, 82]. A high $H \sim 8$ T is needed to saturate the magnetization of the film even at low temperatures [see FDMR curves along $y-$direction in Fig. 4.2(a) at 2 K], while YIG is expected to saturate within a few mT in plane [54]. These results already suggest that the top surface magnetization of the 12-nm-thick YIG is strongly influenced by the 2.2-nm-thick GdIG at the bottom. Moreover, at relatively low H (below ~ 1.5 T) and at low

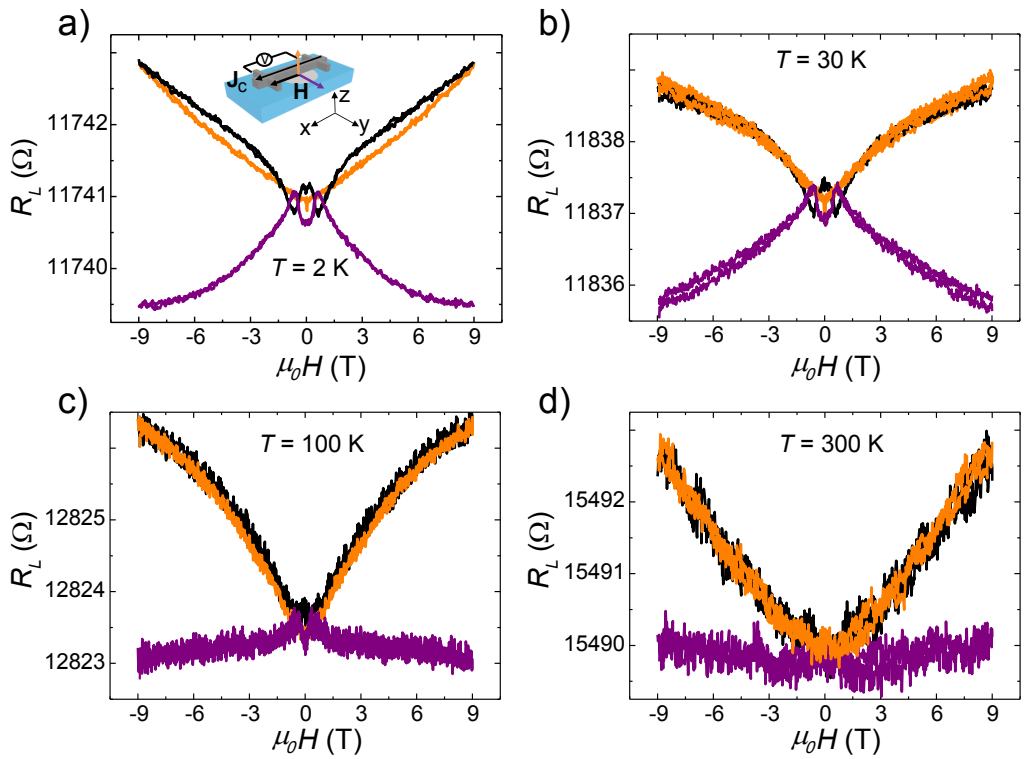

Figure 4.2: **Longitudinal field dependent magnetoresistance at high magnetic fields.** Longitudinal FDMR measurements at (a) 2 K, (b) 30 K, (c) 100 K and (d) 300 K along the three main axes with a step size of 18 mT. Sketch indicates the definition of the axes, color code of the magnetic field direction, and the measurement configuration.

temperatures (below $\sim$ 100 K) the FDMR curves along the three main axes show unexpected crossings, indicating complex magnetic behavior with the magnetization being non-collinear with the applied H [see the zoom of Fig. 4.2(a) in Fig. 4.3] The unexpected crossing shown by the FDMR curves along the three main axes remain up to 100 K, see Figs. 4.2(c) and 4.2(d). Above this temeprature, no signature of SMR is observed. Instead, the FDMR curves are similar to the ones reported with Pt on top of non-magnetic materials such a SiO_2, Pyrex or sapphire, characteristic of Hanle magnetoresistance [54].

To understand better the magnetic properties and to confirm the non-collinear magnetization behavior of the bilayer, we performed ADMR measurements in $\alpha-$, $\beta-$ and $\gamma-$planes (see sketches in Fig. 4.4) at 2 K.The ADMR curves have three distinct behaviors depending on the applied H [zones 1-3 indicated in Fig. 4.3]. At high H [above $\sim$ 1.5 T, zone 3, Fig. 4.4(c)], we have a cos^2 dependence with the angle for $\alpha-$ and $\beta-$planes, and no modulation for the $\gamma-$plane, which is the expected dependence for SMR [53, 65, 75, 76, 135] when the magnetization is saturated and collinear with H. The same angular dependence is expected for

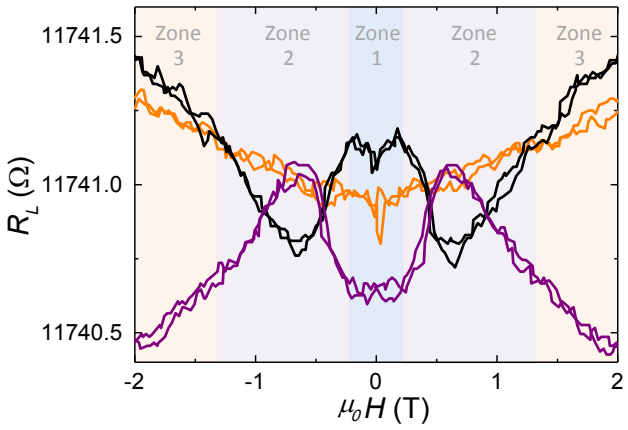

Figure 4.3: **Longitudinal field dependent magnetoresistance at low magnetic field.** Zoom of the FDMR curves in figure 4.2 at low magnetic fields with a step size of 18 mT. Three different zones associated with the magnetization behavior are indicated.

HMR [53], which has a common origin with the SMR and is only relevant at very large fields. The absence of modulation in $\gamma-$plane rules out the presence of MPE in our Pt layer [66] in agreement wit the results in **Chapter 3**. At low H [below $\sim$ 0.25 T, zone 1, Fig. 4.4(a)] we still have the cos^2 dependence in $\alpha-$plane, but the amplitude is smaller because the bilayer is not saturated (as evidenced in Fig. 4.2(a)). However, we have an unusual ADMR for the $\beta-$ and $\gamma-$planes. In the $\beta-$plane, the ADMR curve does not follow a cos^2 dependence, indicating that the magnetization and H are not collinear. When H is perfectly out-of-plane ($\beta = 0^o$ and 180^o) the magnetization also points out-of-plane. As soon as H rotates away from the out-of-plane into the y-direction, the magnetization switches abruptly to the in-plane y-direction ($\beta = 90^o$ and 270^o). This effect cannot be simply explained by the demagnetization field due to strong shape anisotropy expected in the ultra-thin film [81,136]. As we will see below, the presence of the GdIG layer also plays a role in this behavior. Accordingly, the same abrupt switching from the out-of-plane ($\gamma = 0^o$ and 180^o) into the in-plane x-direction ($\gamma = 90^o$ and 270^o) when rotating H along $\gamma-$plane should not give any ADMR modulation; however, the dip in ADMR at $\gamma = 0^o$ and 180^o shows that a small net contribution of the magnetization along y exit, probably because the YIG film breaks into domains.

At intermediate magnetic field (0.25 T $\leq H \leq$ 1.5 T, zone 2, Fig. 4.4(b)), we can see that the ADMR curve for $\alpha-$plane maintains the cos^2 dependence, but with a phase shift α_0 (which can be either $\sim 112^o$ or $\sim 68^o$ for the example at $H =$ 0.5 T shown here). This α_0 should correspond to the angle between H and the surface magnetization. This is confirmed by an extra modulation in the ADMR curves for the $\beta-$ and $\gamma-$plane. Two broad peaks appear, with a maximum in the $\beta-$scan when the magnetization is in-plane ($\beta = 90^o$ and 270^o) and a minimum

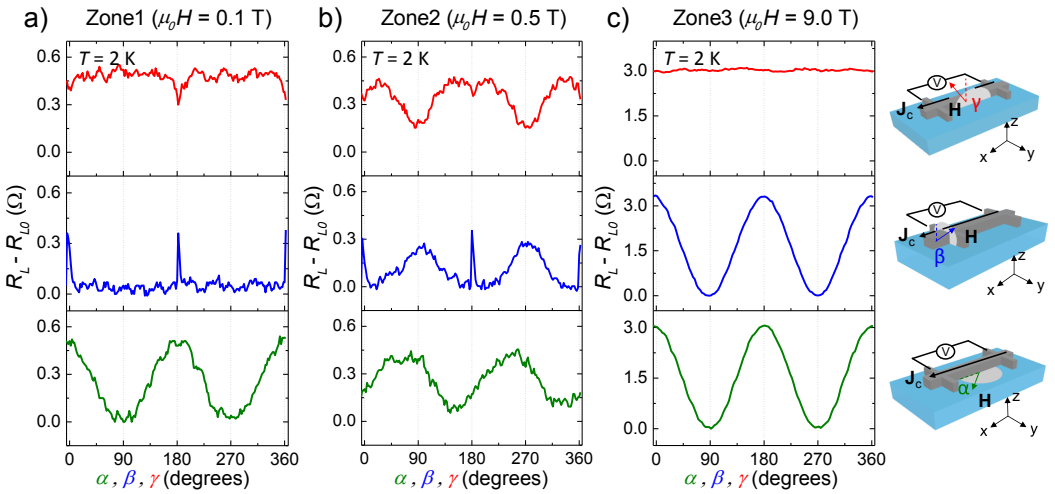

Figure 4.4: **Longitudinal angular dependence magnetoresistance measurements.** Longitudinal ADMR measurements at 2 K along the three relevant H-rotation planes (α, β, γ) for different applied magnetic fields: (a) 0.1 T (zone 1), (b) 0.5 T (zone 2), and (c) 9 T (zone 3). A different background R_{L0} is subtracted for the ADMR curves at each field. Sketches indicate the definition of the angles, the axes, and the measurement configuration. Dotted line at each sketch corresponds to 0^o.

in the $\gamma-$scan when the magnetization is in-plane ($\gamma = 90^o$ and 270^o). This result is equivalent to the observed behavior in the $\alpha-$plane (note that the magnetic field direction at $\beta = 90^o$ in the $\beta-$scan is the same as $\alpha = 90^o$ in the $\alpha-$scan and the magnetic field direction at $\gamma = 90^o$ is the same as $\alpha = 0^o$, see sketches in Fig. 4.4). When the phase shift for the $\alpha-$scan occurs in zone 2, the ADMR value at $\alpha = 90^o$ increases and the value at $\alpha = 0^o$ decreases. This very same effect shows up in the $\beta-$scan with a relative maximum (ADMR value increases) developing at $\beta = 90^o$ and in the $\gamma-$scan with a relative minimum (ADMR value decreases) developing at $\gamma = 90^o$.

To study with more detail the behavior of α_0, we performed ADMR measurements in the $\alpha-$plane for different applied magnetic fields (from 20 mT to 2 T). Figure 4.5(a) shows how the phase of the ADMR curves shift with increasing H. Figure 4.5(b) plots α_0 as a function of H, showing a monotonic change between 0^o and 180^o. Although we cannot, in principle, determine if the phase shift at low fields corresponds to 0^o or 180^o, we assume that α_0 goes from 180^o at low fields to 0^o at high fields because it is physically more plausible. The three different zones already described can be distinguished in this plot: (i) zone 1, where the surface magnetization is antiparallel to the applied H; (ii) zone 2, where the surface magnetization has certain angle with H; (iii) zone 3, where the surface magnetization is almost aligned with H. Note that with the SMR symmetry, we cannot determine whether the rotation occurs clockwise (angle between surface magnetization and H equal to α_0, as assumed in Fig. 4.5(b)) or counter clockwise

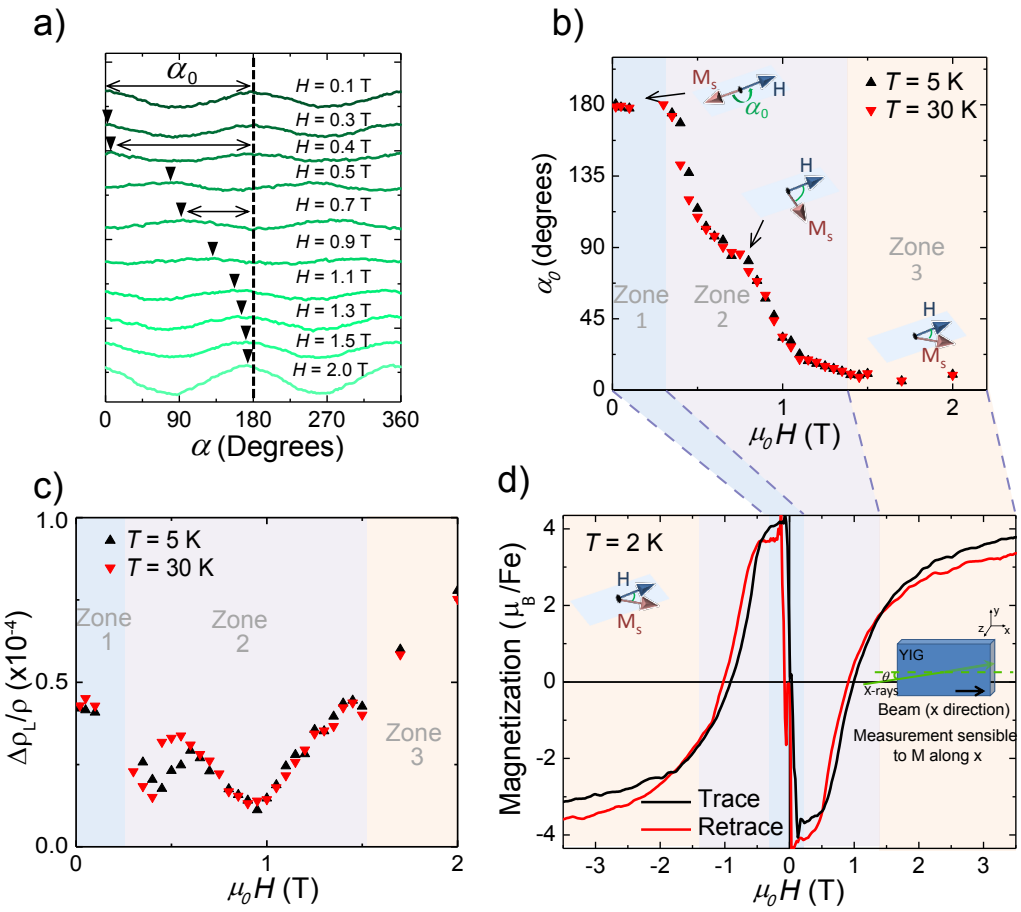

Figure 4.5: **Magnetization evolution with the applied magnetic field.** (a) Longitudinal ADMR measurements for different applied magnetic fields in the α–plane at 5 K. (b) Phase shift (α_0) as a function of magnetic field taken from data in (a). α_0 corresponds to the effective angle between the magnetization vector and the applied magnetic field. (c) Amplitude of the longitudinal SMR as function of H. (d) Hysteresis loop measured by XMCD with the magnetic field applied in-plane at 2 K. Small sketch represents the XMCD measurement configuration.

(angle between surface magnetization and H equal to $360^o - \alpha_0$)

We plot in Fig. 4.5(c) the SMR amplitude taken from the ADMR measurements at 5 K and 30 K in the a-plane (the same curves used to extract α_0) as a function of magnetic field. The SMR amplitude at zero field and all along zone 1 (where $\alpha_0 \sim 180^o$) is constant. When further increasing the magnetic field into zone 2, we observe two clear dips in the amplitude (at 0.45 and 0.95 T), which correspond to $\alpha_0 \sim 135^o$ and $\sim 45^o$. The amplitude at zone 1 is recovered at $\sim$ 1.5 T, when the surface magnetization rotation is almost complete ($\alpha_0 \to 0^o$). The further increase of the amplitude at higher fields (zone 3) is due to a combination of HMR and a non-saturating behavior [see Fig. 4.2(a) of the main text].

The decrease in the amplitude at two particular angles when the surface magnetization rotates towards the magnetic field direction could be explained by the fact that the surface magnetization vector tilts slightly out of plane in order to achieve more stability in the helical configuration formed in the YIG film (see following section). The decrease in the amplitude could also be explained if the locking angle α_0 has certain distribution. This could originate by a rough interface between GdIG and YIG, so that the helical configuration is slightly different along the plane.

4.3.3 X-ray magnetic circular dichroism measurement

To confirm this unconventional behavior that suggests that the surface magnetization of YIG opposes a low external field and only aligns parallel under a high enough field (>1.5 T), we performed XMCD, a technique that extracts information of the magnetization associated with each atomic species. The sample is oriented with its surface forming a grazing angle with respect to the propagation direction of incident x-rays (in-plane configuration), H is applied parallel to the x-ray beam and TEY detection is used, which is sensitive to the surface (up to 2−3 nm depth) [137], see Fig. 4.5(c) for measurement configuration method. We obtained the typical XMCD spectrum for standard YIG at Fe $L_{2,3}$ absorption edges (see section 4.5.1). From these data and applying the sum rules for XMCD spectra at different H values, we can estimate the magnetization per Fe ion and plot the hysteresis loop [see Fig. 4.5(d)]. The loop clearly confirms our scenario: a negative net magnetization is measured at low applied H, i.e., the magnetization vector of the YIG surface is aligned antiparallel to H. The net magnetization is reduced with increasing H because the magnetization vector starts rotating monotonously towards the applied H and, at certain value of H, becomes perpendicular to H, leading to not net magnetization. At high H, the net magnetization becomes positive while the magnetization vector approaches a collinear configuration with H, finally saturating at very high fields. Note that the saturation magnetization (3−3.5 μ_B/Fe) is lower than expected in YIG (5 μ_B/Fe), which can be explained by the presence of Ga substituting Fe along our YIG film [138]. With a particular configuration of the XMCD measurements that is sensitive to the magnetization perpendicular to the applied field [see Fig. 4.6(a)] we can clarify whether the surface magnetization is rotating counter-clockwise or clockwise when increasing the magnetic field. As sketched in Fig. 4.6(b), when the applied magnetic field increases above 0.2 T [field at which the magnetization starts to rotate, according to our results in Fig. 4.5(d)], we should start to detect a signal which will be positive (negative), indicating that the net magnetization is rotating counter-clockwise (clockwise). Figure 4.6(c) shows the experimental data measured in this configuration. The signal is small (i.e., large error bars) and the

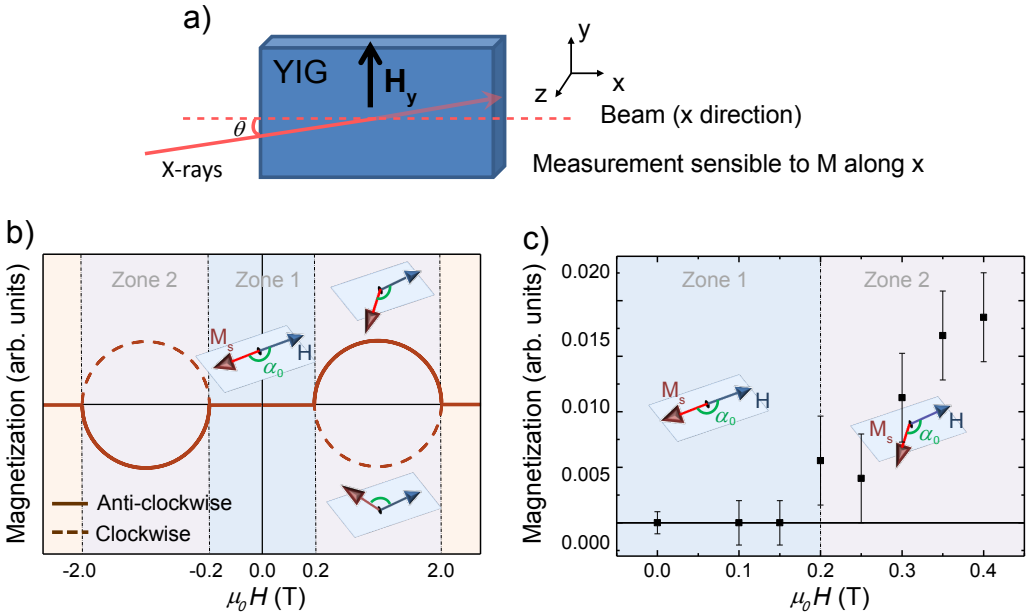

Figure 4.6: **Polarity of the surface magnetization with the external magnetic field.** (a) Experimental setup in the XMCD measurements used to obtain the polarity of the surface magnetization when locked at a certain angle with the external magnetic field. (b) Schematic plot of the perpendicular component of the in-plane magnetization as a function of the in-plane magnetic field. Two cases are shown: the magnetization rotates counter-clockwise (solid line) or clockwise (dotted line) when it is reoriented from an antiparallel to a parallel configuration in zone 2. (c) Experimental XMCD data of the perpendicular component of the in-plane magnetization as a function of the in-plane magnetic field measured at 2 K using the setup of panel (a).

maximum magnetic field is limited to 0.4 T because of the setup constrictions. Nevertheless, we can clearly see that the perpendicular magnetization is zero up to $\sim$ 0.2 T and starts to increase to positive values for larger magnetic fields, directly proving that the surface magnetization is rotating counter clockwise (for further discussion on the preference in the rotation direction, see section 4.5.2).

The behavior of the surface magnetization of YIG observed both via SMR and XMCD can be explained if we consider that YIG is in fact coupled antiparallel to the GdIG interlayer. A hysteresis loop similar to the one in Fig. 4.5(d) has been recently observed in Ni/Gd layers and attributed to the negative exchange coupling between the transition metal and rare-earth ferromagnets [139]. YIG has two magnetic sublattices [3 tetrahedrally coordinated ("FeD") and 2 octahedrally coordinated ("FeA") Fe^{3+} ions per formula unit] which are antiferromagnetically coupled ($J_{ad} \sim 32$ cm^{-1}) [140], leading to its ferrimagnetism, with the magnetization dominated by the FeD sublattice. GdIG has the same iron garnet crystal structure, with a third magnetic sublattice (3 dodecahedrally coordinated Gd^{3+} ions per formula unit), which is ferromagnetically coupled to the FeA sublat-

tice ($J_{ad} \sim 1.75$ cm^{-1}) and antiferromagnetically coupled to the FeD ($J_{cd} \sim 7$ cm^{-1}) [140]. The strong variation of the magnetization of the Gd sublattice with temperature makes GdIG a compensated ferrimagnet, with the magnetization dominated by the Gd and FeA sublattices below room temperature [98, 141, 142]. We hypothesize that the perfect epitaxy of the crystal structure at the YIG/GdIG interface (see sketch in Fig. 4.1(a)) would favor the continuity of the FeA and FeD sublattices across the interface (Fig. 4.7). Such continuity leads to an antiferromagnetic coupling between the net magnetization of the GdIG (dominated by Gd) and the net magnetization of the YIG (dominated by FeD), see Fig. 4.1, which should have the energy of ($J_{cd} \sim 0.14$ meV). This very same coupling has been deduced from recent magnetooptical spectroscopy [128] and polarized neutron reflectivity [129] experiments in YIG/GGG interfaces. In our case, the Gd magnetization at low T is so high that a 2.2-nm-thick GdIG layer can pin the whole 12-nm-thick YIG layer antiparallel to H.

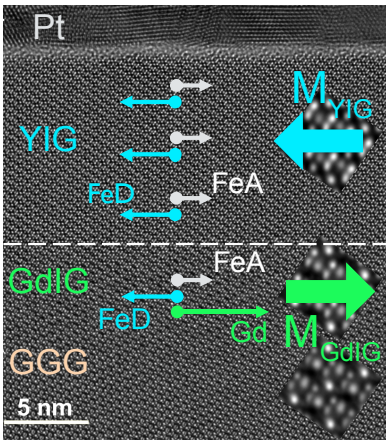

Figure 4.7: **Schematic representation of the different magnetic sublattices.** Sketch of the different magnetic sublattices present in YIG and GdIG, where FeD and FeA are the magnetic sublattices related to the Fe ions and Gd is the magnetic sublattice of the gadolinium ions. M_{YIG} and M_{GdIG} are the net magnetizations for the YIG and GdIG films, respectively.

We are probing only the top surface magnetization by SMR and XMCD, whereas the different boundary conditions lead to different magnetic states at the top and the bottom interface. The complete qualitative picture (see series of sketches in Fig. 4.8) of the magnetic state based on the experimental evidences discussed above would be as follows: the magnetization at the bottom interface of YIG film is strongly antiferromagnetically coupled to the magnetization of the GdIG [98, 142]. At zero magnetic field, the top surface magnetization of the YIG is antiparallel to the magnetic field (as observed from SMR and XMCD measurements), see Fig. 4.8(a). This would be the only situation where the magnetization at the top and the bottom interfaces have the same orientation, leading to an uniform magnetization along the YIG film. When applying a moderate field

(Figs. 4.8(b-d)), the top surface magnetization coherently rotates (as observed from SMR and XMCD measurements). Since moderate fields cannot break the strong antiferromagnetic coupling between Gd moments and FeD moments at the YIG/GdIG interface (the magnetic field needed to break such coupling would be hundreds of teslas, see Ref. [141]), the bottom surface magnetization would be pinned. These two different boundary conditions would lead to a helical magnetization from top to bottom, Figs. 4.8(b-d). Above $\sim$ 1.5 T, the top surface magnetization is mostly aligned with the field, and the helical structure remains (Figs. 4.8(e)). Further increasing the magnetic field favors the parallel alignment of the YIG magnetization, but the antiparallel pinning at the bottom YIG surface would prevent a complete uniform magnetization along the film even at the largest applied field (9 T), see Fig. 4.8(f). This behavior of the magnetization profile is similar to the one reported in Gd/Ni multilayers, also dominated by antiferromagnetic coupling at the interfaces [139]. The behavior of our bilayer is thus equivalent to that of a synthetic antiferromagnet [143], although we are not aware of previous reports of such man-made system with insulating materials.

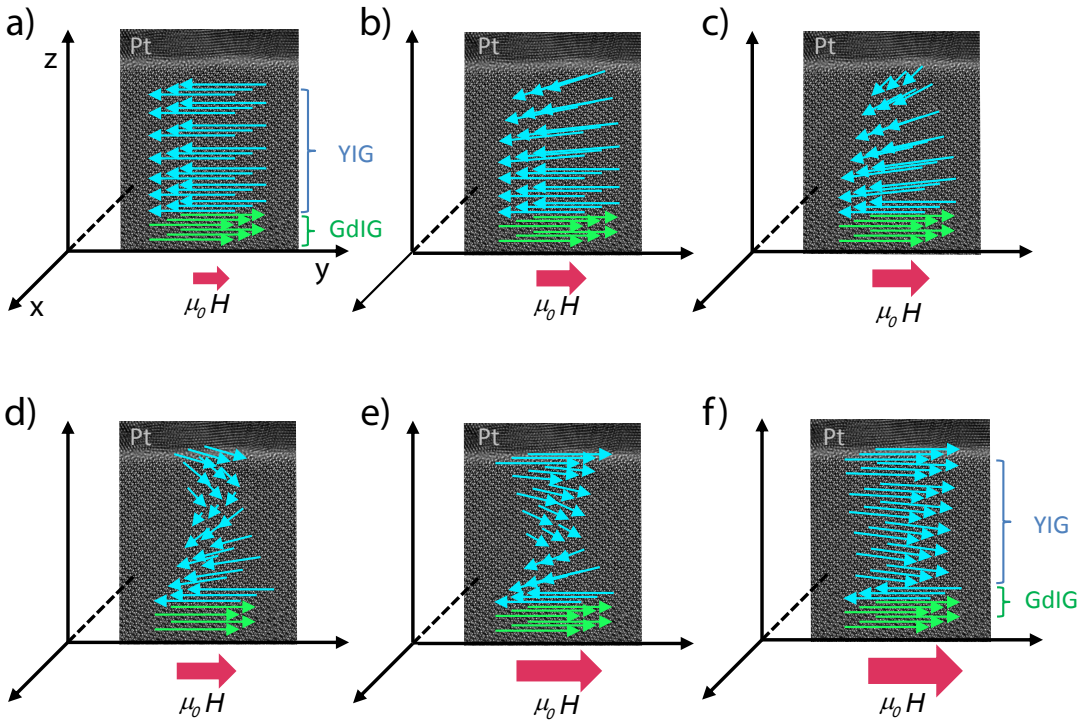

Figure 4.8: **Schematic representation YIG magnetic moments alignment with the external magnetic field.** Sketch of the evolution of the magnetization of the ultrathin YIG film, pinned antiparallel to the GdIG magnetization due to the antiferromagnetic exchange coupling between Gd moments and FeD moments, when an external magnetic field is applied.

4.3.4 Memory effect

The presence of the negative exchange coupling between YIG and GdIG would also explain the sharp switching from the out-of-plane to in-plane magnetization deduced from the shape of the ADMR in the $\beta-$plane (Figs. 4.4(a) and (b)). The strong and opposing demagnetization fields expected from the YIG and the GdIG layers combined with the antiferromagnetic coupling between them would favor the switching of the entire bilayer magnetization to the plane, much sharper than the case of a single YIG layer of similar thickness [81]. This effect is confirmed with detailed FDMR measurements sweeping at low magnetic fields along the $z-$direction (Fig. 4.9): the higher resistance state corresponds to the YIG magnetization pointing out-of-plane and the lower resistance state around zero corresponds to in-plane magnetization. Interestingly, the switching has a clear hysteretic behavior, which is probably due to the complex interplay between antiparallel coupling and the opposing demagnetizing fields of each layer. Switching between two metastables states with orthogonal magnetic configurations can be used in a memory device which is written with a very low magnetic field and read by longitudinal SMR. This would be an advantage with respect to previous proposals of a memory device based on magnetic insulators with perpendicular magnetic anisotropy, because they use the transverse SMR to read the magnetization state, which has a resistance change almost three orders of magnitude smaller [120, 121].

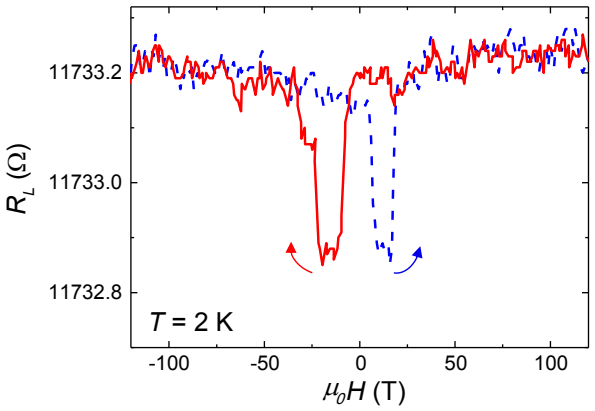

Figure 4.9: **Metastable states with orthogonal magnetic configurations.** Longitudinal FDMR measurement (trace and retrace) at 2 K with the magnetic field applied along the z direction (out-of-plane)

4.4 Conclusions

We structurally and magnetically characterized ultra-thin epitaxial YIG films on GGG, which reveal an atomically well-defined interlayer of GdIG at the YIG/GGG interface. From SMR and XMCD we demonstrate that the YIG magnetization opposes moderate external magnetic fields. This unconventional behavior occurs because YIG/GdIG magnetically couple antiparallel, forming the equivalent to a synthetic antiferromagnet, with the exceptional fact of being insulating. Furthermore, we observe a memory effect between orthogonal magnetization orientations, which can be read with an adjacent Pt film via longitudinal SMR measurements. This bilayer system could be further engineered to optimize the functionalities exploited in insulating spintronic devices, such as writing operations with spin-orbit torque and reading operations with SMR in insulating magnetic memories [120, 121], or in devices where the application of antiferromagnets [144] and their synthetic versions [131] is advantageous.

4.5 Appendix

4.5.1 Appendix A: Magnetic characterization: XMCD measurements

Figure 4.10(a) shows the spectra for circular polarization and the corresponding x-ray absorption spectrum (XAS) of the sample YIG (13 nm)/Pt (2 nm) from where we extract the XMCD curve shown in Fig.4.10(b). This XMCD spectrum is consistent with the $FeL_{2,3}$ edge in thick YIG. We obtained the hysteresis loops by sweeping the magnetic field between 6 T and -6 T in in-plane and out-of-plane configuration and measuring the difference of the XMCD absorption peak (710.2 eV, FeL_3 peak) at 2 K. The in-plane hysteresis loop is shown in Fig. 4.5(d), whereas the out-of-plane hysteresis loop is shown in Fig. 4.10(c), confirming the hard magnetization behavior of our sample due to the strong shape anisotropy.

The non-zero value of magnetization at $H = 0$ T in Fig. 4.5(d) in the main text is an artifact of the XMCD renormalization of the hysteresis loop. This renormalization is unavoidable since the electron yield is sensitive to the applied magnetic field leading to a drop in the XMCD signal. The effect is enhanced for high magnetic fields and when this is applied perpendicular to the flow of electrons. To circumvent this effect, the XMCD signal is renormalized by the XMCD signal out of resonance. For magnetic fields close to zero, the renormalization gives rise to spikes in the signal.

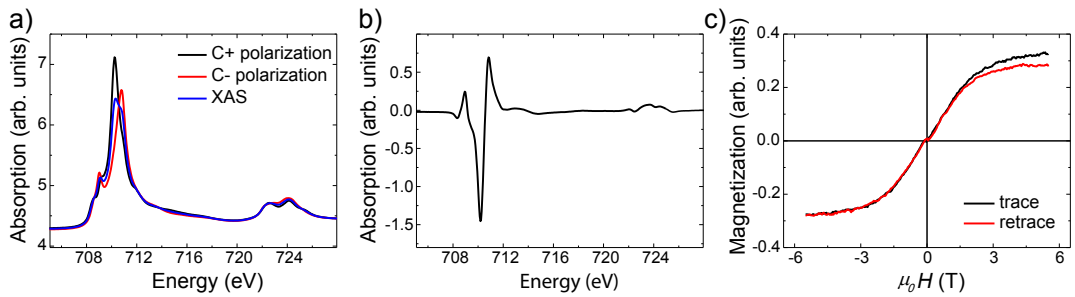

Figure 4.10: **Magnetic characterization by x-ray circular dichroism.** (a) Absorption spectra for positive (black line) and negative (red line) circularly polarized light and X-ray absorption spectrum (blue line) at 2 K and 6 T. (b) XMCD spectrum extracted from the XAS measurements. (c) Hysteresis loop measured by XMCD with the magnetic field applied out of plane at 2 K.

4.5.2 Appendix B: Physical mechanism leading to a preference in the rotation direction

Concerning the physical mechanism leading to a preference in the rotation direction in (Fig. 4.6(c)), we can rule out several possibilities:

(i) The sweep direction of the angle does not play any role because all ADMR measurements in Fig. 4.5(a) were performed from 0^o to 360^o and back, and the curves were identical, no difference or discontinuity was observed. This indicates that, once the locking angle between magnetic field and surface magnetization is defined after a given field is applied, this angle does not change when the field rotates in whatever direction during the ADMR measurement.

(ii) The magnetic anisotropy of YIG (111) is dominated by an easy plane (the plane of the film). There are in fact 6 easy axes in plane corresponding to the <110> axes [145]. Such in-plane magnetocrystalline anisotropy is weak and the in-plane magnetization saturates at few Oe (see, for instance, Ref. [146]). Since our phenomenon of magnetization dephasing with respect to the field occurs above 0.2 T, the anisotropy of the crystal axes should not be relevant.

(iii) The current (I) to probe SMR was kept fixed for all measurements shown in the main text (100 μA), but we have previously confirmed that the SMR amplitude is independent of the current used, as expected from a linear effect. The possibility that the induced spin accumulation from the SHE in Pt could exert a torque to the YIG magnetization large enough to give a preferential rotation direction is also ruled out by the fact that we use the dc-reversal method to measure the resistance (i.e. we average $+I$ and $-I$ to remove thermoelectric effects and drifts from the measured voltage, as it was explained in section 2.2.1). With this set up, a $+I$ would create a spin accumulation with opposite polarity

to the one created by $-I$, averaging the torque to zero.

Taking into account that the probability of clockwise and counter-clockwise rotation should be the same given the easy plane anisotropy of YIG (111), the most likely scenario is that small defects in the crystal acting as pinning sites and/or slight field misalignments determine which one of the two rotation directions takes place.

4

Chapter 5

Spin Hall magnetoresistance in a paramagnetic insulator

In this chapter, we study the spin Hall magnetoresistance in a Pt/GGG interface at low temperatures and large magnetic fields, where GGG is a textbook paramagnetic insulator. The observed magnetoresistance is well explained by spin Hall magnetoresistance theory that takes into account the paramagnetic behavior of the localized spin in GGG and includes the exchange coupling between the conduction electron-spins in Pt and the localized spins in GGG. Our result establishes the spin transport based on the spin-mixing conductance at metal/paramagnetic insulator interfaces. This work was performed in collaboration with Prof. Eiji Saitoh during the secondment of his Ph.D student Koichi Oyanagi in our laboratory. Furthermore, the fitting to our experimental data are perfomed by our collaborators X.-P. Zhang, Dr. V. N. Golovach and Prof. S. Bergeret.*

*Published as: K. Oyanagi†, Juan M. Gomez-Perez†, X.-P. Zhang, E. Sagasta, T. Kikkawa, F. S. Bergeret, V. N. Golovach, L. E. Hueso, F. Casanova, and E. Saitoh, Paramagnetic spin Hall magnetoresistance, *in preparation*. †Equal contribution.

5.1 Introduction

In previous **Chapters 3** and **4**, we have studied the interface between Pt and YIG, that is well known and broadly study. However, other magnetic insulators are attracting the attention for new physics and phenomena to be studied by SMR. For instance, non-local experiment through a paramagnetic insulator shows an efficient spin transport at the interface by spin-flip scattering, suggesting that the spin-sink conductivity G_s can be vital for the HM/PMI interface in addition to the G_r and G_i [84, 147], see Fig. 5.1(b). In contrast to the magnetization of the ferromagnets (Fig. 5.1(a)), the magnetization of paramagnets are free from the exchange stiffness, and it can be controlled by weak magnetic fields.

In this chapter, we report for the first time the observation of spin Hall magnetoresistance in a HM/PMI interface. At very low temperature, we observe the full picture of SMR in a PMI, which is well described by the microscopic theory introduce in section 1.5.5, allowing us to extract the parameter governing the spin transport at the interface. Furthermore, the estimated field-like torque (quantified as G_i) is in the same order of magnitude than that of the spin-transfer torque (quantified as G_r), in contrast to YIG case.

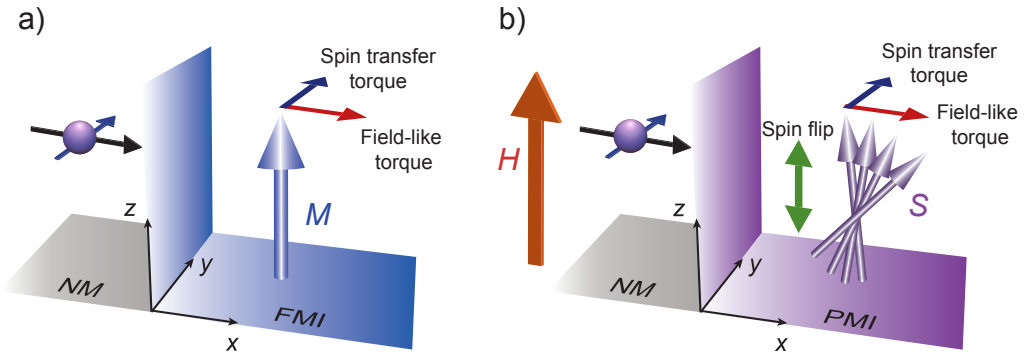

Figure 5.1: **Spin transport at heavy metal/ferromagnetic insulator interface and heavy metal/paramagnetic insulator interface.** (a)-(b) Illustration of the transfer of angular momentum from the heavy metal to (a) FMI and to (b) PMI. M, H and S represent the magnetization, applied magnetic field and localized spin, respectively. The blue and red and green arrows represent the torque direction related to the spin transfer torque and field-like torque, respectively. The green arrow represents how the spin flip can modify the amplitude of the magnetization.

5.2 Experimental details

We studied the interface between Pt and *gadolinium gallium garnet* ($Gd_3Ga_5O_{12}$, GGG). GGG is a paramagnetic insulator which shows large band gap $E_g = 6$ eV [148] and short-range magnetic order [100]. Figure 5.2(a) shows

the temperature T dependence of the GGG magnetization M under an applied magnetic field H of 0.1 T. M increases with decreasing T following the Curie-Weiss law. The inset of Fig. 5.2(a) indicates the Curie-Weiss temperature θ_{CW} of -2 K [149]. Figure 5.2(b) shows the hysteresis loop ($M-H$) measurements of GGG at different T, which confirm a clear paramagnetic behavior with T of the GGG. The magnetization of GGG arises from Gd^{3+} ion with spin $-7/2$, and each Gd^{3+} ion is coupled by the weak nearest-neighbor exchange interaction ($J_{ex} \sim 0.1$ K [150]). Because of the half-filled $4f-$shell in Gd^{3+}, the orbital angular momentum is zero, and thus GGG shows a small magnetic anisotropy of 0.04 K [151, 152].

The devices were fabricated on top of a single-crystalline GGG (111) provided by CRYSTAL GmbH. A 5-nm-thick Pt film was magnetron-sputtered (80 W; 3 mTorr of Ar) on top of GGG. A Pt Hall bar (width $w = 100$ μm and length $l = 800$ μm) was patterned by negative photolithography and Ar-ion milling process, as described in section 2.1. Magnetotransport measurements were performed as explained in section 2.2.1.

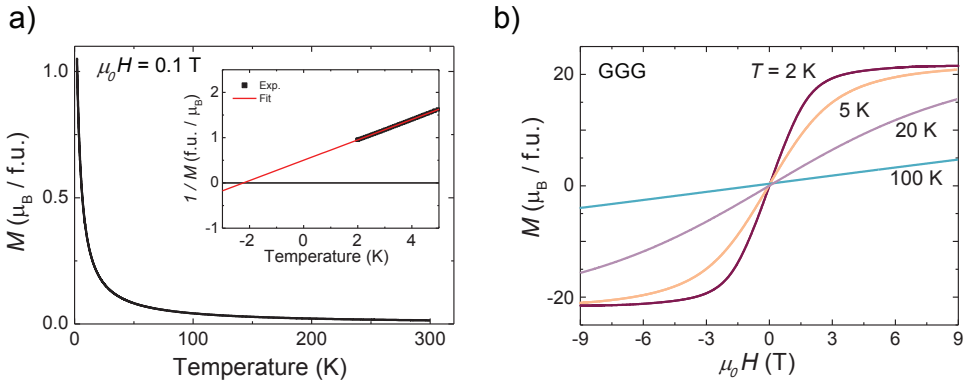

Figure 5.2: **Temperature dependence of the magnetization and hysteresis loop measurements.** (a) T dependence of the GGG M at $H = 0.1$ T. The inset shows the temperature dependence of $1/M$. The red line indicates the linear fit showing the Curie-Weiss temperature $\theta_{CW} = -2$ K. (b) $M-H$ curves at different T.

5.3 Results and discussion

5.3.1 Magnetotransport measurements

SMR appears in both longitudinal and transverse resistivities. However, in the longitudinal resistivity measurement at low temperature ($T < 50$ K) and high magnetic fields an extra magnetoresistance due to the weak anti-localization (WAL) in Pt always appears, which is much larger magnetoresistance than SMR

and masks it as it was shown in Fig. 1.12(b). Therefore, we mainly focus on the transverse resistivity measurement (see section 5.5.1 for longitudinal measurements) in the $\alpha-$plane, where WAL does not contribute to the magnetoresistance measurements.

5.3.2 Quantification of SMR amplitude $\Delta\rho_1/\rho$

We measured the transverse resistivity ρ_T with the external H applied in plane ($\alpha-$plane). First of all, we performed FDMR at $\alpha = 45^o$ and 135^o, where SMR shows the maximum and minimum amplitude, respectively (Eq. 1.24). Figure 5.3(a) shows the FDMR curve of the normalized ρ_T at 2 K. At $\alpha = 45^o$, ρ_T increases up to $H = 5$ T, for $H > 5$ T ρ_T saturates. On the other hand, at $\alpha = 135^o$ ρ_T decreases with H, being consistent with the SMR symmetry [53, 79].

Figure 5.3(b) shows the transverse ADMR measurement ρ_T/ρ at 2 K and 3.5 T with H swept in the $\alpha-$plane. ρ_T/ρ shows a maximum and minimum at $\alpha = 45^o$ and $\alpha = 135^o$, respectively, showing a clear $\sin\alpha\cdot\cos\alpha$ dependence as expected from Eq. 1.24. By fitting the transverse ADMR at 2 K and different magnetic fields, we can obtain the SMR amplitude $\Delta\rho_1/\rho$. We can see clearly that the SMR amplitude extracted from the transverse ADMR is the same than the difference between the transverse FDMR at 45^o and 135^o at the same H, see Fig. 5.3.

The FDMR saturation (Fig. 5.3(a)) cannot be explained by Hanle magnetoresistance [54], which has the very same ADMR symmetry of SMR but depends on the square of H. Therefore, the observed transverse magnetoresistance can be only due to SMR because of the field-induced magnetization in GGG.

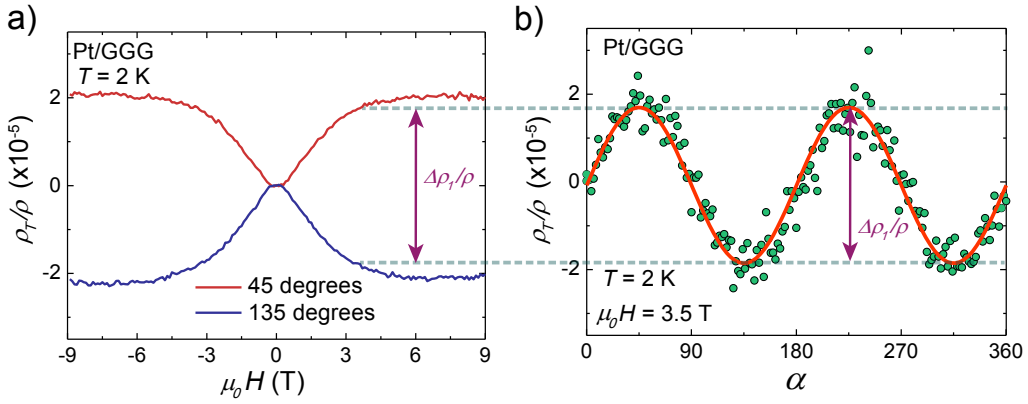

Figure 5.3: **Transverse magnetoresistance measurements.** (a) Transverse FDMR at $\alpha = 45^o$ and $\alpha = 135^o$ at 2 K. (b) Transverse ADMR at 2 K and 3.5 T. The solid line is the $\sin\alpha\cdot\cos\alpha$ fitting to extract the SMR amplitude $\Delta\rho_1/\rho$.

In order to provide further evidences of the SMR scenario in a PMI in the section 5.5.1 we show the longitudinal resistivity measurements.

5.3.3 Quantification of SMR amplitude $\Delta\rho_2/\rho$

In Section 1.5.4 of the introduction we discussed the existence of an anomalous Hall-like contribution measured in Hall-configuration (Fig. 2.5(e)), which is fully understood by the G_i in the SMR scenario [65, 79, 82, 153]. In the particular case of YIG, G_i is at least one order of magnitude smaller than G_r leading to a small contribution, we saw in **Chapter 3** that $\Delta\rho_2/\rho$ is 100 times smaller than $\Delta\rho_1/\rho$ [48, 79, 82, 153]. However, in the case of a PMI the phenomenon could be different. When the attached PMI acquires a field-induced magnetization in $z-$direction, the contribution of all the localized moments to the effective exchange interaction with the Pt conduction electrons might lead to a larger exchange field, i.e., a larger G_i.

Therefore, we perform magnetoresistance measurements by using Hall configuration (Fig. 2.5(e)). Figure 5.4(b) shows the normalized transverse resistivity ρ_T/ρ at 2.5 K. At large magnetic fields, a clear linear dependence with H can be observed, related to the ordinary Hall effect (OHE) in Pt, see inset of Fig. 5.4. Close to zero field, we found a non-linear dependency with H. In order to study this signal, we subtracted the linear response of OHE from ρ_T/ρ. Figure 5.4 shows the H dependence of ρ_T/ρ after subtracting the OHE background, $\Delta\rho_2/\rho$. $\Delta\rho_2/\rho$ is negative for positive H, changing the sign for negative H, which is consistent with the symmetry of the AHE-like expected from SMR theory, see Eq. 1.24 [65]. At $T = 2.5$ K, $\Delta\rho_2/\rho$ saturates around $H \sim 5$ T as it was shown in Fig. 5.3(b) for

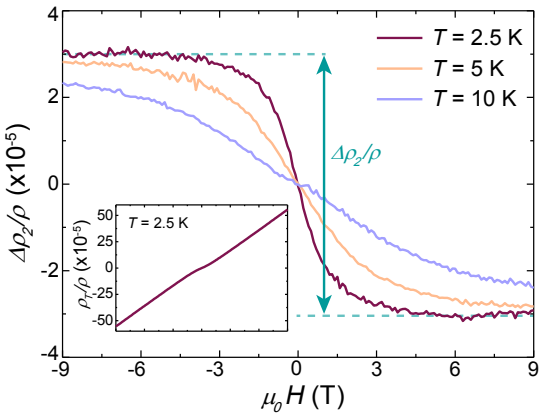

Figure 5.4: **Field dependence of anomalous Hall-like effect.** AHE-like term as a function of the magnetic field at 2.5 K, 5 K and 10 K, after subtracting the linear term related to the OHE (inset shows the raw data).

transverse SMR at the same T. Moreover, opposed to YIG, the saturation value of $\Delta\rho_2/\rho \sim 3 \times 10^{-5}$ is in the same order of magnitude as that of $\Delta\rho_1/\rho$. We can also observe this behavior at 5 K and 10 K, with a larger saturation H, which is the same behavior than that of the GGG magnetization presented in Fig. 5.2(b). Therefore, we can infer that the observed AHE-like behavior corresponds to the component predicted by the SMR theory, which is induced by the paramagnetic moments.

5.3.4 Calculation of the spin-mixing conductance

We model the paramagnetic SMR by using the microscopic theory introduced in Section 1.5.5 [84]. This theory considers the spin transfer at the PMI/HM interface *via* exchange interaction between the conduction electron-spins in the HM and the localized spins in the PMI.

The Pt resistivity is $\rho_{Pt} = 34\ \mu\Omega$·cm. From ρ_{Pt} we can calculate the following parameters [42]: $\theta_{SH} = 0.16$ and $\lambda_{Pt} = 2$ nm. With these parameters and the G-terms defined in Eqs. 1.28−1.30 we can fit our experimental data $\Delta\rho_1/\rho$ and $\Delta\rho_2/\rho$ as a function of H. Therefore, we perform the fittings with the Weiss theory approximation as in Ref. [84], where the free parameters are $\nu_F J_{int}$ and n_{imp}^{2D}. $\nu_F J_{int}$ represents the exchange interaction between the magnetic moments in GGG and the conduction electrons in Pt, and n_{imp}^{2D} is the density of magnetic moment per unit area at the interface. Figure 5.5(a) shows the field dependence of the experimental data for $\Delta\rho_1/\rho$ (purple circles) and $\Delta\rho_2/\rho$ (blue circles), and the fittings (purple lines for $\Delta\rho_1/\rho$, blue line for $\Delta\rho_2/\rho$) at 2 K for $H > 0$ range.

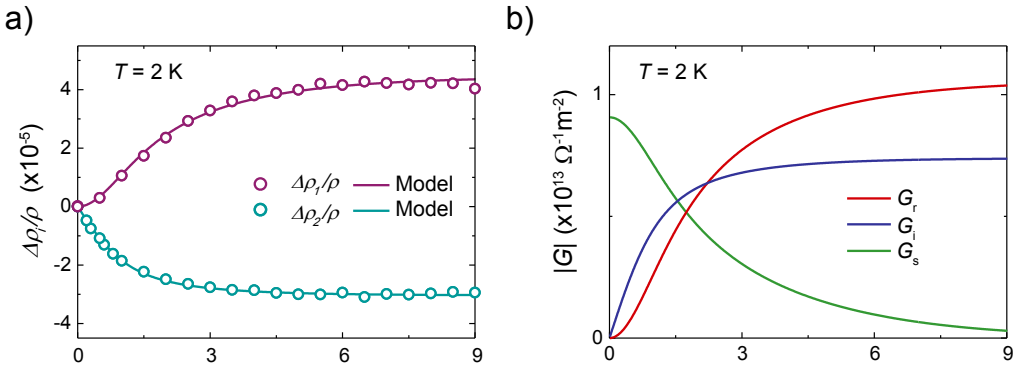

Figure 5.5: **Comparison between the experimental results and theoretical fitting, magnetic field dependencies of the spin-mixing conductance terms.** (a) $\Delta\rho_1/\rho$ (purple circles) and $\Delta\rho_2/\rho$ (blue circles) as a function of H, and the fits to Eqs. 1.33−1.33 using Curie-Weiss model (purple lines and blue line, respectively) at 2 K for $H > 0$ range. (b) Spin-mixing conductances obtained from the fittings at in panel (a). The red, blue and green lines represent G_r, G_i and G_s, respectively.

The best fitting for both amplitudes exactly reproduces the H dependence of the signals with the finite values for the G terms shown in Fig. 5.5(b). At zero H, G_r and G_i vanish, while G_s takes its maximum value 8×10^{12} $\Omega^{-1}\mathrm{m}^{-2}$. When H increases, G_r (G_i) increases and tends to saturate to $G_r \sim 1 \times 10^{13}$ $\Omega^{-1}\mathrm{m}^{-2}$ ($G_i \sim 7 \times 10^{12}$ $\Omega^{-1}\mathrm{m}^{-2}$). However, G_s monotonically decreases to zero at large H.

According to the theory, the anisotropic spin relaxation of the conduction electron-spin in Pt leads to finite a G_r and G_i. In a FMI, the spontaneous M breaks the symmetry and causes the anisotropic spin scattering and, thus, spin transport at the interface. However, in the case of a PMI, at zero H, the absence of a net M due to the randomized spins ($\langle S_\parallel \rangle = 0$), G_r and G_i vanish because of the isotropic spin relaxation times. Therefore, the anisotropic spin relaxation only appears when H induces a net M in the PMI, which increases with H. Therefore, G_r and G_i increase with H. However, G_s decreases with H because the spin-flip scattering at the interface is reduced by increasing H. This picture is only possible due to the Zeeman gap opened in the spin stated of the localized spins. At low magnetic fields, the Zeeman gap ($\propto g\mu_B H$) and the large susceptibility of GGG indicate that the localized spin direction can be easily modified by the transfer of spin angular momentum between the conduction electron-spins and the localized spins, which corresponds to the maximum G_s. Nonetheless, when H increases, the degeneracy of the paramagnetic spins in GGG lifts with the energy gap given by the Zeeman effect. The energy scale of the SHE-induced spin-flip scattering is governed $K_B T$, at low temperatures, which means that the spin-flip scattering can be suppressed by the large Zeeman gap. Therefore, when the Zeeman gap (9 T $\approx$ 25 K) exceeds the thermal energy ($\approx$ 2 K) significantly, G_s vanishes.

Regarding the mechanism that leads to $\Delta\rho_1/\rho$ and $\Delta\rho_2/\rho$ at the Pt/GGG interface, our results indicate that both spin-transfer torque and field-like torque play a crucial role at HM/PMI interfaces. On the one hand, Fig. 5.6(b) shows the comparison between G_r and $\Delta\rho_1/\rho$ as a function of H. From this comparison, we

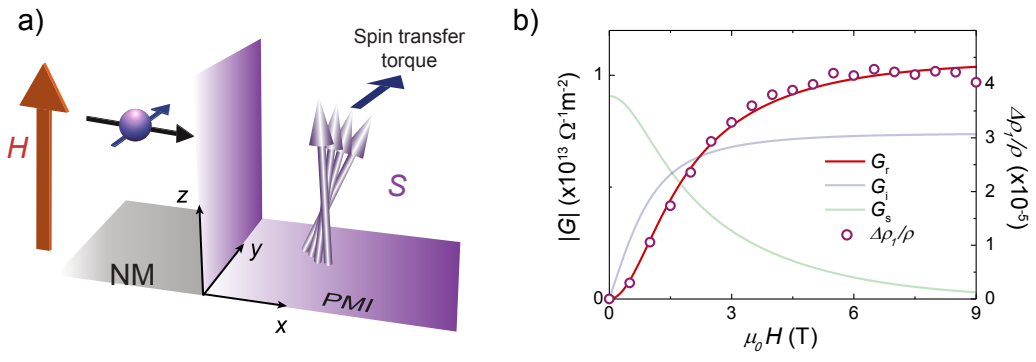

Figure 5.6: **Mechanism of $\Delta\rho_1/\rho$ term in a paramagnetic insulator.** (a)-(b) The mechanism of SMR in a PMI.

found that $\Delta\rho_1/\rho$ is directly proportional to G_r. G_r is responsible of the spin-transfer torque efficiency, therefore, the agreement shown in Fig. 5.6(b) indicates that $\Delta\rho_1/\rho$ is driven by spin-transfer torque in Pt/GGG. On the other hand, Fig. 5.7(b) shows the comparison between G_i and $\Delta\rho_2/\rho$ as a function of H. It can be seen that both H dependencies are in good agreement. Therefore, in this case, $\Delta\rho_2/\rho$ is proportional to G_i that represents the field-like torque efficiency, meaning that G_i induces $\Delta\rho_2/\rho$ in Pt/GGG. We can also notice that the saturation is faster in $\Delta\rho_2/\rho$ than in $\Delta\rho_1/\rho$, and this is because $\Delta\rho_2/\rho$ is directly proportional to $\langle\widehat{S}_{\parallel}\rangle$ (see Eq. 1.29) whereas $\Delta\rho_1/\rho$ is proportional to $\langle\widehat{S}^2_{\parallel}\rangle$ (see Eq. 1.28).

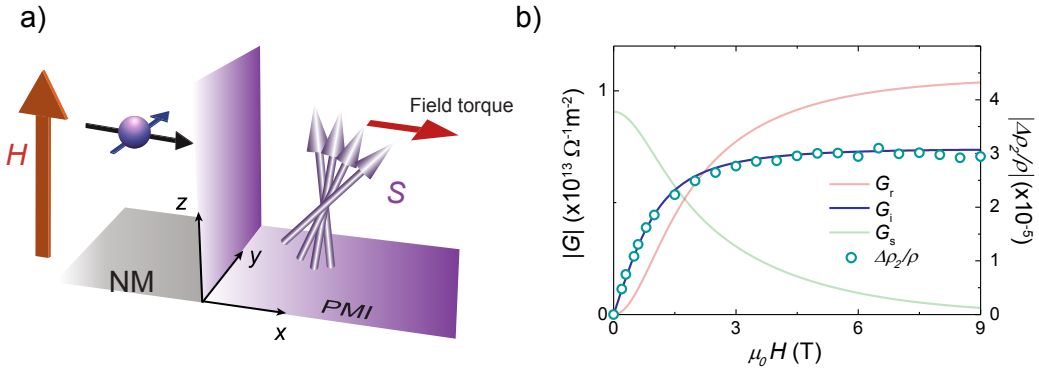

Figure 5.7: **Mechanism of $\Delta\rho_2/\rho$ term in a paramagnetic insulator.** (a)-(b) The mechanism of AHE-like SMR in a PMI.

We have extracted the values of the spin-mixing conductances in Pt/GGG interface, where we found that both spin-transfer torque and field-like torque are equally important. We compare the values obtained from Pt/GGG with Pt/YIG (see section 3.3), we observed that $G_r \sim 1 \times 10^{13}$ $\Omega^{-1}\mathrm{m}^{-2}$ in Pt/GGG is about one order of magnitude smaller than that in Pt/YIG, $G_r \sim 1 \times 10^{14}$ $\Omega^{-1}\mathrm{m}^{-2}$. However, if we compare the two imaginary terms of the spin-mixing conductance, they are $G_i \sim 1 \times 10^{13}$ $\Omega^{-1}\mathrm{m}^{-2}$ for both interfaces.

Finally, from the fitting, we can also extract the Curie-Weiss temperature θ_{CW}, n^{2D}_{imp} at the HM/MI interface $\nu_F J_{int}$. For the fits shown in Fig. 5.5(a) the best fitting parameters are $\theta_{CW} = -0.66$ K, $n^{2D}_{imp} = 6.7 \times 10^{16}$ atoms/m^2 and $\nu_F J_{int} = 1.3 \times 10^{-5}$. Even though the bulk θ_{CW} for GGG is -2 K [inset Fig. 5.2(a)], we extracted a smaller value of -0.66 K. SMR is only sensitive to the magnetic properties at the MI surface, thus, the estimates θ_{CW} indicates that the effective exchange interaction between the Gd moments at the interface is smaller than that in the bulk. we found that n^{2D}_{imp} is just 1% compare to the ideal value $n^{2D}_{imp} = 1/a^2_{Gd} = 6.9 \times 10^{18}$ atom/m^2, where $a^2_{Gd} = 0.38$ nm is the atomic distance between the Gd moments. These results are confirmed by the transmission electron microscopy (TEM) image shown in Fig. 5.8(a), where there

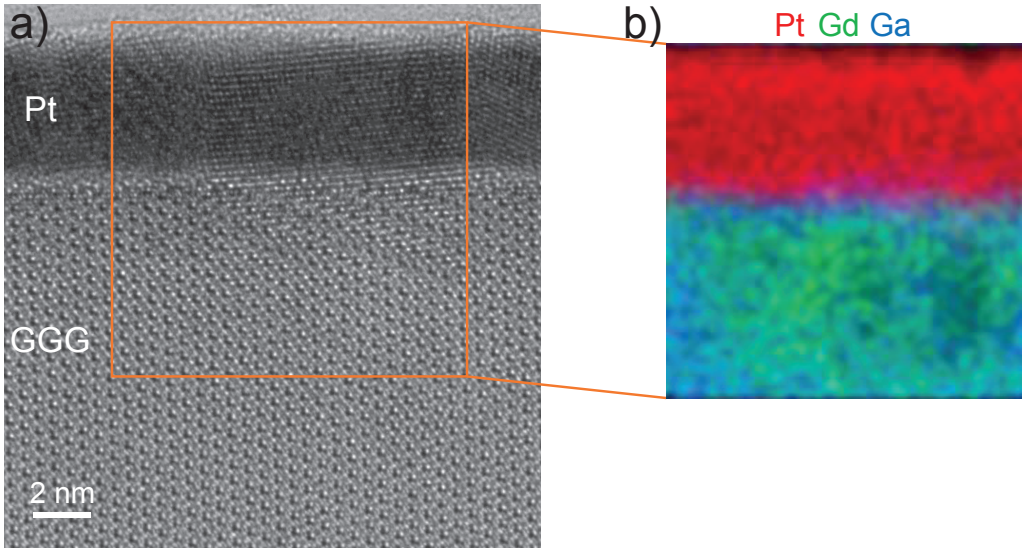

Figure 5.8: **Transmission electron microscopy image and energy dispersive X-ray analysis.** (a) TEM image of the Pt/GGG interface. (b) EDX color map of the region close to the Pt/GGG interface. The colors red, green and blue represent Pt, Gd and Ga, respectively.

is a small region at the interface (around 0.5 nm in depth) that is Ga rich (Fig. 5.8(b)), which could explain the low n_{imp}^{2D} at the interface.

The last parameter extracted is the *s-f* exchange interaction between the conduction electron of Pt and the localized spins in the $4f$ shell of Gd at the Pt/GGG interface, which is $J_{int} = 10$ meV. Up to now, the interface exchange coupling between conduction electron and $4f$ electron is assumed to be small. J_{int} represents the overlap of the conduction electron and the localized spin, and it can be smaller for Pt/GGG than for Pt/YIG. This can be due to the strongly localized $4f$ electrons in Gd^{3+} overlaps less with the conduction electrons in Pt in comparison to the $3d$ electrons in Fe^{3+} (responsible of YIG magnetism). The estimated J_{int} is the same than that of Pt/YIG interface extracted in Ref. [19]. However, they assumed the ideal density Fe^{3+} at the interface, which could lead to an underestimation of J_{int}. Another example is the work of R. Schlitz *et. al.* where they already suggested the weak exchange coupling in Pt/GGG [154]. The small interfacial *s-f* exchange interaction is also assumed small in the experiments of spin Seebeck effect [98]. Our analysis of SMR using the newly developed theory allows us to quantify key parameters at the interface of HM/MI, demonstrating the power of such technique.

5.4 Conclusions

To sum up, we demonstrate, for the first time, the presence of SMR in Pt on top of GGG, which is a paramagnetic insulator. The paramagnetic SMR amplitudes $\Delta\rho_1/\rho$ and $\Delta\rho_2/\rho$ show up by applying large magnetic fields at 2 K. We use the microscopic theory of SMR to relate the observed signal with the spin-mixing conductance at the interface, where we find that the field-like contribution (G_i) is as important as the spin-transfer torque contribution (G_r) in Pt/GGG interface. Finally, we can quantify the exchange interaction between conduction electron in Pt and $4f$ localized spins in Gd^{3+} ($J_{int} \sim 10$ meV).

5.5 Appendix

5.5.1 Appendix A: Longitudinal magnetoresistance measurements

First, we performed the longitudinal FDMR measurements at room temperature in the three-main axes x, y and z direction as it is depicted in the sketch of Fig. 5.9(a). At high temperature, where the GGG magnetization is expected to be negligible and, thus, the SMR contribution, we could expect to measure the intrinsic Hanle magnetoresistance (HMR) in Pt [54]. HMR has the same symmetry that that of SMR with respect of H direction: only appearing when the magnetic field is applied perpendicular to the spin accumulation, H_x and H_z. Figure 5.9(a) shows the FDMR at 300 K in $x-$ and $y-$direction. There is no de-

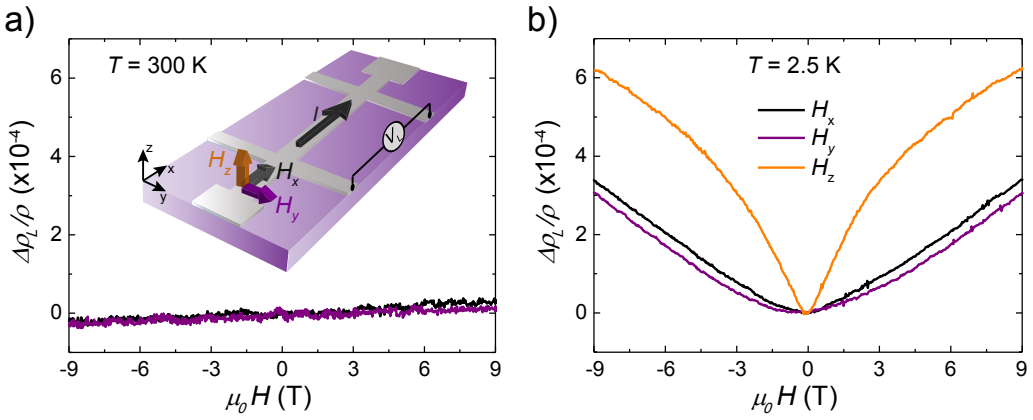

Figure 5.9: **Longitudinal field-dependent magnetoresistance measurements.** (a)-(b) FDMR measurements at (a) 300 K and (b) 2.5 K, in the three main axes defined in the sketch of panel (a).

pendency appreciable as a function of H in $x-$direction. Our results present the absence of HMR in our sample at room temeperature. Moreover, HMR weakly depends on T [54,155]. Therefore, we can clearly discard the presence of HMR in our sample, which depends on the Pt growth condition as discussed in Ref. [54].

Secondly, we measured the longitudinal FDMR at low temperatures, as shown inFig. 5.9(b). Below 50 K, we observe a large magnetoresistance contribution due to WAL. This behavior is already explained in Refs. [54,78]. In spite of WAL, we can extract the SMR amplitude from the difference $\Delta\rho_L(H_x)/\rho - \Delta\rho_L(H_y)/\rho$ as we show in Fig. 5.10(a). The $\Delta\rho_1/\rho$ amplitude extracted from FDMR measurements should be the same than that measured by ADMR (Fig. 5.10(b)), which is confirm in in Fig. 5.10(c). Both H dependencies show the same trend. Moreover, the saturation $H \sim 5$ T and the amplitude value $\sim 3 \times 10^{-5}$ at 5 T, are in agreement with the ones extracted in the transverse configuration, Fig. 5.3. Finally, we studied the temperature dependence of $\Delta\rho_1/\rho$ extracted from the fitting of the ADMR to the $\cos^2\alpha$, plotted in Fig. 5.10(d). Once again, the T dependence is similar than that of GGG magnetization (Fig. 5.2(a)). In summary, the longitudinal measurements confirm the SMR scenario in Pt/GGG.

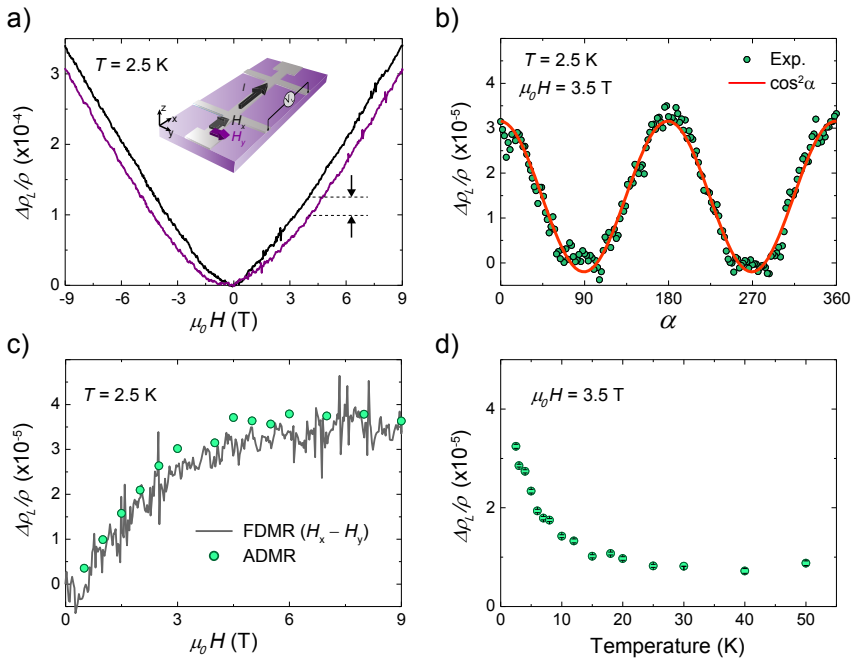

Figure 5.10: **Longitudinal magnetoresistance measurements.** (a) FDMR measurements in x and y directions. The dashed lines and the arrows describe the longitudinal SMR amplitude ($\Delta\rho_1/\rho$) measured in (b) by ADMR, i.e., byrotating the magnetic field in the plane of the sample. The red line is the $\cos^2\alpha$ fitting to extract the amplitude, $\Delta\rho_1/\rho$. (c) Comparison of the $\Delta\rho_1/\rho$ obtain from the difference of the FDMR along x and y directions and from the ADMR in $\alpha-$plane.

5

Chapter 6

Spin Hall magnetoresistance in a ferromagnetic insulator

Spin-dependent transport at heavy metal (HM)/magnetic insulator (MI) interface can be described in terms of three parameters: the so-called spin-sink conductance G_s and the real and imaginary part of the spin-mixing conductance, $G_{\uparrow\downarrow} = G_r + iG_i$. Each parameter is relevant for different spin-dependent phenomena. For example, G_s originates from spin-flip processes and therefore is the leading parameter in inelectrical and thermal excitation of magnons, whereas G_r plays a fundamental role in spin-pumping experiments. On the other hand, G_i is the quantification of the interfacial exchange field, which induces a field like torque in the conduction electrons of the HM. These conductances are broadly studied in ferrimagnetic insulators, where usually the contribution of G_r is much larger than that of G_i, leading to only few reports about the exchange field at HM/MI interface. In this chapter, we investigate for the first time the SMR in a bilayer made of HM and ferromagnetic insulator (FMI). The FMI is EuS, which shows a ferromagnetic behavior below 30 K. We demonstrate that, in a Pt/EuS the G_i contribution (associated with a field-like torque) can be up to four times larger than the G_r term (associated to the Slonczewski torque). This work was done in collaboration with two different groups from the Material Physicis Center (CFM) in Donostia-San Sebastian (Spain): (i) the EuS growth was performed by Dr. M. Ilyn, Dr. C. Rogero and C. Gónzalez-Orellana and (ii) the theoretical fitting to our experimental data are done by X.-P. Zhang, Dr. V. N. Golovach and Prof. S. Bergeret.

6.1 Introduction

In previous chapters, we have introduced different HM/MI hetersotructures that have been characterized by SMR measurements. We have investigated the spin-mixing conductance ($G_{\uparrow\downarrow}$), at the heart of the SMR, what gives essential information about spin transport at the interface. HM/MI interfaces have been extensively studied in different MIs, for instance, ferrimagnetic insulators, basically YIG, [66, 75, 76, 79, 81–83, 156], antiferromagnetic insulators such as NiO, Cr_2O_3 and CoO [157–161] as well as compensated ferrimagnetic insulators such as $Gd_3Fe_5O_12$ [162] or spiral ferrimagnets such as $CuOSeO_2$ [163]. More recently, potential candidates can be a low dimensional ferromagnet [164] or, as we performed in **Chapter 5**, paramagnetic insulators [154, 165–167]. However, so far there are no reports in SMR characterizing purely ferromagnetic insulators (FMI). In 2006, A. Brataas and coworkers [58] suggested that, at the interface of a FMI, such as europium chalcogenides, G_i might dominate over G_r. According to the original theory of SMR [65], large enough values of G_i should lead to an AHE-like contribution ($\Delta\rho_2/\rho$). This effect has been poorly studied so far mainly because of the small number of FMIs with large enough Curie temperature (T_c) available. An example of FMI is EuS, with a T_c typically around 16 K. This FMI in combination with conventional superconductors, as for example Al, has been studied for decades in the context of the magnetic proximity effect [168–171]. The exchange interaction between the conduction electrons of the superconductor and the localized magnetic moments of the EuS leads to a spin-splitting field in Al, even in the absence of an external magnetic field. Such spin-split in superconductors are subjected to an intense research [172, 173] because their possible applications in cryogenic memories [174], thermoelectric detectors [175], superconducting spintronics and caloritronics [176, 177], and in the field of the topological superconductivity induced in the superconducting hybrid structures [178, 179]. All these applications require a spin-splitting field induced in the superconductor adjacent to a FMI. Such field is proportional to the G_i parameter and, therefore knowledge of the latter is crucial.

In this chapter, we report the first SMR measurement in Pt/EuS, from which we can extract the values of G_i as a function of the temperature. Our results demonstrate the clear evidence of the AHE-like component related to the SMR scenario. We fit our temperature dependent SMR amplitudes using with a random phase approximation (RPA) and Weiss field theory (WFT) models with the microscopic theory for SMR [84]. From the fittings, we demonstrate that, in ferromagnetic insulators, where the absence of compensated magnetic moments is clear, the imaginary part of the spin-mixing conductance is similar and up to 4 times larger than the real part. Our project highlights field-like torque in SMR

with ferromagnetic insulator systems.

6.2 Experimental details

EuS/Pt samples were prepared by patterning a Pt Hall bar (width $w = 500$ μm, length $L = 900$ μm, and $d_N = 5$ nm) on top of SiO_2(150 nm)/Si by photolithography process and magnetron-sputtering deposition. EuS was evaporated by our collaborators from the Material Physics Center (CFM). EuS layer was *ex-situ* evaporated on top of the Pt film: the sample was inserted in a UHV preparation chamber (base pressure 10^{-9} mbar) and left for twelve hours at room temperature. EuS was grown by means of sublimation of a stoichiometric EuS powder (99.9% purity) in a commercial e-beam evaporator. Growth rate calibrated with a quartz microbalance was 0.5 nm/min (total thickness is 14 nm). During preparation, the substrate was kept at room temperature. In previous chapters, the Pt layer was deposited on top of the MI, in this case we had to change the order of the stack in order to not damage the EuS during the Pt deposition. Figure 6.1(a) shows a sketch of our Hall bar device. We characterize the film and interface quality by transmission electron microscopy (TEM)/scanning TEM (STEM). SMR measurements to extract the SMR amplitudes were performed as explained in section 2.2.1.

6.3 Results and discussion

6.3.1 Structural and magnetic characterization

Figure 6.1(a) shows a sketch of the device geometry and the measurements configuration. First of all, we characterized the interface quality of the Pt/EuS by TEM and STEM. Figure 6.1(b) shows the stack of Pt/EuS grown on top of SiO_2. at the top of the SiO_2 we can see the polycrystalline 5-nm-thick layer of Pt and, on top of that, the EuS layer. In principle, we grew 14 nm of EuS, but from the TEM image and the energy dispersive X-ray spectroscopy (EDX) analysis, we observe that the upper 4 nm of the EuS are oxidized and present an amorphous structure. However, close to the Pt, the EuS has the right composition and crystalline structure, which means that the interface between the Pt and EuS is of good quality for the SMR measurements. After the structural characterization, we studied the magnetism of the EuS film. Figure 6.1(c) shows the temperature dependence of the EuS magnetization (M) measured at $H = 0.1$ T. EuS exhibits a clear ferromagnetic behavior below 30 K, in agreement with previous reports [180, 181]. However, no saturation behavior is observed at very

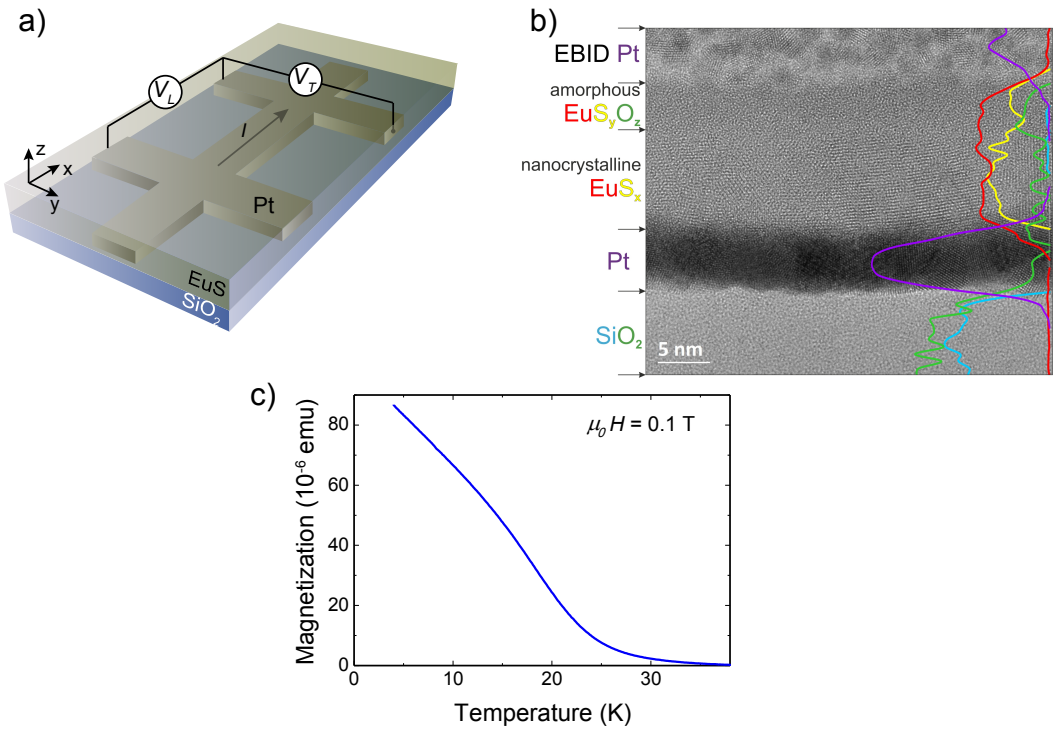

Figure 6.1: **Sketch of the device, transmission electron microscopy image of the EuS/Pt heterostructure and EuS magnetization.** (a) Schematic illustration of the device geometry. (b) TEM image with the spatial EDX data analysis. The colors corresponds to blue:Si, green:O, purple:Pt, red:Eu, and yellow:S. (c) Temperature dependence of the EuS magnetization measured by SQUID.

low temperature, which can be related to the two magnetic layers present in the stack. A similar $M(T)$ behavior has been reported in an evaporated 10-nm-thick EuS film [182].

6.3.2 Angular-dependent magnetoresistance

Figures 6.2(c) and 6.2(d) are shown the ADMR measurements at 2.5 K with the magnetic field ($H = 0.1$ T and 2 T, respectively) rotating in the three main planes defined in the sketches (Pt resistivity $\rho \sim 47$ $\mu\Omega$·cm). At $H = 0.1$ T, we can clearly say that only in $\alpha-$plane the magnetization is saturated, confirming the soft magnetic behavior in plane, the longitudinal (transverse) ADMR shows the typical $cos^2\alpha$ ($cos\alpha \cdot sin\alpha$) modulation related to the SMR geometry [75, 76, 79, 164]. In order to saturate out-of-plane we applied $H = 2$ T [Fig. 6.2(b)]. In this case, the cos^2 modulation in $\alpha-$ and $\beta-$plane is clear with similar amplitude ($\Delta\rho_1/\rho$) in the longitudinal ADMR, and $cos\alpha \cdot sin\alpha$ in the transverse ADMR.

In the case of $\gamma-$plane, no modulation is expected. Nonetheless, there is a small modulation not related to SMR neither to anisotropy magnetoresistance

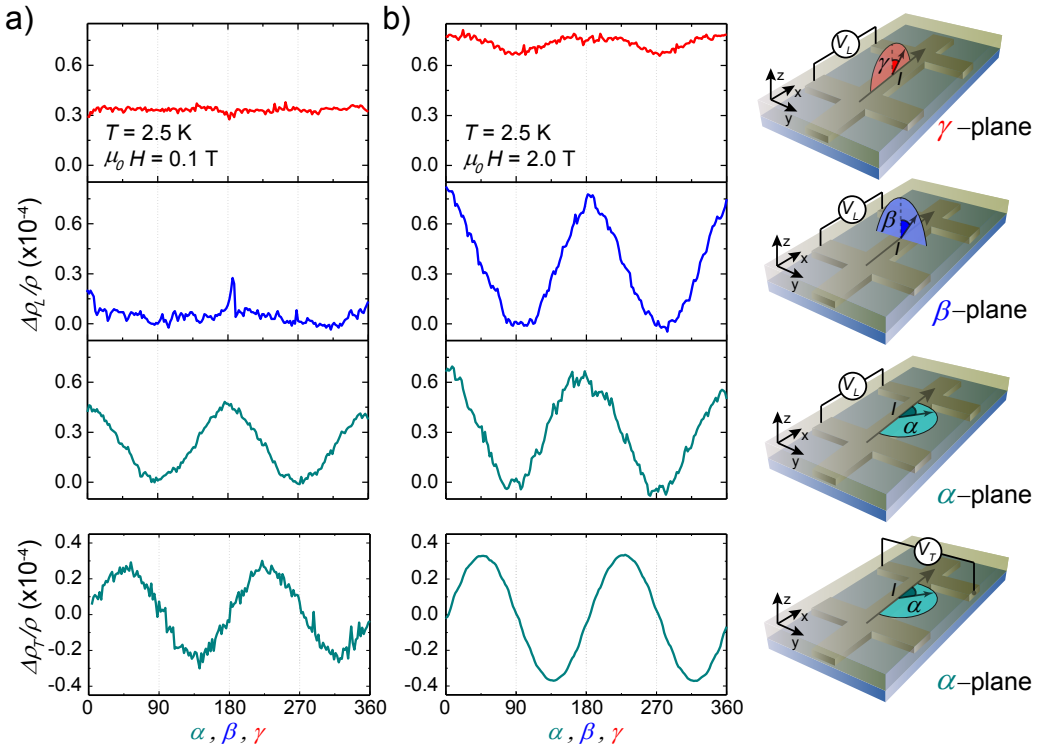

Figure 6.2: **Angular-dependent magnetoresistance measurements in Pt/EuS.** (a) Normalized longitudinal ($\Delta\rho_L/\rho$) and transverse ($\Delta\rho_T/\rho$) ADMR at 2.5 K along the three relevant $H-$rotation planes (α,β,γ), see sketches on the right side, for different applied magnetic fields: (a) $\mu_0 H = 0.1$ T and (b) $\mu_0 H = 2$ T.

(AMR) [183, 184] due to magnetic proximity effect (MPE) in Pt [67, 69, 70, 185–187]. This modulation is likely due to weak antilocalization (WAL) that appears in Pt at low temperatures and large H, when H is applied out-of-plane [78], see section 1.5.4.

6.3.3 Field-dependent magnetoresistance and Hall measurements

This is confirmed by the longitudinal FDMR measurements shown in Fig. 6.3(a) in the three main axes (see sketch in the figure), where the curve in H_z-direction should be the same that the one in H_x due to the spin symmetry by SMR: in both cases $\boldsymbol{\mu_S}$ is perpendicular to the EuS magnetization, leading to a high resistance state. The fact that, at large magnetic fields, the curve in H_z is larger than H_x is a clear feature of the WAL in Pt. It is also observed an increased in the resistance H_y-direction with H, this feature is also related to WAL (Supplementary information in Ref. [54]). At low magnetic fields ($\mu_0 H$ < 1.5 T), a clear gap appears between H_x, H_z curves and H_z curve with peaks

around zero field. These peaks are better seen in the FDMR at lower magnetic fields shown in Fig. 6.3(b), which correspond to the reversal magnetization of EuS (few mT in plane). Figure 6.3(c) is the transverse FDMR in plane, with the magnetic field applied in $\alpha = 45^o$ and $\alpha = 135^o$ (corresponding to the maximum and minimum values), confirming that the magnetization reversal occurs around ~ 5 mT. In the case of H_z, the magnetization reversal occurs at larger H (~ 1.5 T) because the hard axis the EuS film is out-of-plane. In addition, we performed Hall measurements, see Fig. 6.3(d). At large H, we observe linear dependence with H that corresponds to the OHE. In the case of low H, as in the previous chapter with the Pt/GGG, there is a clear non-linearity which follows the out-of-plane magnetization reversal of EuS. Therefore, in Pt/EuS, we also measure the AHE-like term expected from SMR, which gives us the $\Delta\rho_2/\rho$ amplitude from the intercept of the linear fittings at large (positive and negative) magnetic fields 6.3(d).

We have already discussed that $\Delta\rho_1/\rho$ and $\Delta\rho_2/\rho$ are the SMR amplitudes and depend on the $G_{\uparrow\downarrow} = (G_r + iG_i)$. In the original SMR theory, the $G_{\uparrow\downarrow}$ terms are considered temperature and field independent. In the case of a ferrimagnetic insulator, with compensated magnetic moments, G_i is at least one order of magnitude smaller compared to the G_r, giving rise to a very small AHE-like effect in this kind of materials, such as YIG [48,79,82]. In these cases, it is usually difficult to measure in the Hall configuration due to the huge Hall effect background compared to the contribution of the AHE-like amplitude (**Chapter 3**). Nonetheless, in the EuS we can see a clear $\Delta\rho_2/\rho$ signal in Fig. 6.3(d). Figure 6.4(a) shows the temperature dependence of $\Delta\rho_1/\rho$ and $\Delta\rho_2/\rho$; we find that $\Delta\rho_2/\rho$ is larger than of $\Delta\rho_1/\rho$. In both cases, the signal disappears close to the T_c of our EuS film.

6.3.4 Temperature dependence of spin conductances

Next, we investigate the evolution of the different spin conductance terms with the temperature. For that purpose, we use again the microscopic theory for SMR explained in section 1.5.5. We perform two kind of fittings to our experimental data, by using two different models for the ferromagnetism of EuS, random phase approximation (RPA) and Weiss field theory (WFT). The former fits the EuS magnetization to Curie-Weiss law in order to extract the spin expectation $\langle\widehat{S}_\parallel\rangle$, while the later uses experimental magnetization as $\langle\widehat{S}_\parallel\rangle$ and, from $\langle\widehat{S}_\parallel\rangle$ the spin-spin correlation function$\langle\widehat{S}^2_\parallel\rangle$ can be calculated [84]. For the fitting we need the temperature dependence of the two SMR amplitudes [Fig. 6.4(a)] and the values of λ_s ($\sim$1.3 nm) and θ_{SH} ($\sim$0.19) extracted from the Pt resistivity at each temperature [42]. Figure 6.4(a) shows the fitting curves for the SMR amplitudes $\Delta\rho_1/\rho$ (purple line) and $\Delta\rho_2/\rho$ (blue line) as a function of T, with J_{sf}, n^{2D}_{imp}, J_1

and J_2 being the fitting parameters. J_1 and J_2 are the exchange couplings for first neighbors (12 first neighbors) and second neighbors (6 second neighbors), respectively. The simulation reproduces, with quite accuracy, the obtained experimental data for both RPA and WFT model. The fitting parameters used for the simulations are $n^{2D}_{imp,RPA} = 0.12/a^2$ with a the EuS lattice parameter ($n^{2D}_{imp,WFT}$ $=0.14/a^2$) and $J_{sf,RPA} = 19.28$ meV ($J_{sf,WFT} = 16.84$ meV), which is the ferromagnetic exchange interaction between $1s$ electrons in Pt and $4f$ electrons in EuS for RPA (WFT) fitting. EuS exchange constants extracted from the fitting $J_1 = 0.221k_B$ (ferromagnetic exchange interaction of $4f$ electrons in EuS) and $J_2 = -0.1k_B$ (antiferromagnetic exchange interaction with the second neighbors) are in very good agreement with previous theoretical reports [51] and experimental values extracted by neutron scattering [188, 189]. Figure 6.4(a) shows that both models reproduce quite accurately the experimental data and that the best fit-

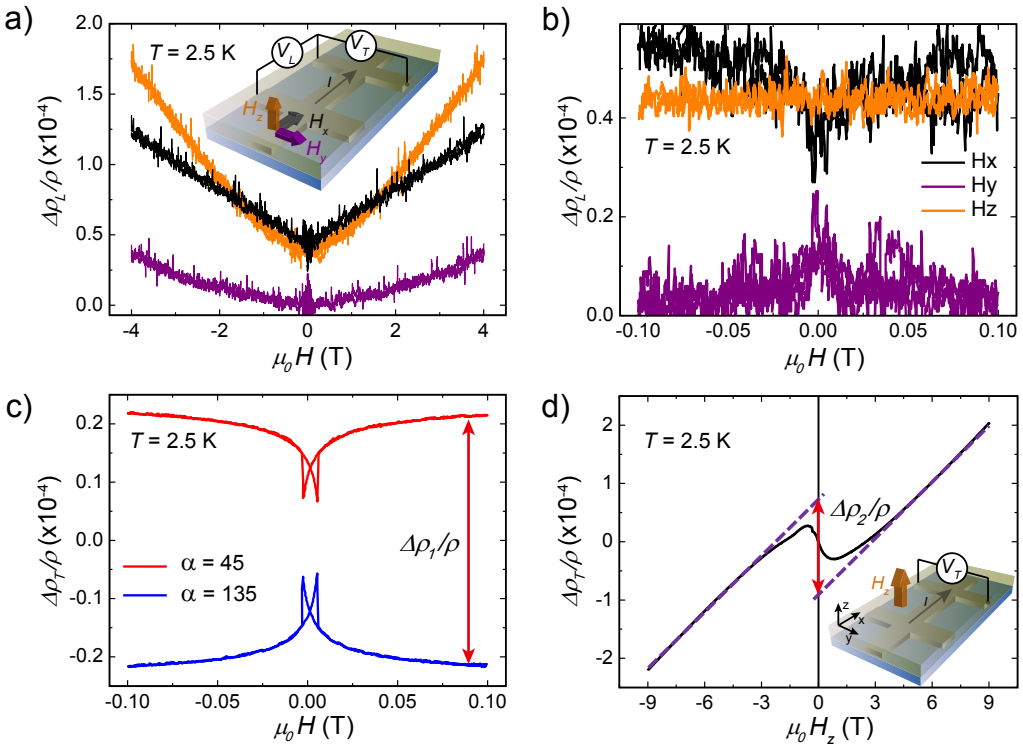

Figure 6.3: **Field-dependent magnetoresistance measurements in Pt/EuS.** (a) Normalized longitudinal FDMR measurements performed along the three main axes at 2.5 K in a range of magnetic fields between 4 T and – 4 T (see sketch for the definition of the axes, color code of the magnetic field direction, and measurement configuration). (b) Zoom of the area at low magnetic field where the magnetization reversal occurs. (c) Normalized transverse FDMR measurements performed in $\alpha-$plane in $\alpha = 45^o$ and $\alpha = 135^o$. The red arrow shows the amplitude corresponding to $\Delta\rho_1/\rho$. (d) Hall configuration measurements. Dash purple lines correspond to the linear fit performed at large magnetic fields. The red arrow shows the amplitude corresponding to $\Delta\rho_2/\rho$.

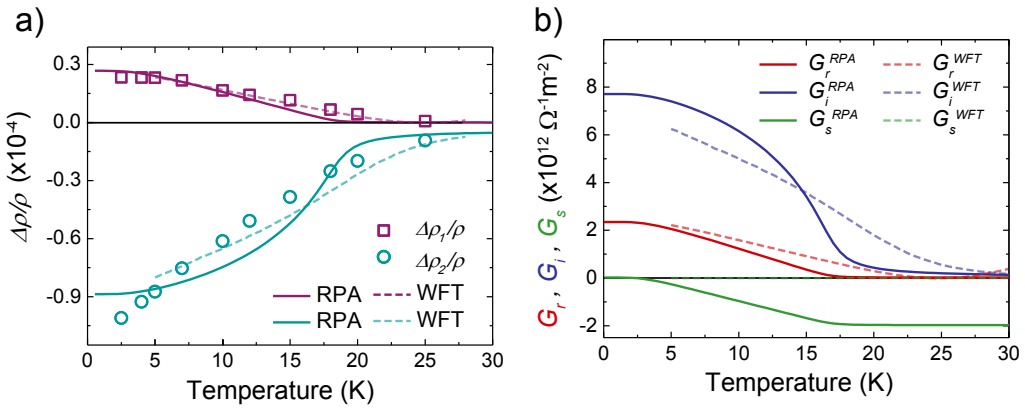

Figure 6.4: **Temperature dependence of the spin Hall magnetoresistance amplitudes and the spin conductances.** (a) Temperature dependence of the normalized SMR amplitudes $\Delta\rho_1/\rho$ (extracted from the ADMR in $\alpha-$plane at $H = 0.1$ T) and $\Delta\rho_2/\rho$ (extracted from from the AHE-like contribution in the Hall configuration method. The open dots represent the experimental data and the solid (dashed) lines are thebest fits obtained with the RPA (WFT) model and the microscopic theory [84]. (b) Temperature dependence of the real part (G_r), imaginary part (G_i) of the spin-mixing conductance and the spin-sink conductance (G_s). The solid (dashed) lines are calculated values from the best fits obtained fittings with RPA (WFT) model.

ting parameters are similar for both cases, which strengthen the reliability of the obtained values. The obtained J_{sf} here is much smaller than other experimental accessible values, for instance $J_{sd} = 350$ meV for Co-Cu, but it is similar to the one extracted for Pt/GGG in previous chapter. n_{imp}^{2D} values depend on the slicing of the lattice surface and the quality of HM/FMI surface. The n_{imp}^{2D} value obtained here matches well with previous **Chapter 5**.

From the same fitting parameters obtained from Fig. 6.4(a), we use Eqs. 1.28-1.30 to calculate the temperature dependence for G_r, G_i, and G_s, see Fig. 6.4(b). At low temperature, when the EuS magnetization saturates, G_r and G_i are maximum whereas G_s becomes zero due to the reduction of the spin-flip scattering. At higher temperatures and close to T_c, with the absence of net magnetization due to the randomized spins ($\langle\widehat{S}_{\parallel}\rangle \to 0$), G_r and G_i vanish to zero because of the isotropic relaxation time (see Eqs. 1.31), whereas G_s becomes maximum. This observed behavior is equivalent (or similar) to the magnetic field dependence of the spin conductances in Pt/GGG described in **Chapter 5**. The key point of the temperature dependence of the spin conductivities is that we experimentally demonstrate for the first time that in FMI such as EuS, G_i is larger than G_r, up to 4 times larger at very low temperatures ($T = 2.5$ K), as it was predicted in Ref. [58] for europium chalcogenides. The small differences between the model used and the experimental data can be due to small defects at the interface and the higher T_c (for the case of RPA fits) that our film shows (Fig. 6.1(b)), and

that the mean field theory applied does not consider. According to our results, we can confirm that in Pt/EuS the field-like torque plays an important role in this system and it is not negligible as it is in other MIs [48, 79, 82], where there is a compensation of the magnetic moments.

From the value obtained for G_i from the SMR measurements we can calculate the effective interfacial exchange h_{ex} that is related to G_i *via* [84]: $h_{ex} = G_i/\pi G_0 \nu_F b$, where G_0 is the quantum of conductance, ν_F is the density of states of the HM at the Fermi level and b is a length of the order of the mean free path (l). By assuming $\nu_F \approx 4.6 \times 10^{28}$ m^{-3}eV^{-3} and $l \approx 10^{-9}$ m and taking the value of G_i from SMR measurements, $G_i \approx 7.65 \times 10^{12}$ Ω^{-1}m^{-2}, we obtain $h_{ex} = 10^{-3}$ eV. If we assume this value of h_{ex} for an EuS/Al bilayer then the effective spin-splitting field induced in Al is given by $h_{eff} = h_{ex} b/d_{Al}$, where d_{Al} is the thickness of the Al layer. For $d_{Al} \approx 2 - 10$ nm [170, 179], we calculate $h_{eff} \approx 100 - 500$ μeV, whereas the superconducting gap for Al at low temperatures is approximately $\Delta \approx 200$ μeV. In order to observe coexistance between superconductivity and the spin-splitting field, $h_{eff} < 0.7\Delta$ and hence for the observation of a clear spin-split BCS (Bardeen–Cooper–Schrieffer) density of states, special care should be taken in the fabrication of EuS/Al bilayers.

6.4 Conclusions

In summary, we observe SMR in a Pt/EuS bilayer, where EuS is a pure ferromagnetic insulator below 30 K. The SMR is observed by ADMR and FDMR measurements, in which the magnetization reversal of EuS is observed. Furthermore, we also measure the AHE-like contribution of the SMR, driven by a large imaginary part of the spin-mixing conductance. We can extract microscopic parameters such as the exchange interaction between the $1s$ electrons of Pt and the $4f$ efectrons of Eu ($J_{sf} \sim 17-19$ meV). We study the temperature dependence of the spin conductances of the Pt/EuS interface, showing for the first time experimentally a larger field-like torque (G_i) than spin-transfer torque (G_r) in a HM/MI interface. The effective exchange field associated to G_i is expected to be ~ 1 meV. Therefore, SMR measurements offer a simple way to quantify effective fields which are of interest in different areas, such as superconducting applications.

6

6

Results. Part II

Magnon Spin Transport in Magnetic Insulators

6

Chapter 7

Differences in the magnon diffusion length for electrically and thermally driven magnon currents in $Y_3Fe_5O_{12}$

Magnon currents can be excited both electrically and thermally, even in magnetic insulators, by applying charge currents in an adjacent metal layer. Earlier reports in thin YIG films suggested that the diffusion length of magnons is independent on the excitation method, but different values were obtained in thicker films. In this chapter, we study the magnon diffusion length for electrically and thermally excited magnons in a 2-μm-thick YIG film as a function of temperature and magnetic field. Our results evidence that the diffusion length depends on the generation mechanism. Moreover, we show that the damping of the thermally driven magnons with magnetic field is weaker than for those excited electrically. Finally, we demonstrate that the magnon diffusion length for thermally excited magnons is independent of the YIG thickness and material growth conditions, confirming that this quantity is an intrinsic parameter of YIG.*

*Published as: Juan M. Gomez-Perez, Saül Vélez, Luis E. Hueso and Fèlix Casanova, "Difference of the magnon diffusion length for electrically and thermally driven magnon currents in $Y_3Fe_5O_{12}$", arXiv:1912.00490 (2019)

7.1 Introduction

The generation of magnon spin currents in MIs can be achieved by exciting the ferromagnetic resonance of the MI [19,85] (low frequency coherent magnons), by inducing a thermal gradient [86] (high frequency incoherent magnons), or electrically by making use of the SHE of HM such as Pt [20] (high-frequency incoherent magnons), whereas, in most of the cases, have been detected ellectrically by employing the ISHE. In the original work of Cornelissen *et al.* [20], magnons were electrically and thermally excited in YIG, and electrically detected up to tens of μm apart at room temperature, by employing a non-local configuration in which Pt strips acted as injectors and detectors of the magnons currents (see section 1.5.6). Many studies on incoherent magnon spin transport have followed [19, 20, 52, 53, 56, 82, 86, 90, 91, 91–93, 96, 97, 99], in which YIG played the central role because of its soft ferrimagnetism, negligible magnetic anisotropy, and low Gilbert damping [19, 20, 46, 52, 53, 56, 86, 91, 93, 96, 97, 99], although magnon spin transport has also been demonstrated in other MIs [90, 101, 190].

The key parameter that defines the characteristic length to which magnons propagate is the magnon diffusion length (λ_m); see section 1.5.6. Its value has been studies in YIG as a function of the temperature [56, 90, 97, 99], magnetic field [100], thermal gradient [86], and thickness [96]. Earlier report suggested that λ_m is the same regardless of the mechanism by which the magnons are excited (by thermal gradients or by torques employing the SHE) [56], but more recent works showed that those values might be different [90, 96]. It is thus not clear whether the thickness of the MI layer might play a role on the value of λ_m or whether the nature of the excited magnons, and thus their diffusivity, might be different due to the different energy scales involved in the two types of generation methods.

In this chapter, we report a systematic study of the magnon diffusion length in a 2-μm-thick YIG for ellectrically and thermally excited magnons at various magnetic fields in a wide range of temperatures. Our results evidence that the magnons diffuse differently depending on the way they are created, supporting the idea that magnons of different energies, which exhibit different characteristic diffusive length scales, are generated. Furthermore, we demonstrate that the size and temperature dependence of λ_m of the thermally excited magnons are the same regardless of the YIG thickness and growth method. This result shows the robustness of thermally induced magnon transport to extract the magnon transport properties of YIG and, by extension, of MIs.

7.2 Experimental details

The devices were fabricated on top of 2-μm-thick YIG films provided by Innovent e.V. (Jena, Germany). YIG was grown by liquid phase epitaxy (LPE) in a (111) GGG substrate. In a first sample (sample 1), a 5-nm-thick Pt layer was magnetron-sputtered *ex situ* (80 W; 3 mtorr of Ar) on top of YIG, and Pt strips (width $w = 450$ nm, length $L = 80$ μm) were patterned by negative e-beam lithography and Ar-ion milling (see section 2.1) with different edge-to-edge distances ($d = 1{-}20$ μm). In a second sample (sample 2), devices with distances ranging from 8.5 μm to 125 μm were fabricated. In this case, for shorter distance devices ($d = 8.5{-}40$ μm), the Pt strip dimensions are the same as for sample 1, whereas for longer distances ($d = 50{-}125$ μm), the dimensions are $L = 650$ μm and $w = 2.7$ μm and the measured voltage is normalized accordingly [20]. A SEM image of one of the devices is shown in Fig. 7.1(a). Magnetotransport measurements were carried out as explained in section 2.2.1, in order to measure the electrical (V_{NL}^{e}) and thermal (V_{NL}^{th}) non-local voltages.

7.3 Results and discussion

7.3.1 Angular dependence of the non-local signal for electrically and thermally excited magnons.

We investigate the magnon spin transport for both electrically and thermally induced magnon currents in YIG by employing the non-local configuration shown in Fig. 7.1(a). This device scheme allows exploiting the large SHE in Pt [42,87–89] to electrically excite and detect magnon currents in YIG. By applying a charge current along a Pt strip, a spin accumulation is induced at the Pt side of the Pt/YIG interface due to the SHE [which is in the plane of the film and perpendicular to the current, see vector notation in Fig. 7.1(b)]. When the YIG magnetization and spin polarization of the spin accumulation in Pt are parallel (antiparallel), a magnon is annihilated (created) due to exchange interaction between the Pt electron spins and the YIG magnetic moments, leading to a magnon imbalance that modifies the magnon chemical potential close to the interface [55]. This gives rise to a diffusion of magnons (magnon spin current) that can propagate for several microns along YIG [20,52,56,90–94]. By the reciprocal process, a second Pt strip can detect the magnon imbalance, as the induced spin accumulation in Pt (due to the magnon-to-spin conversion at the interface) is finally converted to a voltage by the ISHE. Given that the electrical excitation of magnon currents is a linear process (for weak and moderate excitation amplitudes) [20, 191], the

detected non-local voltage V_{NL}^{e} (see section 7.2 for details) is proportional to the applied charge current. This is indeed confirmed in our devices for all experimen-

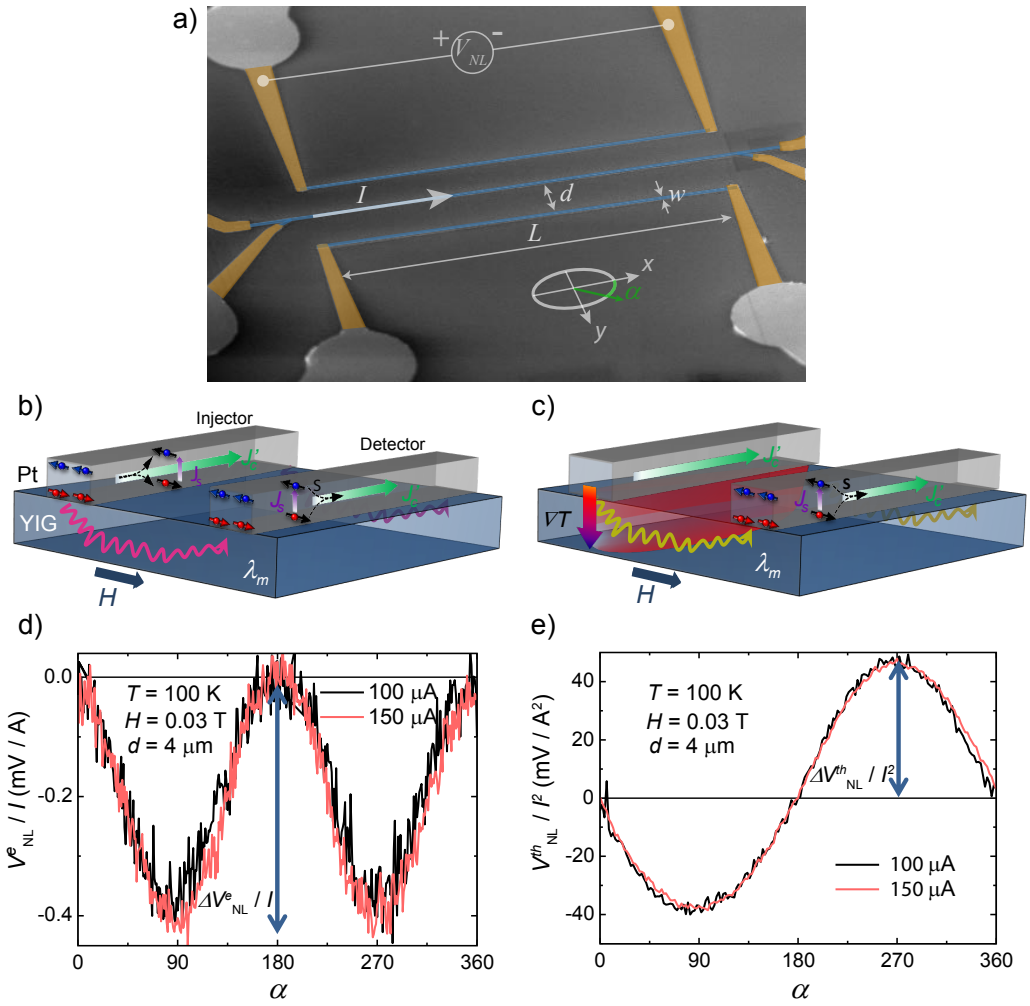

Figure 7.1: **Device geometry, measurement configuration and angular-dependent non-local signal for electrically and thermally excited magnons.** (a) SEM image of a non-local device used in this work ($d = 6$ μm). The measurement configuration and the geometrical parameters are indicated. (b,c) Schematic representation of the creation, transport and detection of magnon currents in the non-local devices by means of (b) electrical excitation and (c) thermal excitation. (d,e) Representative angular-dependent non-local signals detected for (d) electrically and (e) thermally excited magnons using the measurement configuration shown in (a). The magnetic field applied is $H = 0.03$ T, which is sufficient to saturate the magnetization of our YIG films. The measurement temperature is 100 K and the device corresponds to sample 1. The non-local signals are presented as the non-local voltage normalized to the applied current in (d) and to the square of the applied current in (e), showing that V_{NL}^{e} and V_{NL}^{th} are linear and quadratically dependent on the injected current, respectively.

tal conditions reported in this work. As an example, we show in Fig. 7.1(d) the non-local V_{NL}^{e} signal measured in a representative device at two different currents while rotating the in-plane magnetic field. The two curves nicely overlap once the signal is normalized by the injected current. Moreover, note that the angular dependence of the non-local voltage shows the expected sin^2 dependence, which is due to the symmetry of the SHE and the ISHE at the injector and detector Pt stripes, respectively, and their relative orientation with the magnetization of the YIG layer [20, 52, 53].

On the other hand, magnons can also be thermally excited. In ferromagnetic materials, a thermal gradient drives a magnon spin current parallel to the induced heating flow due to the spin Seebeck effect [46]. Therefore, by making use of the Joule dissipation in a Pt strip, a thermal gradient can be generated in the YIG film beneath, resulting in a diffusive magnon current that can be non-locally detected by employing the ISHE of a second Pt strip (Fig. 7.1(c)) [20, 86, 91, 96, 97, 99]. In this non-local spin Seebeck configuration, the voltage V_{NL}^{th} (see section 7.2 for details) scales quadratically with the applied charge current. This is confirmed in our devices at temperatures above 2.5 K and for the whole range of currents employed in this work. This dependence is demonstrated in Fig. 7.1(e), where we show the angular dependence of the non-local voltage V_{NL}^{th} measured at two different currents in a representative device, which coincide once we normalize the curves to the square of the injected current. At 2.5 K, and for low current densities, however, V_{NL}^{th} does not scale with the square of the current (see section 7.6.1), which is consistent with previous reports [100]. The angular dependence of the thermally excited magnon currents shows a sin dependence with α [see Figs. 7.1(a) and 7.1(e)], because in this case only the ISHE symmetry of the detector plays a role [20, 52].

From these two types of non-local signals, and by measuring their amplitude in devices having different distances d between the injector and detector strips, we can extract the magnon diffusion length of our YIG films.

7.3.2 Temperature and magnetic field dependence of the non-local signals

We now investigate the temperature and magnetic field dependence of the magnon transport for both thermally and electrically excited magnon currents. The temperature dependence of the amplitude of the non-local signal, measured at $H = 0.03$ T and for different distances between the Pt electrodes, is plotted in Figs. 7.2(a) (for electrically excited magnons) and 7.2(b) (for thermally excited magnons).

The non-local signal for electrically excited magnons [Fig. 7.2(a)] vanishes when approaching zero temperature and, for the longest distances, can only be extracted reliably above 50 K (see section 7.6.2). The signal increases with increasing temperature, having a maximum at approximately 100 K. This behavior, which is in agreement with Refs. [52, 56], can be understood by taking into account that the magnon population is strictly zero at zero temperature and increases with temperature, leading to a more efficient generation. However, above 100 K, the non-local signal decreases up to 300 K. This temperature dependence is different than the ones reported in Refs. [52,56], but closely resembles the temperature dependence of the SMR measured in our Pt/YIG bilayers (see section 7.6.2). This correlation is expected as the amplitude of both the SMR and the non-local signal have the same dependence with the spin Hall efficiency at the Pt/YIG interface [55]. Besides, as expected, the non-local signal decreases when the distance between the Pt electrodes increases.

In the case of thermally excited magnons [Fig. 7.2(b)], the largest non-local spin Seebeck signal is found at the lowest temperature (2.5 K). The signal is larger than the one measured for electrically-driven magnon currents and, for this reason, we are able to detect non-local signals for longer distances (~ 20 μm in this sample, and up to 125 μm in the second sample with longer distances, see section 7.6.3). The amplitude sharply decreases between 2.5 K and 10 K, followed by a plateau between 10 and 50 K, and finally decreases monotonically with increasing temperature. The low temperature behavior ($T < 10$ K) could be related to the strong variation of the thermal gradient generated at the Pt injector, since many of the parameters defining the thermal gradient (such as thermal conductivity and specific heat of YIG) have a strong temperature dependence at this low temperature regime [192]. Indeed, a puzzling behavior of the non-local spin Seebeck effect signal have been reported at this temperature range, whose origin remains unclear [56,99]. Moreover, and in agreement with what is observed for electrically-driven magnon currents, the signal gets smaller when increasing the injector-detector distance. Finally, a sign change of the non-local spin Seebeck effect is expected for injector-detector distances that are below certain value (which is on the order of the YIG thickness) [91,96,193]. In our case, however, we do not observe this behavior as all measurements are taken above the distance at which the sign change occurs.

The magnetic field dependence of the non-local signal is plotted in Fig. 7.2(c) (for electrically excited magnons) and Fig. 7.2(d) (for thermally excited magnons) for a distance $d = 4$ μm between the Pt electrodes and different temperatures. The non-local signal for electrically excited magnons [Fig. 7.2(c)] decreases monotonously with magnetic field, being strongly reduced at 9 T. In contrast, the signal for thermally excited magnons [Fig. 7.2(d)] shows a shallow maximum

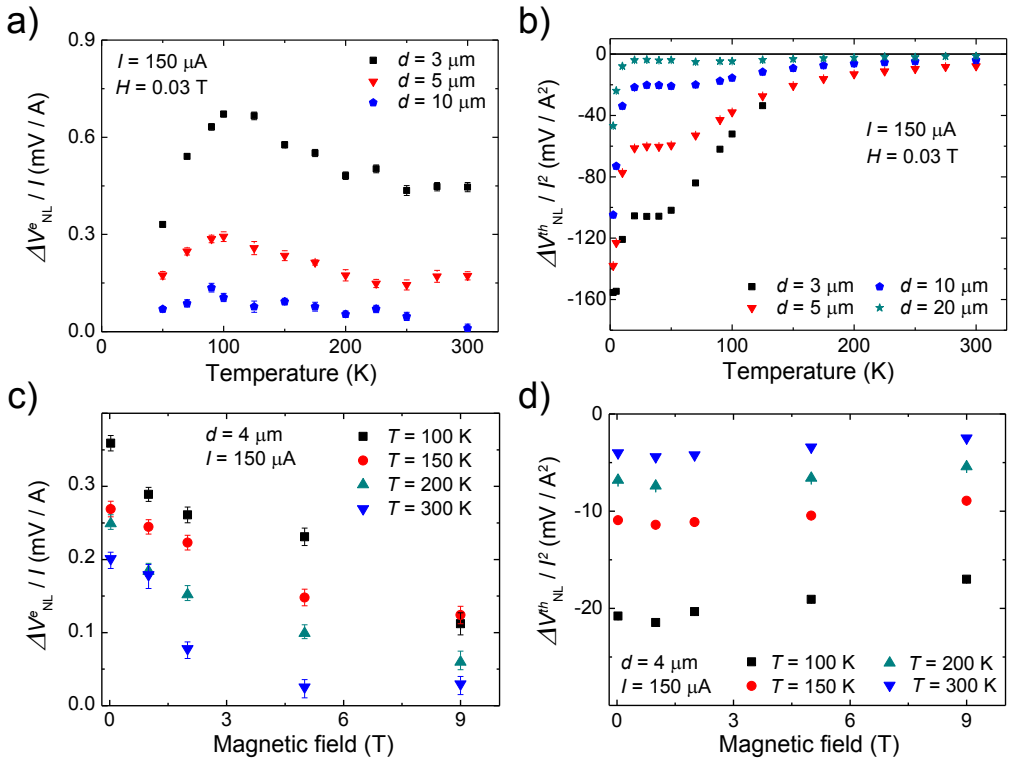

Figure 7.2: **Temperature dependence and field dependence of the non-local signals for electrically and thermally excited magnons.** (a-b) Temperature dependence of the non-local voltage amplitude for (a) electrically and (b) thermally excited magnons at 0.03 T, and for different distances between the injector and detector Pt strips. (c-d) Magnetic field dependence of the non-local voltage amplitude measured at a distance of 4 μm and different temperatures for (c) electrically and (d) thermally excited magnon currents. The non-local signal is normalized to the charge current applied (150 μA) in (a) and (c), and to the square of the current in (b) and (d). All data correspond to sample 1.

at $\sim$ 1 T, and slowly decreases to 9 T. These behaviors are similar to the ones reported in Ref. [93].

7.3.3 Temperature and magnetic field dependence of the magnon diffusion length

From the data reported in the previous section, we can now extract the magnon diffusion length at different magnetic fields and temperatures, which is the relevant parameter that describes the magnon transport behavior. As an example, we show in Figs. 7.3(a) and 7.3(b) the non-local signals as a function of the distance d between the Pt electrodes for a particular temperature (150 K) and selected magnetic fields (0.03, 5 and 9 T). We identify two distinctive

regions known as the diffusion regime (light purple region) and the exponential regime (light brown region), see section 1.5.6 for details. In the diffusion regime, which corresponds to $d \lesssim \lambda_m$, the non-equilibrium magnon accumulation diffuses away from the injector into the YIG with a geometrical decay [55, 82, 90]. Further away, at $d \gtrsim \lambda_m$, magnons relax showing an exponential decay for the two type of excited magnons [20, 96, 99]. Therefore, in order to determine λ_m, a linear fitting of the natural logarithm of the non-local voltage amplitude is performed in the exponential regime, as shown in Figs. 7.3(a) and 7.3(b) (red solid lines). In the case of the thermally excited magnons, the linear fittings should be carried out for distances shorter than 3−5 times λ_m to avoid entering the $1/d^2-$regime, where the signal is dominated by the temperature gradient induced (by geometric thermal diffusion) at the YIG/GGG interface underneath the Pt detector [93]. From these fittings, we extracted the magnon diffusion length for both electrically (λ_m^e) and thermally excited magnons (λ_m^{th}) at different temperatures and applied magnetic fields. The results are presented in Figs. 7.3(c)−7.3(f).

At any magnetic field applied, λ_m^e shows a constant or slightly decreasing behavior with increasing temperature [Fig. 7.3(c)]. As discussed above, we cannot estimate λ_m^e below 50 K because of the small signal-to-noise ratio. λ_m^e decreases monotonously with increasing the magnetic field [Fig. 7.3(e)], in line with the strong decay reported in Ref. [93] for electrically excited magnons at 300 K. Both the temperature and field dependences are completely different for λ_m^{th} [Fig. 7.3(d)]. At low magnetic fields (0.03 T), λ_m^{th} is maximum at the lowest measured temperature (2.5 K) and decreases up to 30 K. In this temperature range, the increase of the magnetic field reduces the value of λ_m^{th}, although the same trend with temperature is kept in the whole range of magnetic fields explored (up to 9 T). For temperatures above 30 K, however, two different temperature dependences for λ_m^{th} are identified depending on the strength of the magnetic field: i) at low magnetic fields (0.03 T), λ_m^{th} slightly increases with temperature, in contrast with the behavior of λ_m^e for the same magnetic field and temperature range; ii) at high magnetic field (5 T and 9 T), λ_m^{th} becomes fairly temperature independent. It is also worth mentioning that the decay of λ_m^{th} with increasing magnetic field is different at different temperatures, but saturates above $\sim$ 2 T in all cases except at 2.5 K [see Fig. 7.3(f)], in agreement with the case at 300 K shown in Ref. [93]. The origin of the differences between the magnon diffusion lengths will be discussed in the following section.

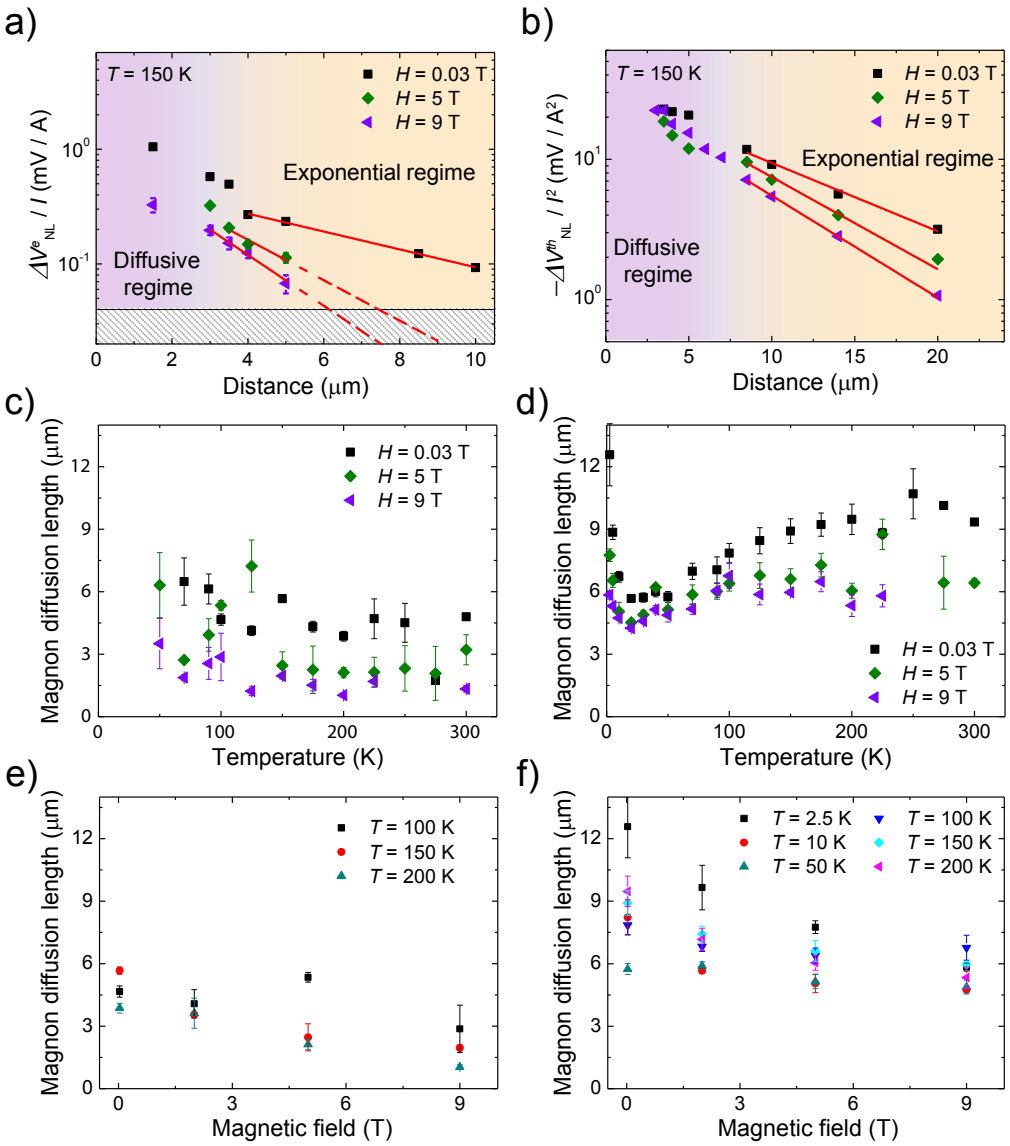

Figure 7.3: **Temperature dependence and magnetic field dependence of the magnon diffusion length.** (a-b) Non-local voltage amplitude for (a) electrically and (b) thermally excited magnons as a function of injector-detector distance and for different magnetic fields. The diffusive and exponential magnon transport regimes, which are indicated with different colors, are identified from the different decay of the signal with increasing distance. The red lines are fits in the exponential regime to extract the magnon diffusion length at the corresponding magnetic field applied. The dashed region at the bottom of (a) indicates the noise threshold of the measurement setup. (c-d) Temperature dependence of the magnon diffusion length for (c) electrically (λ_m^e) and (d) thermally (λ_m^{th}) excited magnons at different magnetic fields. (e-f) Magnetic field dependence of (e) λ_m^e and (f) λ_m^{th} at different temperatures. All data correspond to sample 1.

7.3.4 Comparison between electrical and thermal magnon diffusion length

In the following, we compare the temperature dependence of λ_m^e and λ_m^{th} for low (0.03 T) and high (9 T) magnetic fields applied (see Fig. 7.4).

Low magnetic field regime. Let us start with the case of a low magnetic field applied (0.03 T). As discussed before, the relatively low signal generated for electrically excited magnons prevented us to measure λ_m^e at low temperatures. However, in the temperature regime from $\sim$ 70 K to $\sim$ 100 K, it seems that both λ_m^e and λ_m^{th} converge to $\sim$ 6 μm. Increasing the temperature, however, results in a splitting of both characteristic lengths, with λ_m^{th} increasing while λ_m^e slightly decreasing, reaching $\sim$ 9.3 μm and $\sim$ 4.8 μm, respectively, at room temperature. This behavior is in stark contrast to previous results reported in 0.2-μm-thick YIG films, where both magnon diffusion lengths coincide [20, 93]. However, as in our 2-μm-thick YIG, recent results in thicker YIG films indicate that the magnon diffusion lengths of electrically and thermally excited magnons might be different [96, 99], suggesting that the thickness of the YIG layer might have an influence in the magnon diffusion length.

In order to rule out the possibility of non-local thermal effects influencing the signals, which would lead to a misestimation of λ_m^{th}, we measured a second sample (sample 2) with devices with longer injector-detector distances. As discussed in section 7.6.3, we can clearly distinguish the exponential regime, from which λ_m^{th} can be extracted reliably, from the $1/d^2-$regime, which is dominated by the thermal gradient generated at the GGG/YIG interface underneath the detector [99]. By fitting the data to the entire exponential regime (which ranges up to $\sim$40 μm), we obtain λ_m^{th} values that are in good agreement with the values extracted from sample 1 (see Fig. 7.5). We thus conclude that both λ_m^{th} and λ_m^e are properly evaluated for the case of a low magnetic field applied and, more importantly, they are different in the temperature range 100$-$300 K. The captured trend for $\lambda_m^e(T)$ suggests that it may converge with $\lambda_m^{th}(T)$ at lower temperatures (Fig. 7.4, solid symbols). However, the relatively small non-local signal measured for electrically excited magnons at low temperatures (note that both the reduction of the temperature, see Fig. 7.2(a), as well as the thickness of the YIG film contribute to a reduction of the signal [20, 56, 93, 97]) impede us to evaluate their diffusion length in this regime and, consequently, prevented us to extract solid conclusions about the possible convergence of both magnon diffusion lengths at low temperatures.

The large difference observed between the magnon diffusion length for electrically and thermally excited magnons (which approaches to a factor of two at

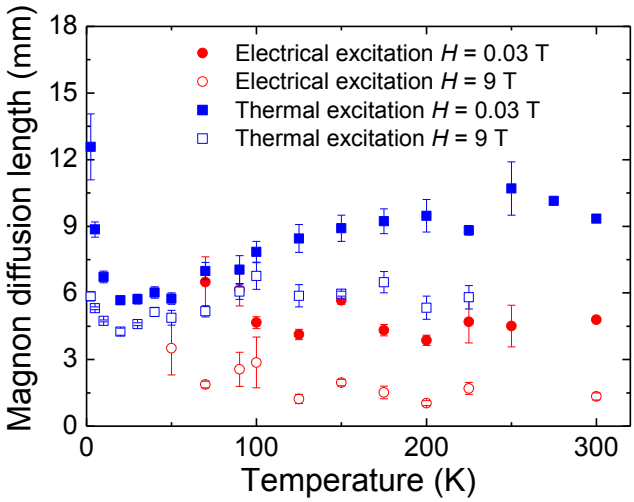

Figure 7.4: **Temperature dependence of the electrical and thermal magnon diffusion length.** Temperature dependence of the magnon diffusion length at 0.03 T (solid symbols) and 9 T (open symbols) for electrically (red circles) and thermally (blue squares) excited magnons. Data corresponding to sample 1.

room temperature) evidences that the magnons generated at the YIG/Pt-injector interface diffuse and relax differently depending on the way they are excited. First reports in thinner films [20,56,93] (0.2 μm, whereas here we study a 2.0-μm-thick YIG), however, suggested that both methods result in the creation and propagation of equivalent magnon populations. From a theoretical perspective, given that it was possible to model the magnon transport experiments by employing a single relaxation parameter, it was believed that the magnon transport is dominated by the diffusion of thermal magnons [20,55]. More recent reports, however, showed hints that the magnon diffusion length of electrically excited magnons may differ from those excited thermally in thick films [96, 99], with λ_m^e values found that are surprisingly similar to the one extracted here ($\lambda_m^e \sim 6$ μm at room temperature [96]). The existence of such discrepancy, however, was not discussed.

In order to understand the origin of the discrepancy between λ_m^e and λ_m^{th}, we note that studies of the longitudinal spin Seebeck effect in YIG/Pt showed that sub-thermal magnons, i.e., magnons that have energies below k_BT, interact more strongly with the electrons in Pt [194]. The critical temperature at which the sub-thermal magnons become noticeable in the experiment was estimated to be $T_c \sim 40$ K. Conversely, it is known that current-driven torques couple more efficiently to low-frequency magnons [66]. We therefore interpret our results as the direct consequence of the excitation of different magnon populations, i.e., sub-thermal or thermal magnons, depending on whether the generation is produced by current-driven torques or by local thermal gradients (note that the excitation of magnon currents by thermal means do not require that the Pt injector

and the YIG film are in direct contact, but to generate a local hot spot [96]). Interestingly, the temperature dependence of the two magnon diffusion lengths indicate that they may converge at low temperatures (Fig. 7.4), where both electrical and thermal methods should excite similar magnon populations. Our results demonstrate that the magnon diffusion length is frequency-dependent, and evidence that the method and conditions at which the magnons are excited can strongly influence the magnon diffusion length, thus calling for more complex models to accurately describe diffusive magnon currents in magnetic systems. Experiments such as frequency-dependent coherent generation and propagation of magnon currents could shed some light on these questions. The role of the YIG thickness on the magnon transport for electrically excited magnons is not understood at the moment. However, we speculate that thin YIG films may favor a magnon overpopulation, even for moderate current-driven torques, or that the scattering at the YIG/GGG interface enhances the magnon scattering and thus their thermalization. Both mechanisms would result in a deformation of the magnon population for the electrically excited magnons towards the one generated by thermal means, and hence explaining the similar magnon diffusion length extracted from both methods.

High magnetic field regime. We now turn to the case of high magnetic fields (> 2 T), a regime in which both magnon diffusion lengths reduce with respect to the low field case (compare, for instance, open and solid symbols in Fig. 7.4), an effect that is more evident for temperatures above $\sim$100 K. Moreover, in contrast to the case of low magnetic fields, λ_m^{th} and λ_m^e do not coincide at any temperature, with a difference that increases up to a factor of four for temperatures above 100 K. This large difference is due to the strong decay of λ_m^e with magnetic field [Fig. 7.3(e)], whereas λ_m^{th} tends to saturate [Fig. 7.3(f)]. This different behavior of the diffusion lengths with magnetic field was already reported by Cornelissen *et al.* in a 0.2-μm-thick YIG at room temperature and was interpreted as an artifact arising from the temperature gradients present close to the detector [93].

Indeed, the influence of such thermal gradients gives rise to long-ranged nonlocal signals ($1/d^2-$regime), which are expected to dominate at distances longer than $3-5$ times the magnon diffusion length. Although we have ruled out this possibility at low fields (section 7.6.3), the decay of λ_m^{th} with increasing the magnetic field [Fig. 7.3(f)] might lead to a shift of the $1/d^2-$regime to shorter distances. Whereas at 2 T we can still clearly distinguish the exponential regime from the $1/d^2-$regime, at 5 and 9 T they cannot be distinguished (see section 7.6.3). These are precisely the magnetic fields at which λ_m^{th} tends to saturate [Fig. 7.3(f)]. Although we cannot unequivocally confirm this, our observations suggests that the apparent saturation of $\lambda_m^{th}(H)$ above 2 T could arise from an overestimation of

the magnon diffusion length caused by the fitting of the non-local signal in a region partially influenced by the thermal gradients. Alternatively, the different magnetic-field dependence of λ_m^e and λ_m^{th} could be originated by the different origin of the two type of excited magnons (sub-thermal vs thermal, respectively).

7.4 Robustness of the thermal magnon diffusion length with YIG thickness

In the following, we show that the temperature dependence of the magnon diffusion length of the thermally excited magnons at low fields is the same regardless of the YIG thickness. In Fig. 7.5, we present the temperature dependence of λ_m^{th} for our 2-μm-thick YIG (blue solid squares for sample 1 and cyan solid circles for sample 2), together with the data of two previous works: a single crystal of YIG (500 μm) grown by Czochralski method [97] (black open triangle), and a thinner YIG with a thickness of 0.2 μm grown by LPE [56] (red open triangle). Interestingly, the magnon diffusion lengths in all four samples have the same temperature dependence and comparable amplitude. This surprisingly good match evidences that the YIG thickness and the growth method are not relevant parameters that determine how far thermally excited magnon currents can flow through YIG, showing the robustness of the extracted values. Considering that these are independent measurements in three different experimental setups, but that in all of them a local thermal gradient is generated for creating the magnon currents, we conclude that λ_m^{th} is an intrinsic parameter of YIG that is associated to

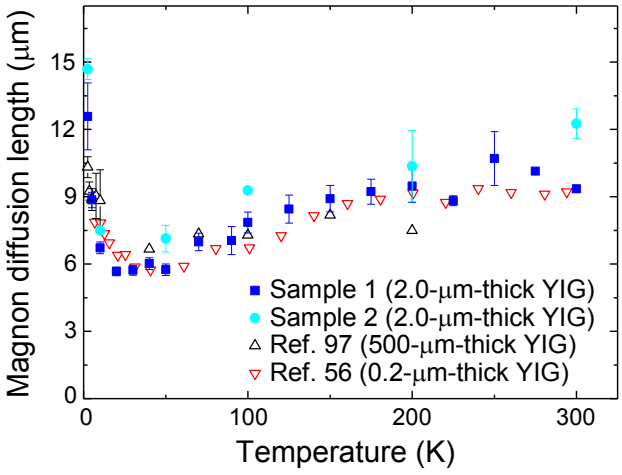

Figure 7.5: **Comparison of the thermal magnon diffusion lengths as a function of temperature for different YIG thicknesses.** Different YIG thicknesses and growth method: 2 μm (sample 1 and 2, this work), 500 μm [97], and 0.2 μm [56].

the diffusion of thermal magnons. We should mention here that the temperature dependence of λ_m^{th} for a 2.7-μm-thick YIG sample (a thickness similar to ours) is also studied in Ref. [99]. λ_m^{th} has the same trend with temperature, but with larger values: λ_m^{th} at room temperature is $\sim$ 15 μm and the maximum value at the lowest temperature rises up to $\sim$ 40 μm. We do not find an easy explanation for the difference between our values and the ones reported in Ref. [99], which might need further investigation.

7.5 Conclusions

Our magnon transport experiments performed in 2-μm-thick YIG films reveal clear differences in the diffusion lengths of electrically and thermally excited non-equilibrium magnon currents. The origin of such difference is attributed to the different non-equilibrium magnon distributions excited depending on the driving mechanism, i.e., sub-thermal and thermal magnon distributions for electrically and thermally excited magnons, respectively, suggesting that the properties of diffusive magnons are frequency dependent. The effect is clearly noticeable at the highest temperature explored (300 K), in which the energy difference between the thermal and sub-thermal magnons is maximum −being the magnon diffusion length of the thermally excited ones larger−, and gradually disappears as the temperature decreases. Moreover, the damping of the magnon currents is also magnetic field dependent, being the electrically excited magnons more damped by external magnetic fields than those thermally excited. In the case of large magnetic fields, we cannot rule out an overestimation of the magnon diffusion length for thermally excited magnons, as the non-local thermal gradients occurring in the $1/d^2$−regime might dominate at lower distances. Finally, we demonstrate that, at low magnetic fields, the same temperature dependence and size of the magnon diffusion length is obtained for thermally excited magnons in YIG samples of different thicknesses and growth conditions, demonstrating the robustness of the measurement method and that this quantity is indeed an intrinsic parameter of YIG.

7.6 Appendix

7.6.1 Appendix A: Current dependence of the non-local spin Seebeck signal at low temperatures

Figure 7.6(a) shows the angular-dependent non-local spin Seebeck signal V_{NL}^{th}, normalized to the square of the injected current, for different currents at the lowest

temperature measured ($T = 2.5$ K). The curves at lower currents do not overlap, evidencing a non-quadric dependence of the non-local voltage V_{NL}^{th}. This anomaly is also observed in Fig. 7.5(b), which shows that V_{NL}^{th} does not scale with I^2 at low currents ($I \lesssim 50$ μA). At higher currents, however, V_{NL}^{th} follows a quadratic dependence with the current, as evidenced by the linear dependence with I^2 above $I \sim 70$ μA [Fig. 7.6(b)]. This range is the one used for extracting λ_m^{th}. The current dependence of V_{NL}^{th} in the low current regime is rather linear [see Fig. 7.6(c)]. This linear dependence has already been reported in YIG at 3 K [100], but its origin remains unclear. Understanding this deviation from the expected behavior would require further studies that are beyond the scope of this work.

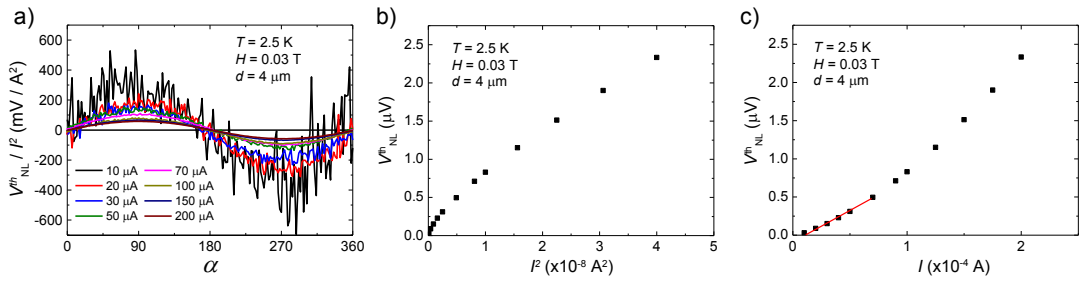

Figure 7.6: **Current dependence of the non-local signal.** (a) Angular dependence of the non-local signal V_{NL}^{th} taken for a magnetic field of 0.03 T rotating in the plane of the film and for different currents applied. The non-local voltage is normalized to the square of the applied current. Measurement temperature is 2.5 K. (b,c) Amplitude of the non-local voltage V_{NL}^{th} as a function of (b) the square of the current and (c) the current. All data correspond to Sample 1.

7.6.2 Appendix B: Temperature dependence of the non-local signal for electrically excited magnons and the spin Hall magnetoresistance.

Figure 7.7(a) shows the amplitude of the non-local signal measured for electrically excited magnons as a function of temperature and for more injector-detector distances than the ones shown in Fig. 7.3(a). The temperature dependence of the signal follows the same trend as observed in Fig. 7.3(a), although the magnetic field applied in these measurements is 1 T. Note that, whereas a signal can still be detected at temperatures below 50 K for distances up to 4 μm, the signal falls below the noise level at larger distances, preventing us from extracting the magnon diffusion length below 50 K.

Figure 7.7(b) shows the temperature dependence of the SMR measured in different Pt strips of the same sample. The SMR is a local magnetoresistance that arises from the interplay between spin accumulation generated in the Pt strip with the magnetic moments of the YIG layer [65, 66] and is thus closely

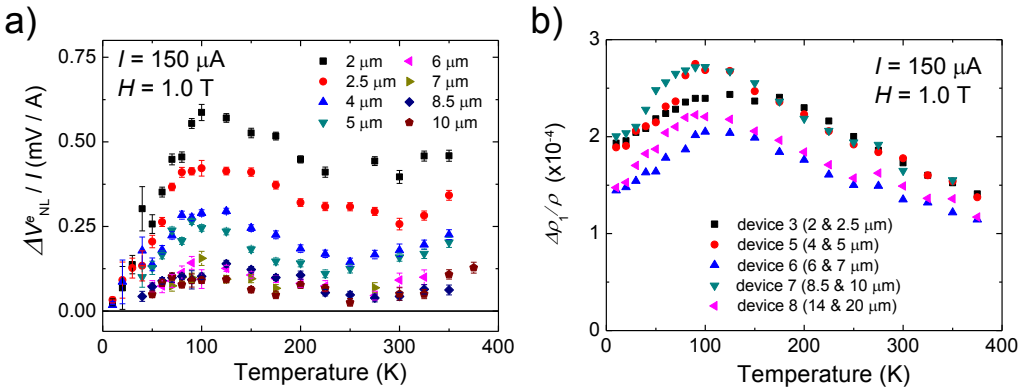

Figure 7.7: **Temperature dependence of the non-local signals for electrically excited magnons and for spin Hall magnetoresistance.** (a) Temperature dependence of the non-local voltage amplitude, normalized to the applied charge current (150 μA), for electrically excited magnons at H = 1.0 T and for different injector-detector distances. (b) Temperature dependence of the SMR amplitude $\Delta\rho_1/\rho$ measured in different Pt strips at H =1.0 T. A current of 150 μA was used. All data corresponds to Sample 1.

related to the electrical excitation of magnons studied here [20,55]. We evaluated the SMR amplitude $\Delta\rho_1/\rho$ in our devices by measuring the longitudinal ADMR in $\alpha-$plane. The temperature dependence of the SMR shows a characteristic maximum around 100 K, following a trend that was previously reported by us [54, 193], as well as by other groups [83]. According to the SMR theory [65, 84], $\Delta\rho_1/\rho$ is defined by Eq. 1.26.

Therefore, SMR only depends on the Pt parameters and the spin-mixing conductance of the interface. In the particular case of YIG, $G_r \gg G_i$ [65] (**Chapter 3**), and thus $\Delta\rho_1/\rho$ is governed by G_r, which is temperature independent [55,195] for the range explored in this experiment [84,164]. This means that the temperature dependence of the SMR is related to the spin Hall efficiency of the excitation and detection at the Pt/YIG interface [20], which would explain the behavior of the non-local signal observed in Figs. 7.3(a) and 7.7(a).

7.6.3 Appendix C: Distance dependence of the non-local signal for thermally excited magnons.

In order to determine the different regimes of the non-local thermal signals V_{NL}^{th} in our YIG films, i.e., the exponential and $1/d^2-$regimes, to ensure that the magnon diffusion length is extracted from the data belonging to the exponential regime, we used sample 2 which contains devices with longer injector-detector distances than the devices in sample 1. Figure 7.8(a) shows the amplitude of the

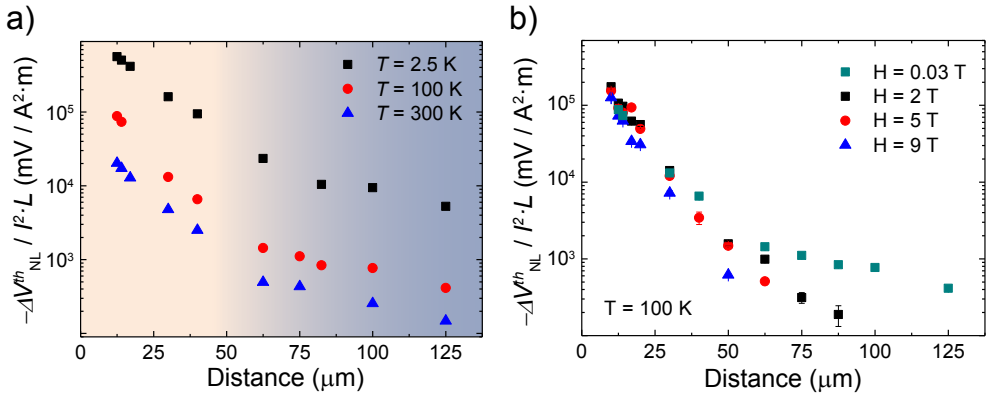

Figure 7.8: **Distance dependence of the non-local voltage amplitude for electrically excited magnons.** Distance dependence of the amplitude of the non-local voltage for thermally excited magnons taken at different temperatures in Sample 2. The signal is normalized to the square applied charge current (150 μA) and the length of the detector (L). The measurement field is $H = 0.03$ T. Two different regimes are identified: the exponential regime, for $d < 50$ μm, and the $1/d^2-$regime, for $d > 50$ μm. (b) Distance dependence of the non-local voltage for thermally generated magnons at $T = 100$ K and different magnetic fields. The two regimes are clearly distinguishable for low magnetic fields ($H = 0.03$ T and 2 T). However, at high magnetic fields it is difficult to evaluate the distance at which the threshold between the two regimes occurs.

non-local signal for thermally excited magnons at $H = 0.03$ T as a function of d and for different temperatures. Two different regimes are clearly identified: (i) for distances up to $d \sim 50$ μm, a first signal decay is identified, which corresponds to the expected exponential decay of the magnon chemical potential with distance [20, 55, 56, 93, 96, 99]. The λ_m^{th} extracted in sample 2 in this regime matches well with the values obtained in sample 1 (Fig. 7.4), confirming that the λ_m^{th} extracted in both samples indeed corresponds to the magnon diffusion length of thermally excited magnons; (ii) for $d > 50$ μm, a second signal decay with an apparent longer characteristic length is identified. In this region, the system enters in the so-called $1/d^2-$regime, in which the signal is dominated by the temperature gradients at the YIG/GGG interface beneath the Pt detector [99]. This result is indeed expected for our YIG-thickness and λ_m^{th} values, in agreement with Ref. [99]. The two regimes can be clearly distinguished for $H = 0.03$ T and 2 T [black solid and green solid squares in Fig. 7.8(b)]. However, at $H = 5$ T and 9 T [red solid circles and blue solid triangles in Fig. 7.8(b), respectively], it is difficult to evaluate the existence of both regimes as no clear change in the slope of the signal decay with d can be identified, indicating that, at the largest measured distances, both magnon transport and non-local thermal gradients might contribute to the non-local V_m^{th} signal. Note that, with increasing the magnetic field, λ_m^{th} decreases and then the emergence of the $1/d^2-$regime would shift to shorter distances. In this case, and only for these large magnetic fields, we could be overestimating λ_m^{th}.

The saturation of λ_m^{th} with magnetic field above $\sim$ 2 T might be indicating that this is the case [Fig. 7.3(f)].

Chapter 8

Absence of evidence of spin transport through amorphous $Y_3Fe_5O_{12}$

Long-distance transport of spin information in insulators without magnetic long-range-order has been recently reported. In this chapter, we perform a complete characterization of amorphous $Y_3Fe_5O_{12}$ (a-YIG) films grown on top of SiO_2. We confirm a clear amorphous structure and paramagnetic behavior of our a-YIG films, with semiconducting behavior resistivity that strongly decays with increasing temperature. The non-local transport measurements show a signal which is not compatible with spin transport and can be attributed to the drop of the a-YIG resistivity caused by Joule heating. Our results emphasize that exploring spin transport in amorphous materials requires careful procedures in order to exclude the charge contribution from the spin transport signals. This work was performed during my secondment in Tohoku University (Japan) under the supervision of Prof. Eiji Saitoh.*

*Published as: Juan M. Gomez-Perez, Koichi Oyanagi, Reimei Yahiro, Rafael Ramos, Luis E. Hueso, Eiji Saitoh and Fèlix Casanova,"Absence of evidence of spin transport through amorphous $Y_3Fe_5O_{12}$", *App. Phys. Lett.* **116**, 032401 (2020)

8.1 Introduction

Insulator-based spintronics is attracting a great amount of attention for the storage and transport of spin information because of the long spin propagation lengths [19] and the absence of energy dissipation due to ohmic loses [122] when compared to the conventional metal-based spintronics. In a ferri- and antiferromagnetic insulator, spin waves or magnons can carry spin information [19,20,52,53,55,56,85,86,90–93,97,98,101,122,193]. In particular, YIG is a ferrimagnetic insulator which has been broadly studied because of its small damping constant [196] and magnon propagation up to tens of microns [20] or even few millimeters [19,85].

Up to now, long range spin transport has been achieved in high-quality single-crystal MIs [19,20,52,53,55,56,85,86,90–93,97,98,101,122,147,193]. Moreover, recent reports have stimulated insulator-based spintronics by expanding the field to amorphous materials without long range order [197,198]. Amorphous materials are promising for future spintronics devices due to the ease for mass production, small magnetic anisotropy, and less influence of the phonons because of the lack of crystal structure. The work of D. Wesenberg *et al.* highlights the advantage of amorphous materials for long-range transport of spin information through an amorphous paramagnetic YIG without any external magnetic field applied [197]. However, in contrast reproducing the composition and structure of amorphous materials is difficult because they highly depend on the fabrication conditions and treatments. Therefore, in order to establish amorphous-based spintronics, the relation between material properties and spin transport efficiency should be elucidated.

In this chapter, we test the long-range spin transport reported in Ref. [197] by using amorphous YIG (a-YIG) films grown by magnetron-sputtering deposition on SiO_2. We first clarify the amorphous structure and chemical composition of our films by XRD and TEM/STEM. The magnetic properties are studied by VSM, exhibiting a paramagnetic behavior from room temperature down to 70 K, where an asperomagnetic order appears, which is typical for amorphous magnets [199,200]. We study the magnon transport with non-local measurements using the same measurement configuration as in Ref. [197] and standard local resistivity measurements. Our results reveal that the non-local voltage signal observed at room temperature arises from leakage current through the a-YIG films, caused by the rapidly decreasing resistivity of the a-YIG with increasing temperature and, thus, cannot be attributed to spin transport.

8.2 Experimental details

Amorphous YIG films were grown on a SiO_2 (150 nm)/Si (001) substrate by magnetron sputtering from a stochiometric $Y_3Fe_5O_{12}$ target. 200-nm-thick films were deposited at 150 W RF-power in an Ar pressure of 0.75 mTorr with a growing rate of 0.063 $\mathring{A}$/s at room temperature. No post-annealing was performed to the grown films. The characterization of the a-YIG structure and magnetic properties were carried out by XRD, TEM/STEM and VSM, respectively. TEM/STEM was performed as explained in section 2.2.3. VSM measurements were performed in a liquid-He cryostat (with a temperature T between 2 and 300 K, externally applied magnetic field $\mu_0 H$ up to 5 T).

For the spin transport measurements, we prepared pairs of Pt strips (width 1 μm, length 200 μm). The strips were patterned by positive e-beam lithography with 10 μm distance between the Pt strips. A 10-nm-thick Pt film was deposited *ex situ* via DC-magnetron-sputtering (20 W; 0.75 mTorr). In addition, we prepared a control sample, which consists of a Pt injector (width 270 nm, length 72 μm) and two non-local detectors of Pt and Cu, one at each side of the injector. The distance between the injector and each detector is 5 μm. In this case, the 5-nm-thick Pt (80 W; 3 mTorr) and 35-nm-thick Cu were prepared by DC-magnetron-sputtering *ex situ* (250 W; 2 mTorr). Transport measurements were performed as explained in section 2.2.1 measuring the non-local voltage V_{NL}

8.3 Structural characterization

Figure 8.1(a) shows the XRD spectrum of a-YIG/SiO2/Si (001) sample (purple curve) and a SiO_2/Si (001) substrate (green curve). In both cases, the same two peaks can be seen at 32.9^o and 69.1^o corresponding to Si (002) and Si (004). The absence of the peaks corresponding to crystal YIG [201] in the purple curve suggests the amorphous behavior of the film. Figure 8.1(b) shows the 200-nm-thick a-YIG on top of SiO_2/Si substrate. We performed TEM bright field images that shows a uniform amorphous structure [Fig. 8.1(c)]. The inset of Fig. 8.1(c) shows a clear halo pattern of the a-YIG lattice, which is the typical diffraction pattern for amorphous materials. Moreover, in the case of the dark field image, Fig. 8.1(d), we find very short coherent scattering areas of 0.6 nm in diameter. We also performed EDX analysis of spatial distribution of the elements along the out-of-plane direction [Fig. 8.1(e)]. By extracting the mean and the standard error of the atomic % data along the profile, we found that the concentration along the 200-nm-thick a-YIG for Fe, O and Y is constant within the error bars. The film composition is slightly different compared with stochiometric YIG

($Y_3Fe_5O_12$) [202]. The Fe and Y content is 21.9±0.4% and 12±1%, respectively, being a bit smaller than that of stochiometric YIG (where the Fe and Y content are 25% and 15%, respectively). The film is more oxidized than expected, with an O content of 68±1% instead of the stochiometric 60%.

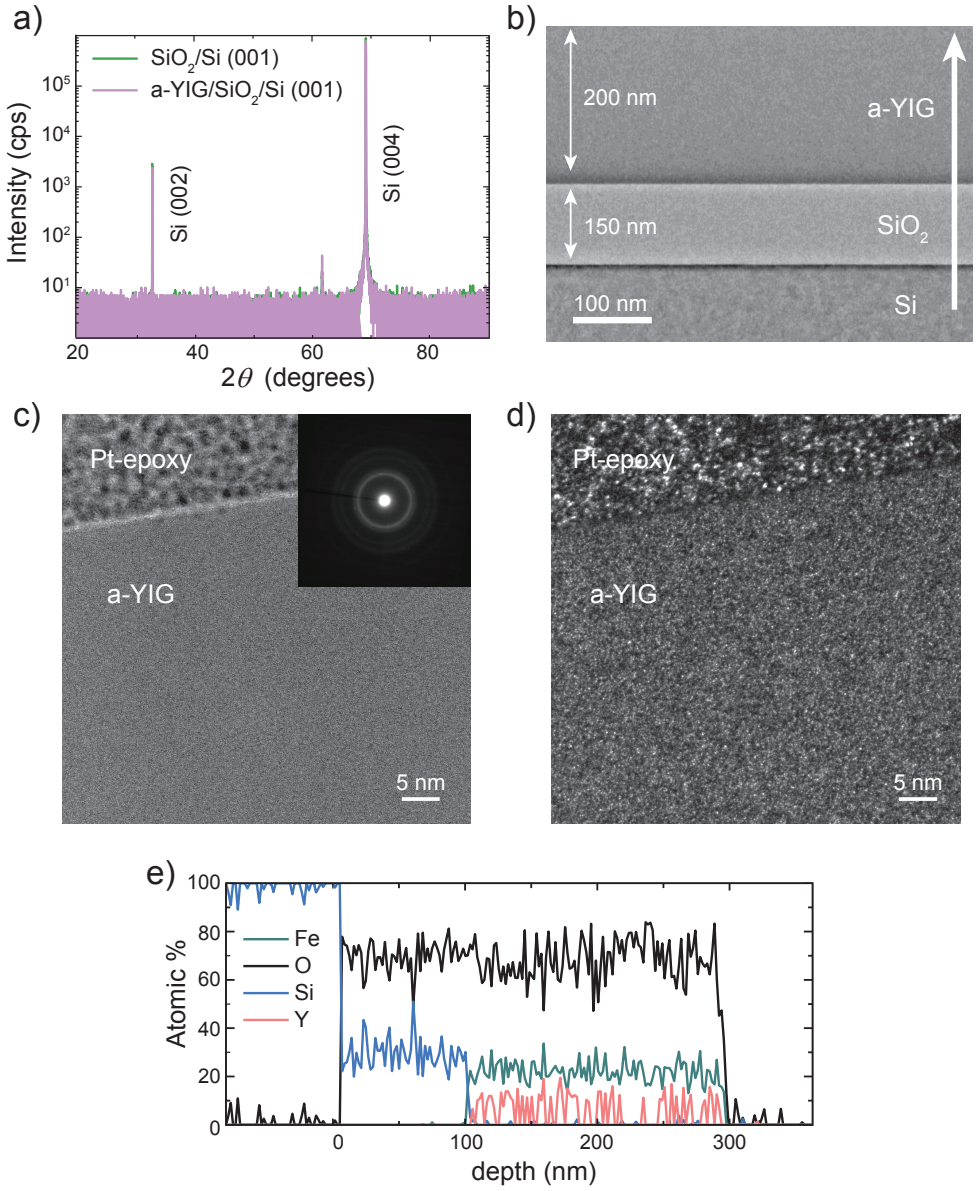

Figure 8.1: **Structural characterization of a-YIG.** (a) X-ray diffraction measurement of the SiO_2/Si (001) substrate (green) and the a-YIG film growth on top of SiO_2/Si (001) (purple). (b) TEM bright field image of the 200-nm-thick a-YIG grown on top of 150-nm-thick SiO_2/Si substrate. TEM (c) bright and (d) dark field images with a zoom of the a-YIG TEM image. The inset in (c) shows the diffraction pattern of the film. (e) Spatial distribution of the elements, measured by EDX along the out-of-plane direction, following the direction of the white arrow in panel (b). The green line corresponds to the Fe content, the black one to the O content, and the blue and red the Si and Y contents, respectively.

8.4 Magnetic characterization

Figures 8.2(a) and (b) show the a-YIG magnetization M as a function of the magnetic field H and temperature T, respectively. In both cases, the T-independent diamagnetic background of the SiO_2/Si measured in a reference substrate has been subtracted. The $M(H)$ curve at 300 K shows a linear behavior with no hysteresis between -5 T and 5 T, characteristic of the paramagnetic phase. The field-cooled (FC) curve was performed by first cooling the sample with a strong in-plane magnetic field applied (9 T) and then measuring M as a function of T while heating under a small in-plane applied magnetic field (0.5 T). For the case of zero-field-cooled (ZFC) curve, the sample was cooled down from room temperature without any applied magnetic field and, after that, a small in-plane magnetic field was applied to measure M while increasing the temperature. The FC curve gradually increases down to 70 K, being consistent with a typical Curie-Weiss trend of paramagnetic materials. However, below 70 K we find a decrease of M. This decrease, as well as the gap opening at low temperatures between FC and ZFC curves, are attributed to the phase transition of the a-YIG from a paramagnetic to an asperomagnetic phase [203, 204]. In the asperomagnetic phase, random magnetic moments add up to a non-vanishing macroscopic magnetization [49]. Hence, based on the structural and magnetic features, we confirm the amorphous and paramagnetic nature of our a-YIG films.

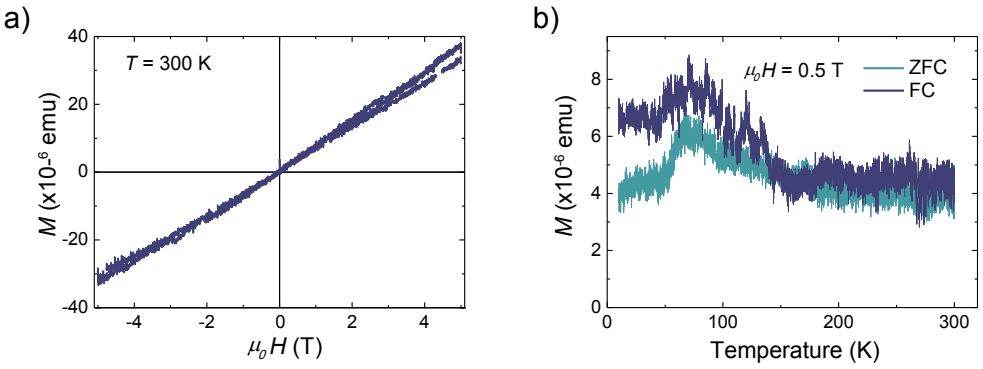

Figure 8.2: **Magnetic characterization of a-YIG.** (a) Hysteresis loop measured by VSM at room temperature. The diamagnetic background from SiO_2/Si substrate was subtracted after measuring it from a reference sample. (b) Temperature dependence of the a-YIG magnetization, the dark blue (light blue) line shows Field-Cooled (Zero-Field-Cooled) curve at $\mu_0 H = 0.5$ T. The same diamagnetic background from the SiO_2/Si substrate was also subtracted and assumed to be temperature independent.

8.5 Electrical characterization

We evaluate the electrical properties of the a-YIG film using the configuration sketched in Fig. 8.3(a). Firstly, we applied a constant voltage of 10 V between the Pt contacts and detected the current flowing through the a-YIG to measure the a-YIG resistivity (ρ_{YIG}). The purple curve in Fig. 8.3(c) corresponds to the T dependence of ρ_{YIG}, which shows a semiconducting behavior and drops with increasing T from 10^6 Ω·m at 235 K to 10^2 Ω·m at 400 K. A similar resistivity drop is reported for ultrathin YIG films [205]. At room temperature, our ρ_{YIG} is 10^4 Ω·m, which is six orders of magnitude smaller than that of single-crystal YIG at the same temperature, $\sim 10^{10}$ Ω ·m [206].

Next, we performed non-local transport measurements in the very same device [configuration sketched in Fig. 8.3(b)]. As discussed above, a non-local spin transport has been reported in a-YIG and attributed to the correlation-mediated spin current [197]. When a charge current is applied along the Pt wire, a transverse pure spin current is created due to the SHE [32]. This pure spin current generates a spin accumulation at the top and the bottom of the Pt wire. The interfacial exchange interaction would transfer spin angular momentum from Pt electrons to the local Fe^{3+} moments in a-YIG [44] and create a non-equilibrium spin accumulation in a-YIG. If a-YIG could transport this spin accumulation, that would be detected in a second Pt strip via the ISHE [32, 40]. We applied a DC charge current of 3 mA (current density $j_c \sim 10^{11}$ A/m^2) along the Pt injector and detected a non-local voltage V_{NL} across the Pt detector. Figure 8.3(c) shows the T dependence of V_{NL} (brown curve). Below 330 K, no detectable signal appears above the background noise of $\sim 2{-}5{\times}10^{-2}$ μV. However, above 330 K, a non-local signal appears, and its amplitude increases strongly up to 10^2 μV at 400 K. Coincidently, the non-local signal increases while ρ_{YIG} drops by two orders of magnitude in the range between 300 and 400 K. Interestingly, the onset temperature (T_{onset}) of $\sim$ 330 K is compatible with the one reported in Ref. [197].

To understand the origin of V_{NL}, we performed non-local measurements in the control sample [see Fig.8.4(a)]. The middle Pt strip is used as an injector and the other two are used as non-local detectors. One of them is made of Pt and the other one is made of Cu, which has a weak spin-orbit coupling and thus shows negligible SHE. We expect that, if the ISHE governs the V_{NL} detected above T_{onset}, V_{NL} will disappear for the Pt/a-YIG/Cu configuration. Figures 8.4(b) and (c) show the T dependence of V_{NL} at different currents I for the Pt and Cu detectors, respectively. For the Pt detector, we observed the very same trend shown in Fig. 8.3(c); V_{NL} appears above certain T_{onset} and increases with T. However, in contrast to our expectation, we also measured a clear V_{NL} across the Cu detector with the same trend as the Pt case, indicating that the observed

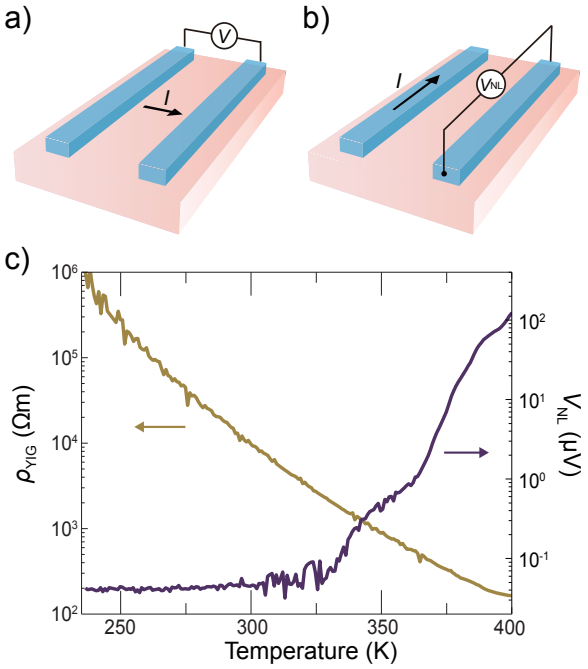

Figure 8.3: **Measurement configuration and temperature dependence of the a-YIG resistivity.** Schematics of measurement configuration for (a) the YIG resistivity ρ_{YIG} and (b) the non-local voltage V_{NL} across the Pt strip. (c) Semi-log plot of the temperature dependence of ρ_{YIG} (dark yellow) and V_{NL} (blue).

V_{NL} cannot be attributed to the spin current flowing through the a-YIG film, which is actually supported by a theoretical work [207], where they have found that the spin angular momentum cannot transfer through such disordered system.

Figure 8.4(d) shows T_{onset} in the Pt and Cu detectors as a function of I^2. Both T_{onset} show the same trend; the signal appears at lower T with larger I^2. These results can be easily understood by considering that the device temperature increases due to Joule heating, resulting in the decrease of ρ_{YIG} [the semiconducting trend shown in Fig. 8.3(c)]. Consequently, V_{NL} in both Pt and Cu detectors arise from the charge transport through the a-YIG film, because the non-local configuration we use is consistent with the van der Pauw configuration [208], and could also explain the results in Ref. [197]. This interpretation also explains why the amplitude of V_{NL} in the Cu detector is one order smaller than in the Pt detector: the higher resistivity of Pt as compared to Cu gives rise to a higher detected voltage for the same flowing current. The difference between the T_{onset} for the Cu and Pt detectors is related to this amplitude difference of the V_{NL}, the lower signal-to-noise ratio in Cu makes the extraction of an accurate value of T_{onset} difficult. Finally, if we compare our results to the ones published in Ref. [197], we can evidence the similarities in the temperature dependence of V_{NL}, as well

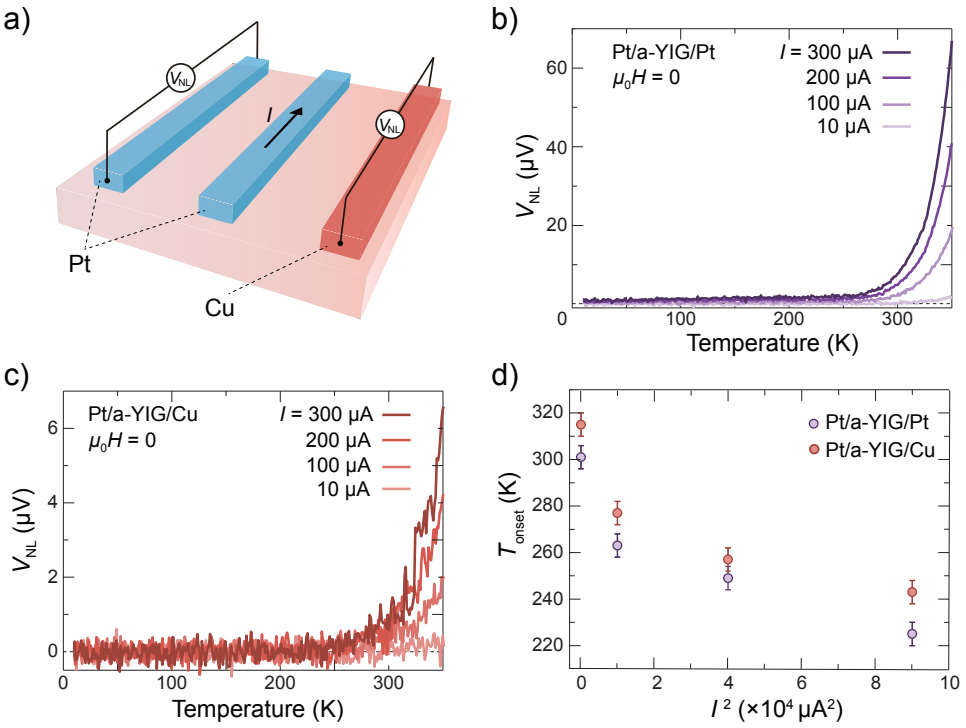

Figure 8.4: **Non-local measurements with Pt and Cu detectors.** (a) Non-local configuration measurement with a Pt injector and two non-local detectors, Pt (left) and Cu (right). The strips are separated by a distance $d = 5$ μm. Temperature dependence of the non-local voltage V_{NL} detected at (b) the Pt detector and (c) the Cu detector for different charge currents applied. (d) Onset temperature T_{onset} as a function of the square of the current $I2$ for the Pt and the Cu detectors.

as the similar T_{onset} at which we are able to detect the non-local voltage. In our case, though, we clearly demonstrate the leakage current between the contacts due to the local raise of temperature as the origin of the effect.

In addition, we performed non-local angular dependent magnetoresistance (ADMR) measurements to confirm that V_{NL} is not related to spin or magnon transport. Figure 8.5(a) shows the ADMR with the magnetic field rotating an angle β in the $zy-$plane [see sketch in Fig. 8.5(b) for the measurement configuration] at 300 K and different fields up to 5 T. There is no modulation with β as one would expect if V_{NL} is related to spin or magnon transport through a magnetic insulator [20, 52]. Moreover, we performed non-local field dependent magnetoresistance (FDMR) measurements with the magnetic field swept in the $z-$ direction (out of plane) at 300 K, shown in Fig. 8.5(b). Only a small positive magnetoresistance with no hysteresis is detected up to 9 T, ruling out again any magnon transport origin of V_{NL}, since such a large magnetic field would suppress magnons and, thus, V_{NL} [100]. Considering that the origin of V_{NL} is the current

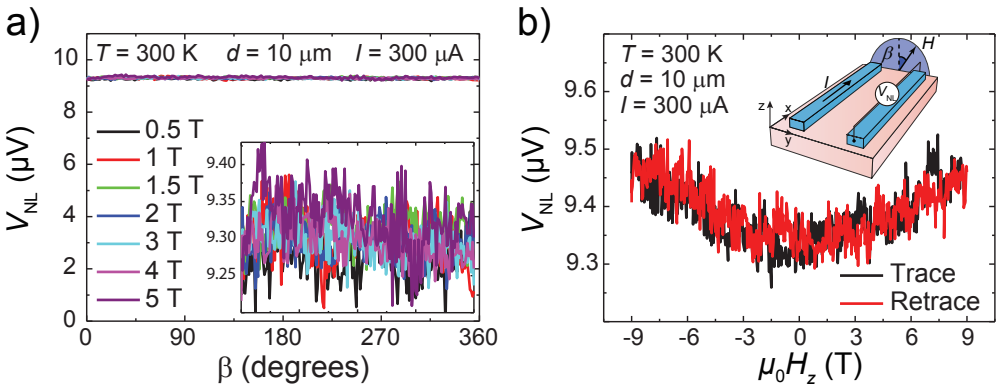

Figure 8.5: **Non-local angular- and field-dependent magnetoresistance measurements.** (a) Non-local ADMR measurements at $T = 300$ K in $\beta-$plane, see inset in (b) for the measurement configuration. (b) Non-local FDMR measurement with the magnetic field applied out-of-plane ($z-$direction).

leakage through the film, the observed FDMR is most likely ordinary magnetoresistance of the a-YIG film, since no anisotropic magnetoresistance is expected to be present in the a-YIG at this temperature, which is paramagnetic.

8.6 Conclusions

In conclusion, we carefully studied the spin transport in amorphous sputtered YIG films, as previously reported in Ref. [197]. The magnetic characterization shows a paramagnetic behavior from room temperature down to 70 K and, below 70 K, the asperomagnetism previously reported in a-YIG. Through the local and non-local transport measurements at different temperatures and applied currents, we conclude that the observed non-local voltage signal does not correspond to spin transport and can only be attributed to a leakage current between the injector and detector due to the dramatic drop of the a-YIG resistivity induced by local Joule heating.

Chapter 9

Summary and outlook

This thesis is focused on study of the spin transport through interfaces between heavy metal and magnetic insulators and the transport of the spin information through magnetic insulators. For that purpose, starting from bare magnetic insulator substrates, we performed the metal deposition and the lithography processes, and all the magnetotransport measurements, in order to experimentally study two spin-dependent phenomena at the HM/MI interface by spin Hall magnetoresistance and magnon spin transport. We study the importance of the *spin-mixing* conductance at the interface of different MI and which is the influence of G_r, G_i and G_s in the spin transport through the HM/MI interface depending on the magnetic order of the MI.

Part I. *Spin Hall Magnetoresistance in Magnetic Insulators*

In **Part I**, we performed a local study of the spin transport properties at the interface by using Pt Hall bar devices on top of different magnetic insulators: (i) ferrimagnetic insulator, (ii) synthetic antiferromagnetic insulator, (iii) paramagnetic insulator and (iv) ferromagnetic insulator.

- In **Chapter 3**, we employed first Pt/YIG for longitudinal ADMR measurements and Hall configuration measurements extracting the two amplitudes relates to SMR ($\Delta\rho_1/\rho$ and $\Delta\rho_2/\rho$, respectively). We extracted a $G_r = (3.8 \pm 1.0) \times 10^{14}\ \Omega^{-1}\mathrm{m}^{-2}$ and a ratio G_r/G_i of 22 ± 3, compatible to previous reports in Pt/YIG interfaces. However, there has been some controversies about using Pt for SMR experiments. In particular, the $\Delta\rho_2/\rho$ term, similar behavior to AHE, and might be interpreted as magnetic proximity effect in Pt. Therefore, in order to discard the possible presence of magnetic proximity effect in Pt, we employed Au instead of Pt as a HM,

measuring again the SMR amplitudes. The observed $\Delta\rho_1/\rho$ and $\Delta\rho_2/\rho$ amplitudes in both studied systems, Au/YIG and Pt/YIG, are consistent with the same physical picture of SMR. This means that the AHE-like signal observed in the Hall configuration can be fully understood by the role of the imaginary part of the spin-mixing conductance.

- In **Chapter 4**, we studied the evolution of the magnetization depending on the magnetic field intensity in a synthetic AFM formed by a YIG/GdIG bilayer grown on top of GGG. We demonstrated by SMR and XMCD measurements that YIG magnetization opposes to the external magnetic field. Furthermore, we observed a memory effect between orthogonal magnetization orientations, which can be read *via* longitudinal SMR measurements. In terms of applications, the system could be exploited for insulating spintronic devices, such as writing operations with spin-orbit torque and reading operations with SMR in insulating magnetic memories.

- In **Chapter 5** we demonstrate the presence of SMR in Pt/GGG, which is a text-book paramagnetic insulator. At low temperature, we can saturate the SMR amplitude for $\mu_0 H > 3.5$ T, at 2 K. In addition, we could detect the AHE-like contribution predicted by SMR theory. We model our experimental results to the microscopic SMR theory, obtaining the field dependence for the *spin-mixing* conductance terms. From this analysis, we found that the field-like torque (G_i) contribution is as important as the spin-transfer torque (G_r) contribution in Pt/GGG interface, with both values around $\sim 10^{13}$ $\Omega^{-1}\mathrm{m}^{-2}$.

- In **Chapter 6**, we observed the presence of SMR in Pt/EuS heterostructure, where EuS is a ferromagnetic insulator below 30 K. The SMR is observed by ADMR and FDMR measurements, in which the magnetization reversal of EuS is observed. Furthermore, we also measure the AHE-like contribution of the SMR, driven by a large imaginary part of the spin-mixing conductance. By using the microscopic SMR theory we can extract the microscopic parameters such as the the exchange interaction between the $1s$ electrons of Pt and the $4f$ efectrons of Eu, $J_{sf} \sim 17{-}19$ meV. Our analysis of the spin conductances revels for the first time experimentally a larger field-like torque ($G_i \sim 8{\times}10^{12}$ $\Omega^{-1}\mathrm{m}^{-2}$) than spin-transfer torque ($G_r \sim 2{\times}10^{12}$ $\Omega^{-1}\mathrm{m}^{-2}$) in a HM/MI interface. The effective exchange field associated to G_i is expected to be ~ 1 meV. Therefore, SMR measurements offer a simple way to quantify effective fields which are of interest in different areas, such as superconducting applications.

Part II. *Magnon Spin Transport in Magnetic Insulators*

In **Part II** we presented our experimental results of transport of spin information along two different magnetic insulators by using a non-local configuration, where one Pt strip acts as an injector and the second one as a detector. The two magnetic insulators are: (i) YIG, the typical ferrimagnetic insulator broadly studied, and (ii) amorphous YIG, an insulator without a long-range magnetic order.

- In **Chapter 7**, we measured non-local magnetotransport through 2-μm-thick YIG films. We performed a systematic study for different temperatures and magnetic fields. Our results reveal clear differences in the magnon diffusion lengths between electrically and thermally excited magnons. The origin of such difference is attributed to the different non-equilibrium magnon distributions excited depending on the driving mechanism, suggesting that the diffusion properties of magnons are frequency dependent. In addition, the magnon currents are also magnetic-field dependent. When the magnetic field increases, the electrically excited magnons are more damped than the thermal ones, meaning that they will be detected for shorter distances. Finally, we demonstrate that, at low magnetic fields, the same temperature dependence and size of the magnon diffusion length is obtained for thermally excited magnons in YIG samples of different thicknesses and growth conditions.

- In **Chapter 8**, we cautiously studied the spin transport in amorphous YIG. The non-local transport measurements as a function of the temperature show a clear signal that cannot be compatible with spin transport. We conclude that the non-local detected voltage can only be attributed to a leakage current between the Pt strips due to the drop of the amorphous YIG resistivity at high temperatures.

As a summary of this thesis, we have performed a deep study of spin-dependent phenomena related to HM/MI interfaces, studying both local and non-local spin transport properties. However, there is further work to do. In the case of SMR in different magnetic insulators, it would be appealing to study the interface between a heavy metal and antiferromagnetic insulator from the point of view of the experiments and the microscopic theory as well, to understand the field and temperature dependence of the spin-mixing conductance terms. For instance MnO, which is a antiferromagnetic insulator with a Néel temperature of 530 K. On the other hand, related to magnon spin transport it can be worth

studying a ferromagnetic insulator such as EuS or EuO. First, to check if the magnon transport is more efficient in a ferromagnet than in a ferrimagnet or paramagnet, i.e., whether the magnons can be transported for longer distances. Second, it is worth studying the magnon transport close to the ferromagnetic to paramagnetic transition.

List of acronyms and symbols

Acronyms

ADMR – Angular dependent magnetoresistance
AFM – Antiferromagnetic
AHE – Anomalous Hall effect
AMR – Anisotropy magnetoresistance
ac – alternating current
DI – Deionized
dc – Direct current
eBL – Electron-beam lithography
EDX – Energy dispersive x-ray spectroscopy
EuS – Europium sulfide
FC – Field cooled
FDMR – Field dependent magnetoresistance
FeA – 2 octahedrically coordinated Fe^{3+} ions per formula sublattice in YIG and GdIG
FeD – 3 tetrahedrically coordinated Fe^{3+} ions per formula sublattice in YIG and GdIG
FM – Ferromagnetic material
FMI – Ferromagnetic insulator
FMR – Ferromagnetic resonance
GGG – Gadolinium gallium garnet
GdIG – Gadolinium iron garnet
GMR – Giant magnetoresistance
GPA – Geometrical phase analysis
HM – Heavy metal
HR-TEM – High resolution transmission electron microscopy
HAADF – High angle annular dark field
HV – High vacuum
IPA – Isopropyl
ISHE – Inverse spin Hall effect
LPE – Liquid phase epitaxy

MI – Magnetic insulator
MRAM – Magnetic random access memory
MTJ – Magnetic tunnel junction
NM – Normal metal
OHE – Ordinary Hall effect
PLD – Pulsed laser deposition
PM – Paramagentic material
PI – Paramagnetic insulator
SHE – Spin Hall effect
SMR – Spin Hall magnetoresistance
SOC – Spin orbit coupling
SOT – Spin orbit torque
SP – Spin pumping
SSE – Spin Seebeck effect
STT – Spin transfer torque
STEM – Scanning transmission electron microscopy
SQUID – Superconducting quantum interference devices
TEM – Transmission electron microscopy
TEY – Total yield detection
TMR – Tunnel magnetoresistance
VSM – Vibrating sample magnetometer
XAS – X-ray absorption spectrum
XMCD – X-ray magnetic circular dichroism
XRR – X-ray reflectivity
XRD – X-ray diffraction
YIG – Yttrium iron garnet
ZFC – Zero field cooled

Symbols

B – Induced magnetic field
c – Speed of the light
d_N – thickness
D – Diffusion coefficient
e – electron charge
E_g – Energy gap
g – Gyromagnetic factor
$G_{\uparrow\downarrow}$ – Spin-mixing conductance
G_r – Real part spin-mixing conductance
G_i – Imaginary part spin-mixing conductance
G_s – Spin-sink conductance or effective spin-mixing conductance

H – Magnetic field
H_x – Magnetic field applied in $x-$direction
H_y – Magnetic field applied in $y-$direction
H_z – Magnetic field applied in $z-$direction
H_u – Perpendicular anisotropy field
H_{SOC} – Hamiltonian of the spin orbit coupling
$\hbar$ – normalized Plack constant
I – Charge current
$\Im$ – Imaginary part
J_{ad} – Antiferromagnetic exchange coupling energy between FeD and FeA sublattices in YIG
J_{ac} – Antiferromagnetic exchange coupling energy between Gd and FeA magnetic moments in GdIG
J_{cd} – Antiferromagnetic exchange coupling energy between Gd and FeD magnetic moments in GdIG
J_c – Charge current density
J_{ad} – Spin current
J_{ex} – Nearest-neighbor exchange interaction
J_{sd} – Exchange coupling between s electron in Pt and the $d(f)$ spins in EuS (GGG)
J_1 – Ferromagnetic exchange coupling first neighbors in EuS
J_2 – Antiferromagnetic exchange coupling second neighbors in EuS
L – Orbital angular momentum
l – length
M – Magnetization
M_s – Saturated magnetization
M_{eff} – Effective magnetization
m_e – Electron mass
$\boldsymbol{m}_s$ – Unit vector along the magnetic field
m_x – Unit vector component in $x-$direction
m_y – Unit vector component in $y-$direction
m_z – Unit vector component in $z-$direction
$n_s = n_{imp}^{2D}$ – Density of magnetic atoms
R_L – Longitudinal resistance
R_T – Transverse resistance
R_0 – Base resistance
R_{OHE} – Hall coefficient
$\Re$ – Real part
r – Distance between the electron and the nucleus in an atom
s – Spin polarization
S – Spin angular momentum
$\langle S_{\parallel} \rangle$ – longitudinal spin operator of a representative local moment

A

$\langle S_\perp \rangle$ – perpendicular spin operator of a representative local moment
l – thickness
T – Temperature
T_c – Curie temperature
V – Voltage
V_L – Longitudinal voltage
V_T – Transverse voltage
V_{NL} – Non-local voltage
V_{NL}^e – Non-local voltage electrical component
V_{NL}^{th} – Non-local voltage thermal component
w – width
Z – Atomic number

α – Sweeping angle of the magnetic field in plane ($xy-$plane)
α_0 – Phase shift in the synthetic AFM β – Sweeping angle of the magnetic field in plane ($zy-$plane)
γ – Sweeping angle of the magnetic field in plane ($zx-$plane)
γ – Gyromagnetic ratio
$\Delta\rho_1$ – SMR amplitude measure in longitudinal configuration
$\Delta\rho_2$ – AHE-like amplitude in SMR measurments
$\Delta\rho_L$ – Longitudinal SMR amplitude
$\Delta\rho_T$ – Transverse SMR amplitude
ΔT – Temperature gradient
ϵ_0 – Electric constant
θ_{SH} – Spin Hall angle
θ_{CW} – Curie-Weiss temperature
λ – Spin diffusion length
λ_m – Magnon diffusion length
λ_m^e – Magnon diffusion length for electrically excited magnons
λ_m^{th} – Magnon diffusion length for thermally excited magnons
Λ – Effective spin diffusion length
μ_B – Bohr magneton
μ_0 – Orbital magnetic moment
μ_s – Spin magnetic moment
ρ – Base resistivity
ρ_L – Longitudinal resistivity
ρ_T – Transverse resistivity
ρ_{xx} – Longitudinal resistivity
ρ_{xy} – Transverse resistivity
σ – Conductivity
σ_{xx} – Longitudinal conductivity

A

σ_{SH} – Spin Hall conductivity
$\tau_{\parallel}$ – Longitudinal spin relaxation time
$\tau_{\perp}$ – Transverse spin relaxation time
νJ_{sd} – Exchange interaction

A

Bibliography

[1] S. M. Sze and K. K. Ng, *Physics of semiconductor devices* (John wiley & sons, 2006).

[2] R. R. Schaller, *IEEE spectrum* **34**, 52 (1997).

[3] M. M. Waldrop, *Nature* **530**, 144 (2016).

[4] G. Binasch, P. Grünberg, F. Saurenbach, and W. Zinn, *Physical Review B* **39**, 4828 (1989).

[5] M. N. Baibich *et al.*, *Physical Review Letters* **61**, 2472 (1988).

[6] C. Chappert, A. Fert, and F. N. Van Dau, The emergence of spin electronics in data storage, in *Nanoscience And Technology: A Collection of Reviews from Nature Journals*, pp. 147–157, World Scientific, 2010.

[7] M. Julliere, *Physics Letters A* **54**, 225 (1975).

[8] D. Wang, C. Nordman, J. M. Daughton, Z. Qian, and J. Fink, *IEEE Transactions on Magnetics* **40**, 2269 (2004).

[9] S. Ikeda *et al.*, *Applied Physics Letters* **93**, 082508 (2008).

[10] J. C. Slonczewski, *Journal of Magnetism and Magnetic Materials* **159**, L1 (1996).

[11] L. Berger, *Physical Review B* **54**, 9353 (1996).

[12] S. Maekawa, S. O. Valenzuela, E. Saitoh, and K. Kimura, *Spin current* (, 2012).

[13] N. F. Mott, *Proceedings of the Royal Society of London. Series A-Mathematical and Physical Sciences* **153**, 699 (1936).

[14] A. Fert and I. Campbell, *Physical Review Letters* **21**, 1190 (1968).

[15] A. Fert and I. Campbell, *Journal of Physics F: Metal Physics* **6**, 849 (1976).

[16] M. D'yakonov and V. Perel, *Soviet Journal of Experimental and Theoretical Physics Letters* **13**, 467 (1971).

[17] J. Hirsch, *Physical Review Letters* **83**, 1834 (1999).

[18] S. Yakata, Y. Ando, T. Miyazaki, and S. Mizukami, *Japanese journal of applied physics* **45**, 3892 (2006).

[19] Y. Kajiwara *et al.*, *Nature* **464**, 262 (2010).

[20] L. J. Cornelissen, J. Liu, R. A. Duine, J. B. Youssef, and B. J. Van Wees, *Nature Physics* **11**, 1022 (2015), 1505.06325.

[21] H. Idzuchi, Y. Fukuma, and Y. Otani, *Physica E: Low-dimensional Systems and Nanostructures* **68**, 239 (2015).

[22] A. Slachter, F. L. Bakker, J.-P. Adam, and B. J. van Wees, *Nature Physics* **6**, 879 (2010).

[23] K. Ando *et al.*, *Physical review letters* **101**, 036601 (2008).

[24] T. Kimura and Y. Otani, *Physical Review Letters* **99**, 196604 (2007).

[25] K. Ando, *Semiconductor Science and Technology* **29**, 043002 (2014).

[26] J. Flipse, F. Bakker, A. Slachter, F. Dejene, and B. Van Wees, *Nature nanotechnology* **7**, 166 (2012).

[27] A. Manchon, H. C. Koo, J. Nitta, S. Frolov, and R. Duine, *Nature materials* **14**, 871 (2015).

[28] A. Soumyanarayanan, N. Reyren, A. Fert, and C. Panagopoulos, *Nature* **539**, 509 (2016).

[29] A. Manchon and A. Belabbes*Spin-Orbitronics at Transition Metal Interfaces* Vol. 68 (Elsevier, 2017).

[30] D. Vaz, *Unité Mixte de Physique CNRS/Thales associée à l'Université Paris-Saclay* , PhD thesis (2018).

[31] A. Hoffmann, *IEEE transactions on magnetics* **49**, 5172 (2013).

[32] J. Sinova, S. O. Valenzuela, J. Wunderlich, C. H. Back, and T. Jungwirth, *Reviews of Modern Physics* **87**, 1213 (2015), 1411.3249.

[33] E. H. Hall, *American Journal of Mathematics* **2**, 287 (1879).

[34] E. H. Hall, *The London, Edinburgh, and Dublin Philosophical Magazine and Journal of Science* **12**, 157 (1881).

[35] A. W. Smith and R. Sears, *Physical Review* **34**, 1466 (1929).

[36] R. Karplus and J. Luttinger, *Physical Review* **95**, 1154 (1954).

[37] Y. K. Kato, R. C. Myers, A. C. Gossard, and D. D. Awschalom, *Science* **306**, 1910 (2004).

[38] J. Wunderlich, B. Kaestner, J. Sinova, and T. Jungwirth, *Physical Review Letters* **94**, 047204 (2005).

[39] S. O. Valenzuela and M. Tinkham, *Nature* **442**, 176 (2006).

[40] E. Saitoh, M. Ueda, H. Miyajima, and G. Tatara, *Applied Physics Letters* **88**, 182509 (2006).

[41] T. Tanaka *et al.*, *Physical Review B* **77**, 165117 (2008).

[42] E. Sagasta *et al.*, *Physical Review B* **94**, 060412 (2016).

[43] S. Mizukami, Y. Ando, and T. Miyazaki, *Physical Review B* **66**, 104413 (2002).

[44] Y. Tserkovnyak, A. Brataas, and G. E. W. Bauer, *Physical Review B* **66**, 224403 (2002).

[45] K. Uchida *et al.*, *Nature materials* **9**, 894 (2010).

[46] K. Uchida *et al.*, *Applied Physics Letters* **97**, 172505 (2010).

[47] J. Flipse *et al.*, *Physical Review Letters* **113**, 027601 (2014), 1311.4772.

[48] X. Jia, K. Liu, K. Xia, and G. E. W. Bauer, *EPL (Europhysics Letters)* **96**, 17005 (2011), 1103.3764.

[49] J. M. Coey, *Magnetism and magnetic materials* (Cambridge university press, 2010).

[50] C. Kittel, *Introduction to Solid State Physics*, 8 ed. (Wiley, 2004).

[51] W. Müller and W. Nolting, *Physical Review B* **66**, 085205 (2002).

[52] S. T. B. Goennenwein *et al.*, *Applied Physics Letters* **107**, 172405 (2015).

[53] S. Vélez, A. Bedoya-Pinto, W. Yan, L. E. Hueso, and F. Casanova, *Physical Review B* **94**, 174405 (2016).

[54] S. Vélez *et al.*, *Physical Review Letters* **116**, 016603 (2016).

[55] L. J. Cornelissen, K. J. H. Peters, G. E. W. Bauer, R. A. Duine, and B. J. van Wees, *Physical Review B* **94**, 014412 (2016).

[56] L. J. Cornelissen, J. Shan, and B. J. Van Wees, *Physical Review B* **94**, 180402(R) (2016).

[57] J. Barker and G. E. Bauer, *Physical Review B* **100**, 140401 (2019).

[58] A. Brataas, G. E. Bauer, and P. J. Kelly, *Physics Reports* **427**, 157 (2006).

[59] Y. Huai *et al.*, *AAPPS bulletin* **18**, 33 (2008).

[60] H. Adachi, J.-i. Ohe, S. Takahashi, and S. Maekawa, *Physical Review B* **83**, 094410 (2011).

[61] M. Weiler *et al.*, *Physical Review Letters* **111**, 176601 (2013).

[62] O. Mosendz *et al.*, *Physical Review B* **82**, 214403 (2010).

[63] T. J. Seebeck, *Annalen der Physik* **82**, 253 (1826).

[64] K. Uchida *et al.*, *Journal of Physics: Condensed Matter* **26**, 343202 (2014).

[65] Y.-T. Chen *et al.*, *Physical Review B* **87**, 144411 (2013).

[66] H. Nakayama *et al.*, *Physical Review Letters* **110**, 206601 (2013).

[67] S. Y. Huang *et al.*, *Physical Review Letters* **109**, 107204 (2012).

[68] S. Rüegg *et al.*, *Journal of Applied Physics* **69**, 5655 (1991).

[69] Y. M. Lu *et al.*, *Physical Review B* **87**, 220409 (2013).

[70] B. Miao, S. Huang, D. Qu, and C. Chien, *Physical Review Letters* **112**, 236601 (2014).

[71] T. Shang *et al.*, *Scientific Reports* **5**, 17734 (2015).

[72] G. Schütz *et al.*, *Journal of applied physics* **73**, 6430 (1993).

[73] J. Geissler *et al.*, *Physical Review B* **65**, 020405 (2001).

[74] S. Geprägs *et al.*, *Applied Physics Letters* **101**, 262407 (2012).

[75] M. Isasa *et al.*, *Applied Physics Letters* **105**, 142402 (2014).

[76] M. Isasa *et al.*, *Physical Review Applied* **6**, 034007 (2016).

[77] M. Dyakonov, *Physical review letters* **99**, 126601 (2007).

[78] Y. Shiomi *et al.*, *Applied Physics Letters* **104**, 242406 (2014).

[79] M. Althammer *et al.*, *Physical Review B* **87**, 224401 (2013).

[80] N. Vlietstra *et al.*, *Applied Physics Letters* **103**, 032401 (2013).

[81] C. Hahn *et al.*, *Physical Review B* **87**, 174417 (2013).

[82] N. Vlietstra, J. Shan, V. Castel, B. J. Van Wees, and J. Ben Youssef, *Physical Review B* **87**, 184421 (2013).

[83] S. R. Marmion, M. Ali, M. McLaren, D. A. Williams, and B. J. Hickey, *Physical Review B* **89**, 220404 (2014).

[84] X.-P. Zhang, F. S. Bergeret, and V. N. Golovach, *Nano Letters* **19**, 6330 (2019).

[85] A. V. Chumak *et al.*, *Applied Physics Letters* **100**, 082405 (2012).

[86] B. L. Giles, Z. Yang, J. S. Jamison, and R. C. Myers, *Physical Review B* **92**, 224415 (2015).

[87] W. Yan *et al.*, *Nature Communications* **8**, 661 (2017).

[88] C. Stamm *et al.*, *Physical Review Letters* **119**, 087203 (2017).

[89] W. Savero Torres *et al.*, *2D Materials* **4**, 041008 (2017).

[90] J. Shan *et al.*, *Applied Physics Letters* **110**, 132406 (2017).

[91] K. Ganzhorn *et al.*, *AIP Advances* **7**, 085102 (2017).

[92] J. Cramer *et al.*, *Nano Letters* **17**, 3334 (2017), 1703.03218.

[93] L. J. Cornelissen and B. J. Van Wees, *Physical Review B* **93**, 020403(R) (2016).

[94] S. Vélez *et al.*, *Physical Review B* **100**, 180401 (2019).

[95] K. Ganzhorn *et al.*, *Applied Physics Letters* **109**, 022405 (2016).

[96] J. Shan *et al.*, *Physical Review B* **94**, 174437 (2016).

[97] B. L. Giles *et al.*, *Phys. Rev. B* **96**, 180412(R) (2017).

[98] S. Geprägs *et al.*, *Nature Communications* **7**, 10452 (2016).

[99] J. Shan *et al.*, *Physical Review B* **96**, 184427 (2017).

[100] L. J. Cornelissen *et al.*, *Physical Review B* **96**, 104441 (2017).

[101] R. Lebrun *et al.*, *Nature* **561**, 222 (2018).

[102] M. Swain, p. PhD thesis (2015).

[103] Z. Wang and Z. Zhang, *Electron beam evaporation deposition* (Wiley Online Library, 2016).

[104] D. L. Smith, *Thin-film deposition: principles and practice* (McGraw Hill Professional, 1995).

[105] M. Altissimo, *Biomicrofluidics* **4**, 026503 (2010).

[106] A. Barla *et al.*, *Journal of Synchrotron Radiation* **23**, 1507 (2016).

[107] J. Daillant and A. Gibaud*X-ray and neutron reflectivity: principles and applications* Vol. 770 (Springer, 2008).

[108] *http://www.crystallography.net/cod/* .

[109] D. Hou *et al.*, *Nature Communications* **7**, 12265 (2016).

[110] T. Kimura, J. Hamrle, and Y. Otani, *Physical Review B* **72**, 014461 (2005).

[111] J. T. Brangham *et al.*, *Physical Review B* **94**, 054418 (2016).

[112] M. Obstbaum *et al.*, *Physical Review B* **89**, 060407 (2014).

[113] V. Vlaminck, J. E. Pearson, S. D. Bader, and A. Hoffmann, *Physical Review B* **88**, 064414 (2013).

[114] M. Isasa, E. Villamor, L. E. Hueso, M. Gradhand, and F. Casanova, *Physical Review B* **91**, 024402 (2015).

[115] Y. Niimi *et al.*, *Physical Review B* **89**, 054401 (2014).

[116] O. Mosendz, G. Woltersdorf, B. Kardasz, B. Heinrich, and C. H. Back, *Physical Review B* **79**, 224412 (2009).

[117] P. Laczkowski *et al.*, *Physical Review B* **85**, 220404 (2012).

[118] D. Qu, S. Y. Huang, G. Y. Guo, and C. L. Chien, *Physical Review B* **97**, 024402 (2018).

[119] M. Obstbaum *et al.*, *Physical Review Letters* **117**, 167204 (2016).

[120] P. Li *et al.*, *Nature Communications* **7**, 12688 (2016).

[121] C. O. Avci *et al.*, *Nature Materials* **16**, 309 (2016).

[122] A. V. Chumak, V. I. Vasyuchka, A. A. Serga, and B. Hillebrands, *Nature Physics* **11**, 453 (2015).

[123] C. Dubs *et al.*, *Journal of Physics D: Applied Physics* **50**, 204005 (2017).

[124] S. A. Manuilov and A. M. Grishin, *Journal of Applied Physics* **108**, 123917 (2010).

[125] S. A. Manuilov and A. M. Grishin, *Journal of Applied Physics* **108**, 013902 (2010).

[126] C. Hauser *et al.*, *Scientific Reports* **6**, 20827 (2016).

[127] H. Chang *et al.*, *IEEE Magnetics Letters* **5**, 6700104 (2014).

[128] E. L. Jakubisova, S. Visnovsky, H. Chang, and M. Wu, *Applied Physics Letters* **108**, 082403 (2016).

[129] A. Mitra *et al.*, *Scientific Reports* **7**, 11774 (2017).

[130] J. C. Gallagher *et al.*, *Applied Physics Letters* **109**, 072401 (2016).

[131] R. A. Duine, K.-J. Lee, S. S. P. Parkin, and M. D. Stiles, *Nature Physics* **14**, 217 (2018).

[132] K. W. Urban *et al.*, *Philosophical Transactions of the Royal Society A: Mathematical, Physical and Engineering Sciences* **367**, 3735 (2009).

[133] a. K. Gutakovskii, a. L. Chuvilin, and S. a. Song, *Bulletin of the Russian Academy of Sciences: Physics* **71**, 1426 (2007).

[134] S. Geller, G. P. Espinosa, and P. B. Crandall, *Journal of Applied Crystallography* **2**, 86 (1969).

[135] D. Hou *et al.*, *Physical Review Letters* **118**, 147202 (2017).

[136] P. Wang *et al.*, *Applied Physics Letters* **109** (2016).

[137] J. Chakhalian *et al.*, *Science* **318**, 1114 (2007).

[138] G. F. Dionne, *Journal of Applied Physics* **41**, 4874 (1970).

[139] T. D. C. Higgs *et al.*, *Scientific Reports* **6**, 30092 (2016).

[140] A. B. Harris, *Phys. Rev.* **132**, 2398 (1962).

[141] K. Ganzhorn *et al.*, *arXiv:1705.02871* (2017).

[142] T. Yamagishi *et al.*, *Philosophical Magazine* **85**, 1819 (2005).

[143] S. Parkin *et al.*, *IEEE* **91**, 661 (2003).

[144] T. Jungwirth, X. Marti, P. Wadley, and J. Wunderlich, *Nature Nanotechnology* **11**, 231 (2016).

[145] S. B. Ubizskii, *Journal of Magnetism and Magnetic Materials* **195**, 575 (1999).

[146] L. Pietrobon *et al.*, *Small* **11**, 6295 (2015).

[147] K. Oyanagi *et al.*, *Nature Communications* **10**, 1 (2019).

[148] K. Ghimire, H. F. Haneef, R. W. Collins, and N. J. Podraza, *Physica Status Solidi (b)* **252**, 2191 (2015).

[149] W. Kinney and W. Wolf, *Journal of Applied Physics* **50**, 2115 (1979).

[150] P. Schiffer *et al.*, *Physical Review Letters* **74**, 2379 (1995).

[151] P. Schiffer, A. Ramirez, D. A. Huse, and A. Valentino, *Physical Review Letters* **73**, 2500 (1994).

[152] J. Overmeyer, E. Giess, M. Freiser, and B. Calhoun, *Paramagnetic Resonance* (Academic, New York, 1963).

[153] S. Meyer *et al.*, *Applied Physics Letters* **106**, 132402 (2015).

[154] R. Schlitz *et al.*, *Applied Physics Letters* **112**, 132401 (2018).

[155] H. Wu *et al.*, *Physical Review B* **94**, 174407 (2016).

[156] S. Meyer *et al.*, *Applied Physics Letters* **104**, 242411 (2014).

[157] G. R. Hoogeboom, A. Aqeel, T. Kuschel, T. T. Palstra, and B. J. Van Wees, *Applied Physics Letters* **111**, 052409 (2017).

[158] L. Baldrati *et al.*, *Physical Review B* **98**, 024422 (2018).

[159] Y. Ji *et al.*, *Applied Physics Letters* **110**, 262401 (2017).

[160] H. Wang *et al.*, *Journal of Applied Physics* **122**, 083907 (2017).

[161] J. Fischer *et al.*, *Physical Review B* **97**, 014417 (2018).

[162] K. Ganzhorn *et al.*, *Physical Review B* **94**, 094401 (2016), 1605.07441.

[163] A. Aqeel *et al.*, *Physical Review B* **94**, 134418 (2016).

[164] S. Vélez *et al.*, *Physical Review B* **100**, 180401(R) (2019).

[165] A. Aqeel *et al.*, *Physical Review B* **92**, 224410 (2015).

[166] M. Lammel *et al.*, *Applied Physics Letters* **114**, 252402 (2019).

[167] K. Oyanagi *et al.*, *Unpublished* .

[168] J. Moodera, X. Hao, G. Gibson, and R. Meservey, *Physical Review Letters* **61**, 637 (1988).

[169] B. Li *et al.*, *Physical Review Letters* **110**, 097001 (2013).

[170] E. Strambini *et al.*, *Physical Review Materials* **1**, 054402 (2017).

[171] M. Rouco *et al.*, *Physical Review B* **100**, 184501 (2019).

[172] F. S. Bergeret, M. Silaev, P. Virtanen, and T. T. Heikkilä, *Reviews of Modern Physics* **90**, 041001 (2018).

[173] T. T. Heikkilä, M. Silaev, P. Virtanen, and F. S. Bergeret, *Progress in Surface Science* **94**, 100540 (2019).

[174] G. De Simoni, E. Strambini, J. S. Moodera, F. S. Bergeret, and F. Giazotto, *Nano Letters* **18**, 6369 (2018).

[175] T. Heikkilä *et al.*, *Physical Review Applied* **10**, 034053 (2018).

[176] J. Linder and J. W. A. Robinson, *Nature Physics* **11**, 307 (2015).

[177] F. Giazotto, T. Heikkilä, and F. Bergeret, *Physical Review Letters* **114**, 067001 (2015).

[178] P. Virtanen, F. Bergeret, E. Strambini, F. Giazotto, and A. Braggio, *Physical Review B* **98**, 020501 (2018).

[179] Y. Liu *et al.*, *ACS Applied Materials & Interfaces* (2019).

[180] A. Mauger and C. Godart, *Physics Reports* **141**, 51 (1986).

[181] X. Hao, J. Moodera, and R. Meservey, *Physical Review B* **42**, 8235 (1990).

[182] P. Muduli *et al.*, *Physical Review B* **98**, 024416 (2018).

[183] A. B. Pippard, *Magnetoresistance in metals* (Cambridge University Press, Cambridge New York, 1989).

[184] L. K. Zou, Y. Zhang, L. Gu, J. W. Cai, and L. Sun, *Physical Review B* **93**, 075309 (2016).

[185] J. J. Hauser, *Physical Review* **187**, 580 (1969).

[186] W. J. Antel, M. M. Schwickert, T. Lin, W. L. O'Brien, and G. R. Harp, *Physical Review B* **60**, 12933 (1999).

[187] M. Weiler *et al.*, *Physical Review Letters* **108**, 106602 (2012).

[188] H. Bohn, W. Zinn, B. Dorner, and A. Kollmar, *Physical Review B* **22**, 5447 (1980).

[189] H. Bohn, A. Kollmar, and W. Zinn, *Physical Review B* **30**, 6504 (1984).

[190] W. Xing *et al.*, *Physical Review X* **9**, 011026 (2019).

[191] L. Cornelissen, J. Liu, B. Van Wees, and R. Duine, *Physical review letters* **120**, 097702 (2018).

[192] S. R. Boona and J. P. Heremans, *Physical Review B* **90**, 064421 (2014).

[193] X. J. Zhou *et al.*, *Applied Physics Letters* **110**, 062407 (2017).

[194] H. Jin, S. R. Boona, Z. Yang, R. C. Myers, and J. P. Heremans, *Physical Review B* **92**, 054436 (2015).

[195] K. Das, F. Dejene, B. van Wees, and I. Vera-Marun, *Applied Physics Letters* **114**, 072405 (2019).

[196] M. Wu and A. Hoffmann*Recent advances in magnetic insulators-from spintronics to microwave applications* Vol. 64 (Academic Press, 2013).

[197] D. Wesenberg, T. Liu, D. Balzar, M. Wu, and B. L. Zink, *Nature Physics* **13**, 987 (2017).

[198] H. Ochoa, R. Zarzuela, and Y. Tserkovnyak, *Physical Review B* **98**, 054424 (2018).

[199] C. M. Hurd, *Contemporary Physics* **23**, 469 (1982).

[200] J. M. D. Coey and D. H. Ryan, *IEEE transactions on magnetics* **20**, 1278 (1984).

[201] M. Dimer, E. Gerdau, R. Rüffer, H. D. Rüter, and W. Sturhahn, *Journal of Applied Physics* **79**, 9090 (1996).

[202] E. Mallmann, A. Sombra, J. Goes, and P. Fechine, Yttrium iron garnet: properties and applications review, in *Solid State Phenomena* Vol. 202, pp. 65–96, Trans Tech Publ, 2013.

[203] Y. G. Chukalkin, V. R. Shtirz, and B. N. Goshchitskii, *Physica Status Solidi (a)* **112**, 161 (1989).

[204] E. M. Gyorgy *et al.*, *Journal of Applied Physics* **50**, 2883 (1979).

[205] N. Thiery *et al.*, *Physical Review B* **97**, 064422 (2018).

B

[206] R. Metselaar and P. K. Larsen, *Proceedings of the international School of Physics Enrico Fermo* **70**, 417 (1978).

[207] M. F. Jakobsen, A. Qaiumzadeh, and A. Brataas, *Physical Review B* **100**, 134431 (2019).

[208] L. J. van der PAUW, A method of measuring specific resistivity and Hall effect of discs of arbitrary shape, in *Semiconductor Devices: Pioneering Papers*, pp. 174–182, WORLD SCIENTIFIC, 1991.

B

List of publications

This thesis is based on the following publications:

- *Anomalous Hall-like transverse magnetoresistance in Au thin films on* $Y_3Fe_5O_{12}$
  Tobias Kosub, Saül Vélez, Juan M. Gomez-Perez, Luis E. Hueso, Jürgen Fassbender, Fèlix Casanova and Denys Makarov,
  Appl. Phys. Lett. **113**, 222409 (2018).

  (Chapter 3)

- *Synthetic Antiferromagnetic Coupling Between Ultrathin Insulating Garnets*
  Juan M. Gomez-Perez, Saül Vélez, Lauren McKenzie-Sell, Mario Amado, Javier Herrero-Martin, Josu López-López, S. Blanco-Canosa, Luis E. Hueso, Andrey Chuvilin, Jason W. A. Robinson and Fèlix Casanova,
  Phys. Rev. Appl. **10**, 044046 (2018).

  (Chapter 4)

- *Paramagnetic Spin Hall Magnetoresistance*
  Koichi Oyanagi*, Juan M. Gomez-Perez*, Xian P. Zhang, Edurne Sagasta, T. Kikkawa, Vitaly N. Golovach, Luis E. Hueso, F. Sebastian Bergeret and Fèlix Casanova,
  in preparation.

  * Equal contribution

  (Chapter 5)

- *Large field-like torque in heavy metal/ferromagnetic insulator interface*
  Juan M. Gomez-Perez, Francesco Callavale, Marco Gobbi, Luis E. Hueso and Fèlix Casanova, Maxim Ilyn, Celia Rogero, Carmen Gónzale-Orellana Xian P. Zhang, Vitaly N. Golovach, F. Sebastian Bergeret
  in preparation.

  (Chapter 6)

- *Difference of the magnon diffusion length for electrically and thermally driven magnon currents in* $Y_3Fe_5O_{12}$
  Juan M. Gomez-Perez Saül Vélez, Luis E. Hueso and Fèlix Casanova,
  arXiv:1912.00490 (2019).

  (Chapter 7)

- *Absence of evidence of spin/magnon transport through amorphous* $Y_3Fe_5O_{12}$
  Juan M. Gomez-Perez, Koichi Oyanagi, Reimei Yahiro, Rafael Ramos, Luis E. Hueso, Eiji Saitoh and Fèlix Casanova,
  Appl. Phys. Lett **116**, 032401 (2020).

  (Chapter 8)

Other publications:

- *Absence of detectable current-induced magneto-optical Kerr effects in Pt, Ta and W*
  Patricia Riego, Saül Vélez, Juan M. Gomez-Perez, Jon ander Arregi, Luis E. Hueso, Fèlix Casanova and Andreas Berger,
  Appl. Phys. Lett. **109**, 172402 (2016).

- *Tunable Sign Change of Spin Hall Magnetoresistance in Pt/NiO/YIG Structures*
  Dazhi Hou, Zhiyong Qiu, Joseph Barker, Koji Sato, Kei Yamamoto, Saül Vélez, Juan M. Gomez-Perez, Luis E. Hueso, Fèlix Casanova and Eiji Saitoh,
  Phys. Rev. Lett. **118**, 147202 (2017).

- *Thermally driven long-range magnon spin current in yttrium iron garnet due to intrinsic spin Seebeck effect*
  Brandon L. Giles, Zihao Yang, John S. Jamison, Juan M. Gomez-Perez, Saül Vélez, Luis E. Hueso, Fèlix Casanova and Roberto C. Myers,
  Phys. Rev. B **96**, 180412 (2017).

- *Spin fluctuation, geometrical size effects, and zero-field topological order in textured MnSi thin films*
  Josu López-López, Juan M. Gomez-Perez, S.Álvarez, Hari Babu Vasili, A. C. Komarek, Luis E. Hueso, Fèlix Casanova and S. Blanco-Canosa,
  Phys. Rev. B **99**, 144427 (2019).

- *Spin-Hall magnetoresistance in a low-dimensional Heisenberg ferromagnet*
  Saül Vélez, Vitaly N. Golovach, Juan M. Gomez-Perez, Andrey Chuvilin, Cong Tinh Bui, F. Rivadulla, Luis E. Hueso, F. Sebastián Bergeret and Fèlix Casanova,
  Phys. Rev. B **100**, 180401(R) (2019).